IN-SITU TURBULENT FLOCCULATION AND REACTOR MIXING CHARACTERIZATON FOR A SQUARE TANK REACTOR USING IMAGE ANALYSIS AND PARTICLE IMAGE VELOCIMETRY METHODOLOGIES

A Thesis

By

KALEISHA DANAE HAYNES MILLER

Submitted to the Graduate and Professional School of
Texas A&M University
in partial fulfillments of the requirements for the degree of

MASTER OF SCIENCE

Co-Chair of Committee:	Kuang-An Chang
Co-Chair of Committee:	Shankar Chellam
Committee Member:	Dion Antao
Head of Department:	Zachary Grasley

May 2022

Major Subject: Civil Engineering

ABSTRACT

Coagulation and flocculation are common processes in conventional water treatment and the resulting floc size distributions, mean size, and fractal dimension are impacted by operational parameters, including mixing and coagulant dosing method. In this investigation, a novel, non-intrusive methodology combining image analysis and particle image velocimetry was employed to characterize flocculation and reactor mixing from the same data. Image processing techniques were used to characterize flocculation following conventional $FeCl_3$ chemical coagulation and iron electrocoagulation while particle image velocimetry was used to characterize reactor mixing using flocs as tracking particles. Local velocity gradients were compared with the global velocity gradient, G. Results suggest electrocoagulation produced larger and more compact flocs than flocs formed by conventional coagulation. Use of flocs as tracking particles was more reliable prior to steady-state conditions, when flocs were smaller and more numerous. Compared to local velocity gradients, G underestimated actual mixing near the mixing impeller by 40%.

CONTRIBUTORS AND FUNDING SOURCES

Contributors:

This work was supervised and supported by a thesis committee consisting of Drs. Kuang-An Chang and Shankar Chellam, both as co-committee chairs and by Dr. Dion Antao of the Department of Mechanical Engineering as a committee member.

Experimental design and execution, and data collection were performed by Drs. Wei-Liang Chuang and Kyungho Kim in 2018-2019 while they were a post-doc and PhD student, respectively. Preliminary data analysis structure was prepared and provided by Dr. Wei-Liang Chuang.

All other work conducted for the thesis was completed by the student independently.

Funding Sources:

Graduate study was supported by a fellowship from Texas A&M University.

NOMENCLATURE

CC	Chemical Coagulation
D_2	Two-Dimensional Fractal Dimension
EC	Electrocoagulation
FFT	Fast Fourier Transform
G	Global Velocity Gradient
PIV	Particle Image Velocimetry
TKED	Turbulent Kinetic Energy Dissipation

TABLE OF CONTENTS

Page

ABSTRACT ii

CONTRIBUTORS AND FUNDING SOURCES iii

NOMENCLATURE iv

TABLE OF CONTENTS v

LIST OF FIGURES vi

LIST OF TABLES x

1. INTRODUCTION 1

    1.1. Theoretical Background 5

2. METHODS 13

    2.1. Experimental Setup 13
    2.2. Image Processing and Flocculation Characterization 16
    2.3. Particle Image Velocimetry and Reactor Mixing Characterization 25

3. RESULTS 30

    3.1. Flocculation Characterizations 30
    3.2. Reactor Mixing Characterizations 38
    3.3. Global Velocity Gradient Evaluation 52

4. DISCUSSION 57

    4.1. Flocculation Characterization 57
    4.2. Reactor Mixing Characterization 60
    4.3. Global Velocity Gradient Evaluation 62

5. CONCLUSIONS 64

REFERENCES 67

APPENDIX A 75

APPENDIX B 89

APPENDIX C 91

APPENDIX D 102

LIST OF FIGURES

Page

Figure 1: Microscopic image of a ferric hydroxide flocs 5

Figure 2: Schematic of experimental setup including (a) plan view and (b) profile view..... 15

Figure 3: Erosion of a 9 x 9 object with a 4-pixel diamond structuring element 20

Figure 4: Summary of image processing steps 22

Figure 5: Example derivation of D_2 for a hypothetical floc data set 23

Figure 6: Monte Carlo simulation to determine the probability a spherical floc will be accurately measured based on location within the laser light sheet 25

Figure 7: Temporal evolution of floc size..... 33

Figure 8: Temporal evolution of floc mean size for CC and EC 35

Figure 9: Parity plot of the overall mean equivalent diameter for CC and EC experiments for duplicate tests (DS#1.a and DS#1.b) 35

Figure 10: Parity plot of the top 10% mean equivalent diameter for CC and EC experiments for duplicate tests (DS#1.a and DS#1.b) 36

Figure 11: Temporal evolution of the 2D fractal dimension for CC and EC experiments..... 37

Figure 12**:** Parity plot of the 2D fractal dimension data for CC and EC experiments for the duplicate tests (DS#1.a and DS#1.b) 38

Figure 13: Vector rejection percentage for CC and EC experiments. 40

Figure 14: Energy spectrum for the: (a) horizontal (U) velocity components and (b) vertical (W) velocity components for CC at 11 minutes and EC at 20 minutes 41

Figure 15: Average 2D turbulence intensity for the CC experiment. 43

Figure 16: Average 2D turbulence intensity for the EC experiment 44

Figure 17: Average 2D turbulence intensity for the artificially seeded experiment..... 45

Figure 18: Mean TKED rate over time for CC and EC for DS#1.b. 47

Figure 19: Average local TKED rate for the CC experiment 48

Figure 20: Average local TKED rate for the EC experiment. 49

Figure 21: Average local TKED rate for artificially seeded experiment 50

Figure 22: Contours of the average ratio of the local velocity gradients to the global velocity gradient, G, as determined by the spatially averaged TKED rate for the CC experiment 54

Figure 23: Contours of the average ratio of the local velocity gradients to the global velocity gradient, G, as determined by the spatially averaged TKED rate for the EC experiment 55

Figure 24: Contours of the average ratio of the local velocity gradients to the global velocity gradient, G, as determined by the spatially averaged TKED rate for the artificially seeded experiment 56

Figure A-25: Mean particle count based on different binary threshold methods at (a) 7 minutes; (b) 22 minutes; (c) 27 minutes; and (d) 36 minutes for CC, DS#1.a 75

Figure A-26: Mean particle count based on different binary threshold methods at (a) 7 minutes; (b) 22 minutes; (c) 27 minutes; and (d) 36 minutes for EC, DS#1.a. 76

Figure A-27: Energy spectrum at the left upper, left middle, and left bottom region for horizontal (U) and vertical (W) velocity components for CC at (a) 2 minutes; (b) 17 minutes and (c) 38 minutes for DS#1.b 77

Figure A-28: Energy spectrum at the left upper, left middle, and left bottom region for horizontal (U) and vertical (W) velocity components for EC at (a) 2 minutes; (b) 17 minutes and (c) 38 minutes for DS#1.b 78

Figure A-29: Energy spectrum at the left upper, left middle, and left bottom region for horizontal (U) and vertical (W) velocity components for the artificially seeded system for DS#1.b. 79

Figure A-30: Ratio of turbulence intensity values measured in the CC and EC experiments 80

Figure A-31: Relative turbulence intensity deviation when comparing the turbulence intensity measurements between the CC and Seeded experiments for DS#1.b. 81

Figure A-32: Relative turbulence intensity deviation when comparing the turbulence intensity measurements between the EC and Seeded experiments for DS#1.b. 82

Figure A-33: Vertical variation of the TKED rate at 1 cm, 2.7 cm, 7 cm, and 9 cm along the horizontal axis by method and method average for the CC experiment 83

Figure A-34: Vertical variation of the TKED rate at 1 cm, 2.7 cm, 7 cm, and 9 cm along the horizontal axis by method and method average for the EC experiment 84

Figure A-35: Vertical variation of the TKED rate at 1 cm, 2.7 cm, 3 cm, and 3.9 cm along the horizontal axis by method and method average for the artificially seeded experiment 85

Figure A-36: Ratio of TKED rate from the CC and EC experiments for DS#1.b 86

Figure A-37: Relative TKED rate deviation when comparing the TKED rate data from the CC and Seeded experiments for DS#1.b 87

Figure A-38: Relative TKED rate deviation when comparing the TKED rate data from the EC and Seeded experiments for DS#1.b 88

Figure B-39: Temporal evolution of floc size for DS#1.b 89

Figure B-40: Floc mean size evolution for CC and EC for DS#1.b 90

Figure B-41: 2D fractal dimension for CC and EC for DS#1.b 90

Figure C-42: Vector rejection percentage for the CC and EC experiments for DS#2 91

Figure C-43: Energy spectrum at the left upper, left middle, and left bottom region for horizontal (U) and vertical (W) velocity components for CC, DS#2 at (a) 2 minutes; (b) 17 minutes and (c) 38 minutes for DS#2 92

Figure C-44: Energy spectrum at the left upper, left middle, and left bottom region for horizontal (U) and vertical (W) velocity components for EC, DS#2 at (a) 2 minutes; (b) 17 minutes and (c) 38 minutes for DS#2 93

Figure C-45**:** Average 2D turbulence intensity for the CC experiment for DS#2 94

Figure C-46**:** Average 2D turbulence intensity for the EC experiment for DS#2. 95

Figure C-47: Ratio of turbulence intensity values measured in the CC and EC experiments for DS#2. 96

Figure C-48 Average local TKED rate for the CC experiment for DS#2 97

Figure C-49**:** Average local TKED rate for the EC experiment for DS#2 98

Figure C-50: Ratio of TKED rate from the CC and EC experiments for DS#2 99

Figure C-51: Contours of the average ratio of the local velocity gradients to the global velocity gradient, G, as determined by the spatially averaged TKED rate for the CC experiment for DS#2 100

Figure C-52**:** Contours of the average ratio of the local velocity gradients to the global velocity gradient, G, as determined by the spatially averaged TKED rate for the EC experiment for DS#2 101

Figure D-53: Mean TKED rate over time for CC and EC for DS#1.b and DS#2. 102

Figure D-54: Ratio of turbulence intensity results between DS#1.b to DS#2 for the CC experiment..... 103

Figure D-55: Ratio of turbulence intensity results between DS#1.b to DS#2 for the EC experiment..... 104

Figure D-56: Ratio of CC experimental results of TKED rate between DS#1.b to DS#2 105

Figure D-57: Ratio of EC experimental results of TKED rate between DS#1.b to DS#2..... 106

LIST OF TABLES

Page

Table 1: Summary of Data Sets and Roles 30

Table 2: 2D turbulence intensity data comparison between CC, EC, DS#1.b and DS#2..... 46

Table 3: TKED rate data comparison between CC, EC, Seeded, DS#1.b and DS#2 51

Table 4: Summary of the average TKED rate and the Kolmogorov length and time scales for CC, EC, and seeded water experiments and based on the G-Curve produced by Cornwell and Bishop [57] for DS#1.b. 52

Table 5: Spatially-averaged TKED rate (ε) and the global velocity gradient (G), for flow field measurements using flocs, seeded water, and the G-curve from DS#1.b. 53

1. INTRODUCTION

Coagulation and flocculation are key processes in various water treatment applications including treatment of municipal, industrial, and produced water [1-3]. In untreated waters, electrostatic repulsion of particles causes particles to remain separated and suspended in solution instead of agglomerating and settling out of solution. To eliminate electrostatic repulsion and facilitate particle agglomeration, coagulants, such as aluminum or iron salts, are added in a process known as coagulation. After coagulant addition, the suspended particles agglomerate into flocs in a process known as flocculation. These flocs are then removed from the water in subsequent treatment steps such as gravity separation (i.e., sedimentation or dissolved air flotation) [4]. Flocculation characteristics of interest due to their impact on the efficacy of subsequent treatment steps include the steady state floc size distribution and the floc fractal dimension [5, 6]. The steady state floc size distribution for a set of given conditions (e.g., mixing speed, impeller shape, coagulation method, and coagulant dosage), reveals if the conditions induce the desired changes in floc size, with the ultimate goal of producing floc sizes ideal for gravity separation [4]. The average steady-state floc size provides key insights into floc strength, which relates to how flocs will respond to mixing shear stresses [7, 8]. The floc fractal dimension reveals if the flocs are highly branched structures, which are slower to settle than dense, spherical flocs [1]. These characteristics are commonly evaluated using small-scale testing (e.g., jar testing) to determine the optimal operational considerations for full-scale treatment facilities.

Two key operational considerations that influence these flocculation characteristics include the coagulation method and mixing characteristics. Coagulants are typically introduced in the system by directly adding coagulants from a stock solution, referred to herein as conventional chemical coagulation (CC), or through *in-situ* coagulant generation via electrolytic oxidation of a sacrificial

anode of a selected metal, known as electrocoagulation (EC). CC is a common coagulant dosing method and extensive work has focused on flocculation characteristics using CC [6, 8-11]. In contrast, EC is less widely studied [12-16] but has particular advantages over CC that may increase its adoption and acceptance. Advantages to EC include reductions of hazardous chemical transportation and handling, due to the *in-situ* coagulant generation, which also lends itself to use of renewable energy sources [17]. Further, EC has a decreased impact on influent water quality parameters such as pH and alkalinity [17, 18] and increased pollutant removal efficiencies in certain applications [12]. In contrast to CC, EC generates coagulating metal ions by the application of a current to an electrochemical cell equipped with a cathode and a sacrificial anode of a particular metal [19]. These coagulating metal ions operate similarly to coagulants added via CC and facilitate aggregation during flocculation. Although CC and EC operate similarly, the two coagulation methods are known to generate flocs with different structural characteristics (e.g., compactness, size, strength), induce different changes in water chemistry (e.g., pH, dissolved oxygen concentration, alkalinity), and can result in different coagulating metal ions, depending on water chemistry [18-20].

Another important operational consideration is mixing, which facilitates particle collisions resulting in floc growth but can also result in floc breakage depending on mixing speed and floc strength [7]. Beyond flocculation impacts, mixing also has important energy implications, as rapid mixing during coagulant addition was found to constitute the second highest energy user in a typical municipal water treatment plant [21]. In practice, water treatment facilities often employ turbulent flocculation, which is marked by a wide spectrum of velocity gradients, providing means for particle collision and floc growth [4]. The global velocity gradient, G, introduced by Camp and Stein [22] is used as a simple characterization of reactor mixing and represents a spatial-average

of the local velocity gradients present within the reactor. Despite significant criticism of G focused on both its accuracy as a mixing characterization and relevance to turbulent flocculation [2, 23, 24], it a widely used water treatment design parameter. Several studies have evaluated G's impact on flocculation efficacy [9, 25, 26], but these investigations do not consider deviations between G and the local velocity gradients, which can be substantial [2, 27]. As reactor mixing has significant impacts on flocculation efficiency, impacting a variety of flocculation characterizations of interest (e.g., growth rate, steady-state size distribution, floc strength, and fractal dimension) [28-30], a detailed understanding of reactor mixing is key in developing mixing operations that optimize flocculation.

To develop a comprehensive understanding of how these coagulant dosing and reactor mixing impact flocculation, simultaneous observations of flocculation and reactor mixing using non-intrusive, *in-situ* techniques are needed. However, past investigations into flocculation characterizations often utilize a microscope or particle counter and require transporting the flocs from the reactor for analysis, which can impact the floc structure [2, 5, 6, 30]. Further, reactor mixing characterization using intrusive measurement technologies, such as hot wire anemometry, can alter the surrounding flow field, and suffer from limited spatial resolution [31]. To avoid altering the experimental environment and to accurately characterize the entire system, *in-situ*, non-intrusive measurement techniques are critical.

Despite the impact of reactor mixing on flocculation efficiency, studies combining flocculation and mixing characterization using *in-situ* techniques are lacking, resulting in a knowledge gap when considering the fundamental impacts of mixing on flocculation. New methodology is needed that enables simultaneous evaluations of these characteristics using non-intrusive techniques to ultimately inform flocculation reactor design and operation. In response to this need, the current

investigation implemented a novel methodology which combines image analysis techniques and particle image velocimetry (PIV) to collectively characterize flocculation and reactor mixing, providing a framework to enable a wide variety of comprehensive coagulation and flocculation investigations. This methodology relies solely on cross-sectional reactor imaging during flocculation, facilitating spatiotemporal evaluations of flocculation and reactor mixing using the same data collection instance and methodology, which enables fundamental comparisons. While traditional PIV analyses rely on water artificially seeded with tracer particles [32], this investigation leveraged flocs generated during the experiment to track fluid motion and inform turbulent mixing analyses. Because flocs were used to track the fluid motion, flocculation characterizations were uninfluenced by artificial tracer particle presence and both flocculation and reactor mixing were evaluated using the same data set. This novel methodology was applied in the current investigation to evaluate both CC and the lesser-studied EC in terms of flocculation and reactor mixing. Further, this methodology was used to develop pertinent turbulent mixing analyses required to evaluate the accuracy of G throughout the reactor cross section.

The major research objectives of this investigation were to (1) evaluate flocculation characteristics using non-intrusive, *in-situ* techniques to observe floc growth, steady-state size distribution, and fractal geometry for both CC and EC using iron as the metal-ion coagulant; (2) evaluate reactor mixing characteristics using non-intrusive, *in-situ* techniques to measure the velocity field over a vertical reactor cross section and to develop pertinent turbulent flow analyses (e.g., turbulence intensity, turbulent kinetic energy dissipation rate, and turbulent length and time scales), using flocs as tracking particles for the PIV analysis; and (3) compare G with local velocity gradients to evaluate how well G characterizes actual reactor mixing.

1.1. Theoretical Background

1.1.1. Fractal Dimension

Although flocs are frequently considered as Euclidian shapes in flocculation modeling, their shape is better characterized as an irregular, fractal form marked by self-similarity (i.e., morphological characteristics are uniform across all sizes) [6, 33-35]. This fractal form arises from the floc agglomeration into increasingly larger flocs, which produces an irregular, non-Euclidian shaped floc (e.g., Figure 1) that does not follow the coalesced sphere assumption employed in fundamental flocculation modeling and has different hydrodynamic interactions due to floc porosity [4, 36]. A primary way to characterize these irregular fractal forms is through the fractal dimension, which relates the size properties of the floc to a particular length scale [37-39]. This fractal dimension provides important insights into properties that impact accuracy of flocculation modeling and settling rate such as porosity and density [34, 36, 40]. Flocculation models incorporating the flocs' fractal nature reduce the modeling error associated with the coalesced sphere assumption and more accurately predict flocculation behavior [4, 41].

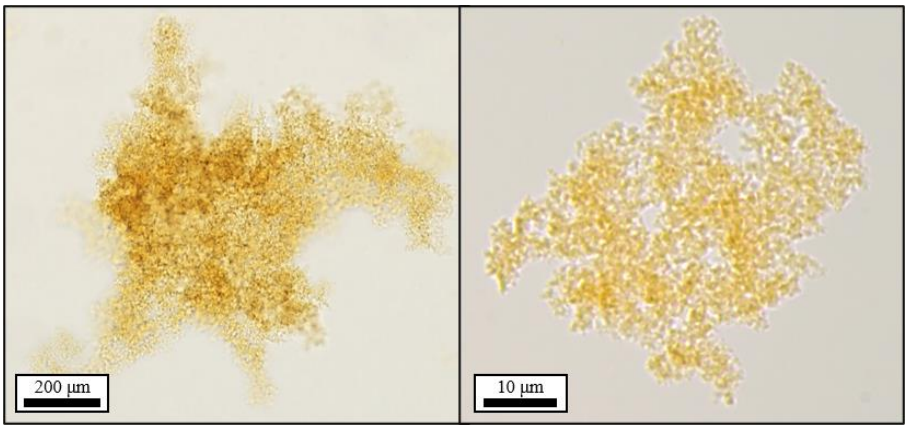

Figure 1: Microscopic image of ferric hydroxide flocs produced by conventional chemical coagulation (left) and by electrocoagulation (right). Note, these images are presented as representative images for visual purposes only.

Three commonly used fractal dimensions include the three-dimensional fractal dimension (D_3), which relates the floc volume to a characteristic floc length [4, 35]; the two-dimensional fractal dimension (D_2), which relates the projected floc area to a characteristic floc length [4, 35, 37, 38]; and the boundary fractal dimension (D_b), which relates the projected floc area to the floc perimeter [35, 37, 38]. Various length properties have been used as the characteristic length in the derivation of D_3 and D_2 including the major axis length, diameter, and radius [35, 42, 43]. For the purposes of this investigation, D_2 is used to characterize the flocs' fractal nature through the following relationship:

$$A \propto l^{D_2} \tag{1}$$

where A is the projected surface area, and l is the major axis length. Based on this relationship, the floc's projected surface area grows according to a power relationship with its major axis length. For Euclidean shapes, the area is always related to the square of the characteristic length (i.e., $D_2 = 2$). For fractal flocs, D_2 varies from 2 for densely packed, spherical flocs, indicating a lower floc porosity and higher floc density and to lower D_2 values for large, highly porous flocs with open structures, indicating a high water content and subsequently a low floc density [1, 6, 37]. Thus, the floc fractal dimension provides insights into floc characteristics that impact operational performance such as density and water content that further impact floc settling velocity.

1.1.2. Turbulent Flow Characterization

Prior to characterizing turbulent flocculation, turbulent flow fundamentals must be established. At a fundamental level, turbulent flows for a particular point in space can be viewed as the summation of the mean and fluctuating velocity component, resulting from the Reynolds decomposition as shown in Equation 2 in tensor notation:

$$U_i = \overline{U}_\iota + u_i \tag{2}$$

where U represents the total instantaneous velocity, $\overline{U}$ represents the mean velocity over time, and u represents the fluctuating velocity component at a particular time. The fluctuating velocity component has a zero mean but largely dictates the turbulent kinetic energy dissipation (TKED) rate, ε, which is used in the estimation of G, and is used to determine the turbulence intensity, I. For two-dimensional (2D) flow measurements, the 2D turbulence intensity (I_{2D}) uses only two velocity components and is calculated as:

$$I_{2D} = \sqrt{\overline{u_\iota{}^2} + \overline{u_J{}^2}} \tag{3}$$

The TKED rate, ε, represents the rate at which energy is transferred from the large energy-containing scales of turbulent motion to the small energy-dissipating scales of turbulent motion [44]. Between these two scales of turbulent motion lies the inertial subrange, within which motions are completely dependent on the inertial effects rather than viscous effects, per Kolmogorov's second hypothesis [44]. The rate at which energy is transferred from the energy-containing to the energy-dissipating range is equivalent to the dissipation and production rate. Thus, the TKED rate provides insights into the energy production rate within the system, which, in the case of turbulent flocculation, is a result of reactor mixing. The TKED rate is found through the turbulent energy budget as:

$$\varepsilon = 2\nu\overline{s_{\iota J} s_{\iota J}} \tag{4}$$

where ν represents the kinematic viscosity of the fluid and s_{ij} represents the tensor notation of the fluctuating strain rate. This fluctuating strain rate can be expanded as [44]:

$$s_{ij} = \frac{1}{2}\left(\frac{\partial u_i}{\partial x_j} + \frac{\partial u_j}{\partial x_i}\right) \tag{5}$$

Thus, the TKED rate from Equation 4 can be rewritten as:

$$\varepsilon = \frac{1}{2}\nu\overline{\left(\frac{\partial u_i}{\partial x_j} + \frac{\partial u_j}{\partial x_i}\right)^2} \tag{6}$$

which contains a total of 12 terms for 3-dimensional (3D) flow, including nine velocity gradients and three cross products. 2D PIV velocity measurements permit direct measurement for five terms (four velocity gradients and one cross product) and one term can easily be obtained by the continuity equation for incompressible flow. The remaining six terms (four velocity gradients and two cross products) must be estimated based on assumptions about the nature of turbulent flow in question [45]. TKED rate estimation using 2D PIV methodologies is common and there are several existing methods to estimate the missing terms in Equation 6. George and Hussein [46] derived a TKED rate estimation based on the assumption that the turbulent flow was locally axisymmetric, meaning that turbulence does not change around the preferred axis (Equation 7). Kimmoun and Branger [47] assumed that rate of change of velocity out-of-plane was small compared to the rate of change of velocity in-plane, and approximated out-of-plane velocity gradients using the in-plane velocity gradients (Equation 8). Luznik et al., [48] applied a modified version of the TKED rate estimate developed by Doron et al., [49] who applied the continuity equation and assumed lateral fluctuations are of similar magnitude (Equation 9), with modifications correcting for the appropriate isotropic limits. Cowen et al., [50] applied a central difference technique to the product of fluctuation strain rate and added an empirical coefficient (c_1) to account for the missing terms (Equation 10), while Sharp and Adrian [51] assumed statistically isotropic turbulence for unmeasured velocity components (Equation 11). For the purposes of this experiment, TKED rate was evaluated by each of the aforementioned estimation methods and the average is reported to provide a general TKED rate estimation.

$$\varepsilon_{George\ \&\ Hussein} = \nu\left(-\overline{\left(\frac{\partial u}{\partial x}\right)^2} + 2\overline{\left(\frac{\partial u}{\partial z}\right)^2} + 2\overline{\left(\frac{\partial w}{\partial x}\right)^2} + 8\overline{\left(\frac{\partial w}{\partial z}\right)^2}\right) \quad (7)$$

$$\varepsilon_{Kimmoun\ \&\ Branger} = \frac{1}{3}\nu\left(7\overline{\left(\frac{\partial u}{\partial x}\right)^2} + 7\overline{\left(\frac{\partial w}{\partial z}\right)^2} + 4\overline{\left(\frac{\partial u}{\partial z}\right)^2} + 4\overline{\left(\frac{\partial w}{\partial x}\right)^2} + 6\overline{\left(\frac{\partial u}{\partial z}\frac{\partial w}{\partial x}\right)}\right) \quad (8)$$

$$\varepsilon_{Luznik\ et\ al.} = \nu\left(4\overline{\left(\frac{\partial u}{\partial x}\right)^2} + 4\overline{\left(\frac{\partial w}{\partial z}\right)^2} + 3\overline{\left(\frac{\partial u}{\partial z}\right)^2} + 3\overline{\left(\frac{\partial w}{\partial x}\right)^2} + 4\overline{\left(\frac{\partial u}{\partial x}\frac{\partial w}{\partial z}\right)} + 6\overline{\left(\frac{\partial u}{\partial z}\frac{\partial w}{\partial x}\right)}\right) \quad (9)$$

$$\varepsilon_{Cowen\ et\ al.} = 2\nu c_1\left(\overline{\left(\frac{\partial u}{\partial x}\right)^2} + \overline{\left(\frac{\partial w}{\partial z}\right)^2} + \frac{1}{2}\overline{\left(\frac{\partial u}{\partial z}\right)^2} + \frac{1}{2}\overline{\left(\frac{\partial w}{\partial x}\right)^2} + \overline{\left(\frac{\partial u}{\partial z}\frac{\partial w}{\partial x}\right)}\right) \quad (10)$$

$$\varepsilon_{Sharp\ \&\ Adrian} = \nu\left(2\overline{\left(\frac{\partial u}{\partial x}\right)^2} + 2\overline{\left(\frac{\partial w}{\partial z}\right)^2} + 3\overline{\left(\frac{\partial u}{\partial z}\right)^2} + 3\overline{\left(\frac{\partial w}{\partial x}\right)^2} + 2\overline{\left(\frac{\partial u}{\partial z}\frac{\partial w}{\partial x}\right)}\right) \quad (11)$$

When evaluating the TKED rate, the velocity resolution has a significant impact on the accuracy of the results [52, 53]. Given the PIV methodology, the information obtained experimentally represents the average velocity of all the particles within the smallest interrogation window, resulting in a spatial filtering within each interrogation window [11, 51, 53]. For large interrogation window sizes, the PIV methodology is unable to provide information on the small, energy dissipating scales, which are critical for accurate TKED rate estimation [31, 53]. The impact of the velocity data's spatial resolution on the TKED rate is minimized when the spatial resolution is within a few multiples of the Kolmogorov length scale [31]. The Kolmogorov length scale, η is defined as:

$$\eta = \left(\frac{\nu^3}{\varepsilon}\right)^{0.25} \quad (12)$$

and represents the length scale of the energy-dissipating eddies. If the spatial resolution is higher than a few multiples of η, the frequencies of the velocity spectra responsible for dissipating the energy are not fully captured by the methodology and subsequent calculations poorly represent the turbulent flow [31]. An additional characteristic scale of turbulent flow is known as the Kolmogorov time scale, τ, defined as:

$$\tau = \left(\frac{\nu}{\varepsilon}\right)^{0.5} \tag{13}$$

which represents the highest frequency of the velocity time series spectra. Per the Nyquist criteria, the sampling frequency should be at least double the highest frequency of the data signal. Therefore, the sampling frequency should be at least double the inverse Kolmogorov time scale.

In addition to the Kolmogorov's length and time scales, the spectral analysis of turbulent motion also exhibits a characteristic trend known as the Kolmogorov -5/3 spectrum [44]. This spectrum characterizes how the energy is distributed among various eddies and, for turbulent flows, exhibits a characteristic -5/3 slope in the inertial subrange. The energy spectrum, S, for a velocity signal can be evaluated by converting the velocity signal into the frequency domain through a fast Fourier transform (FFT) and then calculating the energy spectrum per Equation 14.

$$S = \frac{2}{\Delta f} F F^* \tag{14}$$

where F represents the FFT of the velocity signal, * denotes the complex conjugate, and Δf is the frequency scale which is found by dividing the sampling frequency by the total number of samples. The presence of a turbulent flow regime can thus be verified by evaluating the energy spectrum and identifying if the Kolmogorov -5/3 spectrum is present.

1.1.3. Global Velocity Gradient, G

The global velocity gradient, G, also known as the average velocity gradient [10], root-mean-squared velocity gradient [22, 23] or the average characteristic velocity gradient [9], is a commonly used parameter in coagulation and flocculation design intended to characterize the degree of mixing intensity in turbulent flocculation. In their original introduction of G, Camp and Stein [22] defined G as:

$$\Phi = \mu G^2 = \left[\left(\frac{\partial u}{\partial y} + \frac{\partial v}{\partial x}\right)^2 + \left(\frac{\partial u}{\partial z} + \frac{\partial w}{\partial x}\right)^2 + \left(\frac{\partial v}{\partial z} + \frac{\partial w}{\partial y}\right)^2\right] \quad (15)$$

where Φ represents the total work done per unit volume for a unit time and μ represents the dynamic viscosity. They indicated this representation of G was valid in both laminar and turbulent flows and was a useful method of relating particle aggregation rate to energy dissipation and could be used to represent the velocity gradients responsible for particle collision in the Smoluchowski equation [54, 55]. The double equality in Equation 15 has been challenged since Φ is not equal to the right hand term [54] due to the missing diagonal terms in the 3D strain rate tensor [23]. While Camp and Stein [22] justified the omission of the diagonal terms by asserting that the maximum shear in the system could be determined by adjusting the frame of reference such that these diagonal terms vanish to zero, a tensorial approach by Clark [23] found this to be incorrect in 3D flows. Additionally, Cleasby [55] questioned G's applicability for particles larger than the Kolmogorov length scale while Han and Lawler [24] fundamentally questioned the role of G in flocculation modeling when considering heterodisperse and curvilinear flocculation. G was also evaluated experimentally by Cheng et al., [27] and Park and Park [56], among others. Cheng et al., [27] used PIV methodologies to evaluate the spatial variation of the TKED rate and found the TKED rate to be highly variable and thus G would poorly characterize the mixing in different

reactor regions. Further, Park and Park [56] used PIV to evaluate the TKED rate for various shaped reactors and determined that G was unable to accurately represent the range of mixing velocities present within the reactor.

Despite these criticisms, G remains a prevalent design parameter and can be calculated using mean flow characteristics by the following:

$$G = \left(\frac{\bar{\Phi}}{\mu}\right)^{0.5} = \left(\frac{\bar{\varepsilon}}{\nu}\right)^{0.5} \tag{16}$$

where $\bar{\Phi}$ represents the mean value of total work done per unit volume for a unit time and $\bar{\varepsilon}$ represents the spatially-averaged TKED rate. Additionally, following the assumption that the rate of energy dissipation equals the power supply, G can also be calculated as:

$$G = \left(\frac{P}{\mu V}\right)^{0.5} \tag{17}$$

where P represents the power input into the reactor and V represents the liquid volume of the reactor. While the determination of $\bar{\varepsilon}$ requires knowledge of the local velocity gradients throughout the reactor that are not easily determined without detailed measuring equipment, macroscopic parameters P and V are easily determined, and are used to develop G-curves that relate G to the mixing speed for a particular reactor, impeller, and water temperature [57].

Although G is commonly used in turbulent reactor design as a substitute for the velocity gradient range, it oversimplifies the actual velocity gradients in reactor mixing and in so doing, provides poor flocculation efficiency estimates. Improved understanding of how the velocity gradients vary spatiotemporally within the reactor in question, and if these same patterns are observed for different sized reactors are critical to effective turbulent flocculation reactor design.

2. METHODS

2.1. Experimental Setup

Experiments were performed in a square 2-liter Phipps and Bird B-KER2® Laboratory Jar reactor equipped with a 2-blade paddle mixer. The paddle mixer shaft was centrally located in the reactor, and the paddle was situated close to the bottom of the tank as shown in Figure 2. Mixing was supplied by a DC gear box motor and mixing speed was controlled through an Astron DC power supply with digital readout of amperage and voltage. The system was rapid-mixed at 100 rpm for approximately 2.6 minutes during the coagulant addition (CC) or generation (EC) and initial mixing and then slow-mixed (flocculated) at 15 rpm for approximately 40 minutes.

The reactors were filled to the 2-liter mark with distilled water, 5mM of sodium chloride was added, and the solution was buffered with 20 mM of sodium bicarbonate ($NaHCO_3$) to maintain an approximate pH of 8.3 throughout the experiment, maintaining conditions suitable for $Fe(OH)_3$ floc precipitation. The reactor solutions were oxygen-saturated to approximately 8.3 mg/L prior to coagulant addition. A target coagulant dosage of 10 mg Fe/L was selected based on iteration to provide an optimal floc concentration. Dosages larger than 10 mg Fe/L resulted in the excess floc formation which clouded the image data and made floc border detection difficult. In contrast, dosages less than 10 mg Fe/L resulted in an insufficient floc precipitation for subsequent flocculation characterization. For CC experiments, a stock solution of 324 mM of Fe was prepared by dissolving 4.4 grams of $FeCl_3 \cdot 6H_2O$ into 50 mL of ultrapure water. Approximately 1.1 mL of this stock solution was added to the reactor, resulting in the target concentration of 10 mg Fe/L. For the EC experiments, the coagulant was produced through an annular electrode configuration comprised of a cylindrical sacrificial iron anode within a perforated cathode operated in constant current mode and located in the corner of the square reactor as shown in Figure 2. The anode was

Fe(0) with a 99.95% metal basis purity and an initial effective area of 35.9 cm^2. The perforated cathode was dimensionally stable 316 stainless steel and the gap between the anode and cathode was 2 mm. The EC system was operated at a constant current of 0.5 A, resulting in a current density of 14 mA/cm^2. The current was chosen to minimize electrolysis duration and avoid oxygen depletion and green rust formation [15]. The EC system was operated for approximately 138 seconds to produce 10 mg Fe/L, matching the CC coagulant concentration. Bubbles were observed during the EC system operation but appeared to rise and leave the system during the rapid mixing period. The EC apparatus was removed from the reactor after the coagulant generation.

For both the CC and EC experiments, a vertical cross section of the reactor was illuminated using a Millenia eV CW diode-pumped solid-state (DPSS) laser operated at 10W combined with optics to convert the concentrated laser beam into a light sheet approximately 2.3 mm thick and situated approximately 3 cm from the reactor wall as shown in Figure 2. Images were captured using a Phantom Miro M340 charged couple device (CCD) camera with a 25.6 mm by 16.0 mm 12-bit complementary metal oxide semiconductor (CMOS) sensor with a maximum resolution of 2,560 horizontal pixels by 1,600 vertical pixels. For this experiment, the output image size was selected as 1,600 horizontal pixels by 1,600 vertical pixels to capture a square cross section of the reactor. The camera was equipped with a 60 mm Nikon AF NIKKOR lens at an effective lens focal plane distance of 406 mm, resulting in 108 mm by 108 mm field of view, a resolution of approximately 67.6 μm per pixel and a 4 mm depth of field. The field of view dimensions were confirmed by imaging a ruler located within the focal plane and verifying the pixel resolution. The camera aperture was set to f/2.8 to enable maximum light capture with an exposure time of 200 μs set to freeze particle motion and reduce blurriness. The experiment was performed in a dark room to reduce background noise and enable sharp floc images illuminated by the laser sheet. The

experiment was performed on an optical table to eliminate vibrations that might interfere with the positioning of the laser light sheet and focal plane.

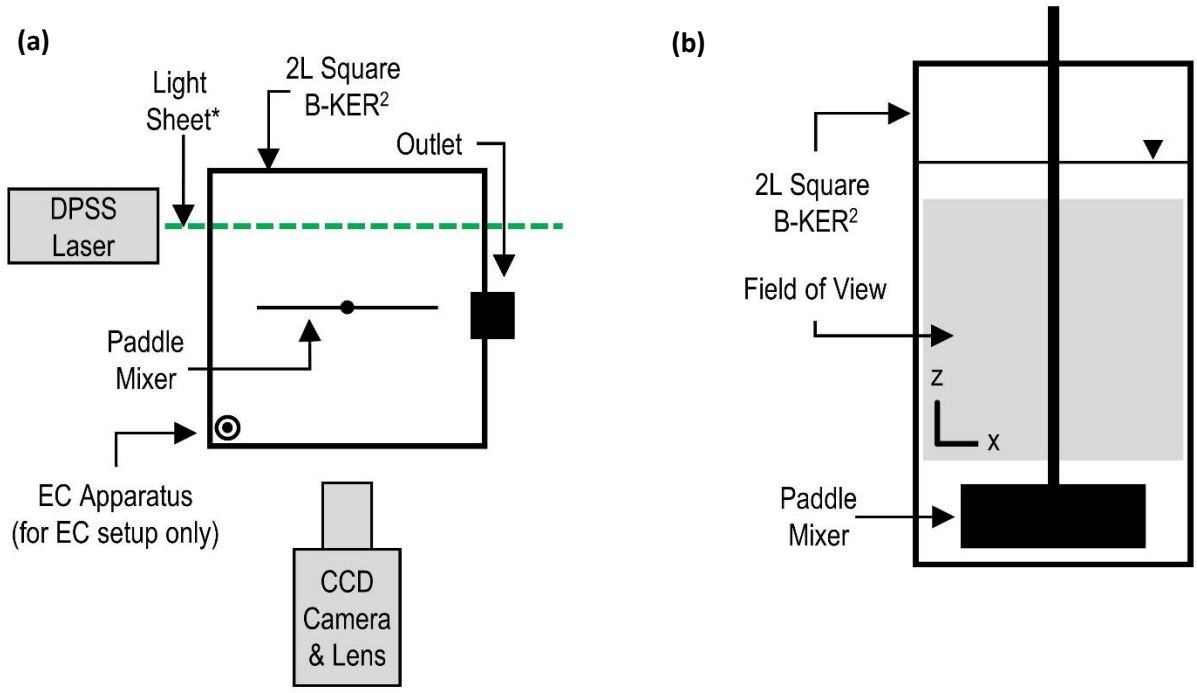

Figure 2: Schematic of experimental setup including (a) plan view and (b) profile view. *Note: light sheet optics not shown

The camera was operated an image capture rate of 100 fps. This rate was selected to provide sufficient images for flocculation and reactor mixing characterization while minimizing the total data quantity at each data collection instance. For larger data sets the data transfer duration is increased and is a limiting factor for the data collection rate. However, a robust data set is desired to obtain a general characterization of flocculation. Further, reactor mixing characterization is best informed by a lengthy data set that allows averaging of any periodic effects and fully characterizes the flow profile while also providing sufficiently high temporal resolution to maintain adequate correlation in the PIV analysis. Therefore, the image data set size was selected to provide enough

data for analysis while maintaining the desired data collection intervals. To enable synchronized data collection and comply with limited camera storage memory, the high-speed image recording was triggered by programmed analog signals sent from the NI USB-6259 device managed by LabVIEW programming. Images for flocculation characterization were collected at 1-minute intervals for 1 second, with an image capture rate of 100 fps, resulting in 100 images collected at each data collection instance. Images for reactor mixing characterization were collected at 3-minute intervals for 30 seconds, with an image capture rate of 100 fps, resulting in 3000 images collected at each data collection instance.

2.2. Image Processing and Flocculation Characterization

Images collected for flocculation characterization were first imported into MATLAB (version R2020b) and then processed using standard image processing techniques including background removal, contrast enhancement, binarization, and basic morphological corrections prior to floc identification. Image processing steps were conducted using MATLAB's Image Processing Toolbox. Although the camera used in this experiment is equipped with a 12-bit sensor, capable of capturing grayscale intensity values from 0 (black) to 4,096 (white), MATLAB software operates in 8-bit or 16-bit data formats. Therefore, to avoid resolution loss, images were first imported into MATLAB and then converted into a 16-bit format through linear pixel intensity rescaling. The result is a 16-bit image where the maximum intensity of the original image (4,096) is scaled to the maximum intensity of a 16-bit format (65,535). An example of the original image quality imported into MATLAB is provided in Figure 4(a).

A primary step in the image processing is background noise removal from the raw image which is present despite best laboratory practices due to the data collection method [58, 59]. If the noise is not removed in the early stages of image processing, subsequent steps can magnify this noise,

resulting in erroneous floc identification or sizing [5]. Background removal is typically performed via one of two methods. One method designates the background noise the average [58] or modal [60] intensity of a series of images in an image capture sequence. A second method for background noise removal is to remove the lowest intensity found in each pixel over all images in the image capture sequence, effectively treating the lowest intensity as the background noise [61]. For this experiment, the average intensity for each pixel, averaged over the specific data collection instance of 100 images captured over 1 second, was designated as the background noise and was removed from each image, as shown in Figure 4(b).

After background removal, the image contrast was enhanced to further distinguish the illuminated flocs from the background and reduce the fuzziness around the flocs which can result in an over-estimation of floc size [6]. The lighting setup clearly illuminates the portion of the floc in the laser sheet, but the floc borders are often less clear when flocs are transitioning through the focal plane and laser sheet, necessitating contrast enhancement. Although the image stores intensity data in a 16-bit format, the actual captured intensities do not occupy the full intensity spectrum; thus, there are "wasted' intensity ranges. Since the illuminated flocs appear bright against the dark background, pixel intensity rescaling within a targeted range was stretched to the maximum intensity values, making full use of the available intensity scales and further distinguishing the bright floc from the dark background. Further, since there was a clear anticipated intensity difference between the bright white floc and the dark black background, a non-linear intensity rescaling was applied using a gamma correction [5]. MATLAB's *imadjust* function, used for contrast enhancement provides for this gamma correction using a non-linear mapping parameter, gamma (γ). For gamma values greater than 1, pixel intensity remapping is weighted towards darker intensities. The result was a contrast-enhanced image that still displays the bright

white floc, but with a darker background. Based on a trial-and-error approach similar to that of Shen and Maa [5], three was selected as the gamma value and the bottom 25% of all intensities were selected to be rescaled using the non-linear intensity rescale to further reveal the illuminated flocs. An example of the impact of contrast enhancement is provided in Figure 4(c).

In the next image processing step, the contrast-enhanced greyscale image is converted into a binary image for more effective image processing and floc identification [62]. Binarization is accomplished by establishing a threshold above which a pixel will map to 65,535 (white) and below which a pixel will map to 0 (black). The result is a binary image useful for floc identification. The selection of this binarization threshold is highly subjective and dependent on the experimental setup in question [60, 62]. In an experiment with multiple data collection instances, the likelihood of a single global threshold value being suitable for all images is unlikely and thus an adaptive thresholding method is typically employed [5]. Three threshold settings (two adaptive and one global) for this experiment were evaluated by the trial-and-error approach and the resulting floc number size distributions were compared to evaluate the threshold's impact on the floc geometry results. Although the different thresholds resulted in slightly different floc distributions and total number, the normalized distribution was relatively similar among all the three thresholds (see Figure A-25 and Figure A-26). Since this investigation compares flocculation using both CC and EC and the raw imagery revealed significant differences in the temporal floc evolution, an adaptive threshold was employed to eliminate differences in the analysis that might arise solely from the use of different global thresholds. This adaptive threshold incorporated both the average and standard deviation of the averaged image and was applied to each image during the binarization process. Pixels intensities above this value were mapped to white (65,535) and pixels intensities

below this value were mapped to black (0), rendering a fully binary image, as shown in the example in Figure 4(d).

After image binarization, the images were further processed to clearly distinguish floc edges and correct floc morphology. In the binary image, flocs appear as cluster of white pixels, bordered by a mix of white and black pixels at the floc edges. In this border region, the mix of white and black pixels represent the transition from floc to the background. To establish a clear floc boundary, the exact transition from floc to background must be determined. To facilitate this, the gradient magnitude in the border region of each floc was evaluated using the Sobel method, which highlights the region of gradient change from white pixels to black pixels and effectively outlines the floc's estimated border. After the floc border is outlined, the interior is filled, resulting in a new floc that encompasses the border region and the original floc and ensures that any voids resulting from flocs aethereal nature are filled. While this step is necessary to clearly identify the transition from floc to background by eliminate stray white pixels at the floc edge, the process results in an overall increase in floc area that must be paired with a subsequent area decrease to ensure a good fit with the observable floc border. Erosion is commonly applied in binary image processing to remove white pixels along the edge of an identified object based on the shape of a structuring element. The structuring element should be of similar shape and size as the identified objects, to result in a morphological correction that aligns best with the original shape of the object. During erosion, the structuring element is iteratively applied over entire image. For a pixel to remain white, the structuring element must contain only white pixels. If any black pixels are contained within the structuring element, the border pixels within the structuring element are designated as black as shown in the example in Figure 3. Erosion is applied herein using a 4-pixel diamond as the structuring element to eliminate stray white pixels along the floc border, thus

facilitating a closer fit with the illuminated floc border, as shown in the example in Figure 4(e)(f). The size and shape of the structuring element were selected based on the anticipated size and shape of the smallest flocs during the experiment.

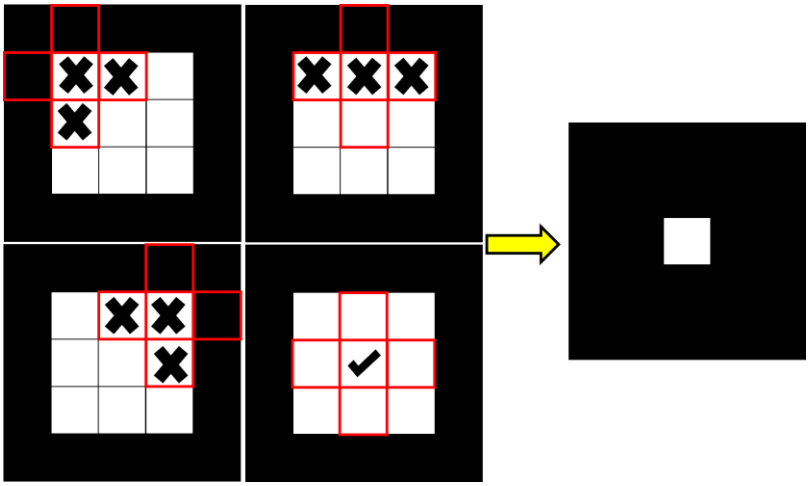

Figure 3: Erosion of a 9 x 9 object with a 4-pixel diamond structuring element (left). Note, not all iterations of the erosion are shown to obtain the final eroded figure (right).

Following the image processing steps, individual flocs are identified and labeled and then floc geometric properties are determined using MATLAB's Image Processing Toolbox. Geometric properties utilized in this investigation include the floc area, equivalent diameter, and major and minor axes. Floc area is determined by the number of pixels identified as part of each floc. Based on this area, the floc equivalent diameter is calculated by assuming the floc shape is a perfect circle. Information on the floc's major and minor axis lengths is obtained by determining the length of major and minor axes of ellipse with an equivalent normalized second central moment of inertia as the identified floc.

After all flocs were identified and geometric properties were determined, a filter was applied to remove flocs too small for accurate size determination and to eliminate flocs not fully

captured by the field of view along the image border. Past investigations have taken several approaches to determine the smallest minimum floc size suitable for size and shape analysis. Shen and Maa [5] only considered objects with areas of at least four pixels and minor axis lengths at least two pixels while Mikkelsen et al., [63] utilized nine coherent pixels as the minimum criteria. For this study, a floc is considered reliable for subsequent analysis if the floc has a total area of at least four pixels and minor axis length of at least two pixels. Once the filtered floc data sets were available for each data collection instance, the data sets were averaged to provide a general floc geometric characterization to be used in subsequent analyses. Flocculation characterizations were not anticipated significantly change between the consecutive images due to the low time differential (0.01 seconds). Thus, to minimize data storage and processing time, only alternating images were analyzed and averaged, resulting in a flocculation characterization based on 50 images collected over 1 second.

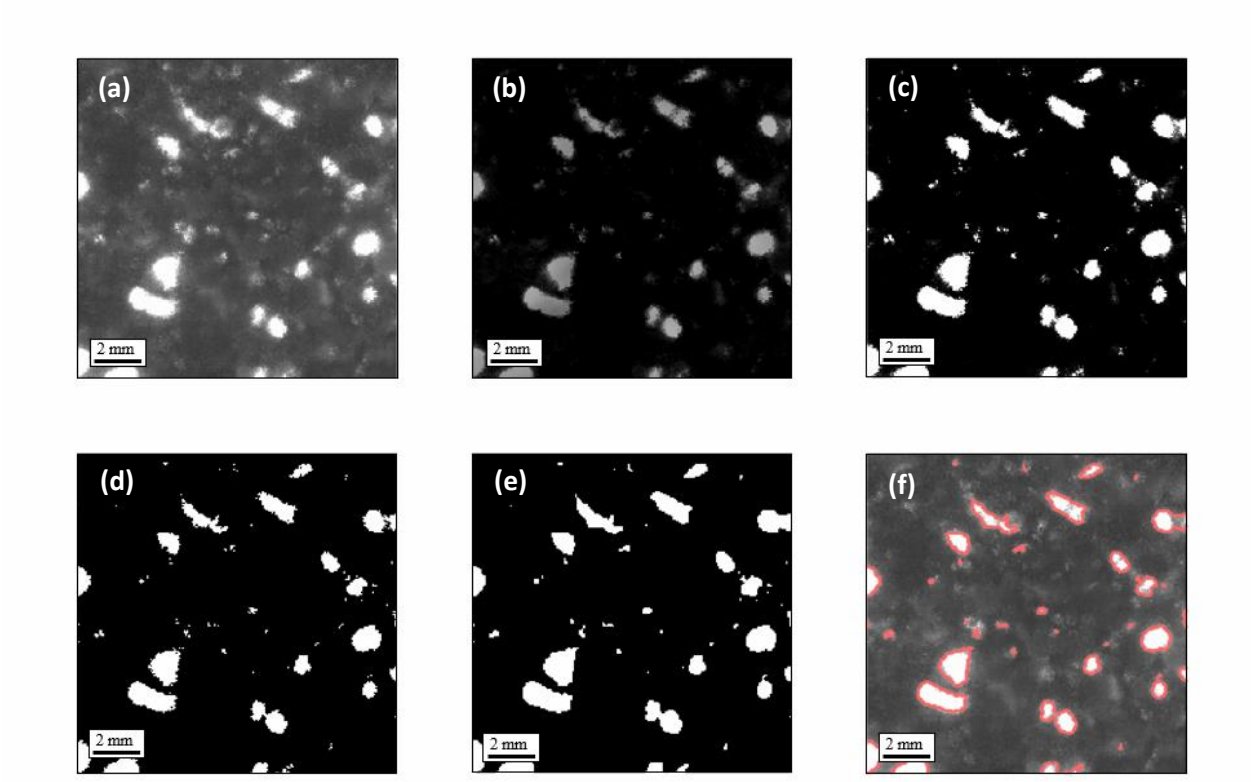

Figure 4: Summary of image processing steps: (a) raw image; (b) image with background removed; (c) contrast-enhanced image; (d) binary image; (e) image with morphological corrections; (f) raw image with floc border

2.2.1. Two-Dimensional Fractal Dimension

The length-based fractal dimension, D_2 for the CC and EC floc distributions was obtained through a linear regression of the floc area against its major axis length on a log-log plot for the total number of flocs identified over the entire data collection instance and did not rely the data set average. By evaluating the fractal dimension with the complete data set, the linear regression is informed by a larger number of flocs to more accurately capture the trend between floc area and equivalent diameter. For each data collection instance, D_2 is determined as the slope of the linear regression, per Equation 1 and shown in the example plot in Figure 5.

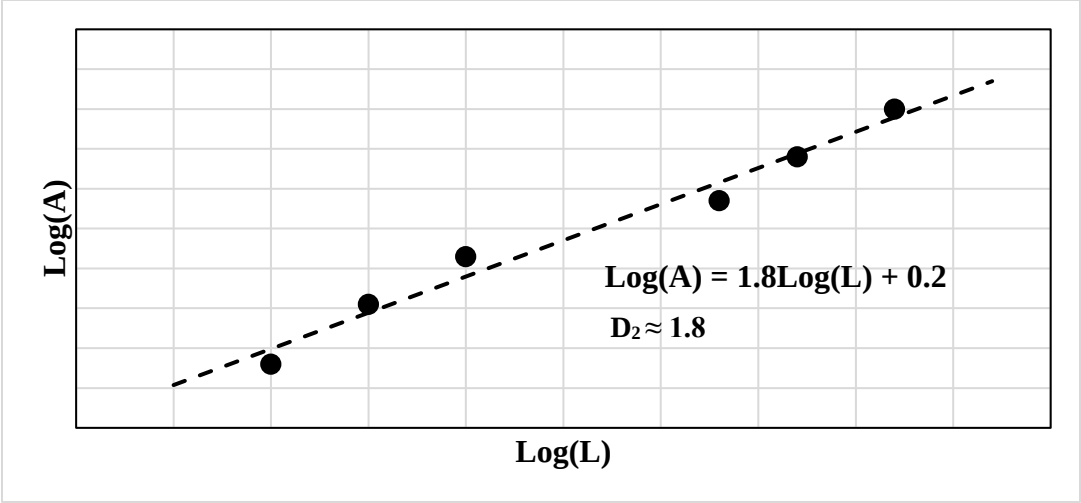

Figure 5: Example derivation of D_2 for a hypothetical floc data set with known areas and characteristic lengths

2.2.2. Flocculation Characterization Validation

Although the *in-situ* image analysis methodology used herein is beneficial as it is a non-disruptive measurement technique, several factors, including the position of the floc within the light sheet or focal plan, or selection of different image processing parameters can impact the accuracy of floc size determination. If a floc is partially within the light sheet or focal plane, part of the floc will appear clear and illuminated, while the other part will appear blurry and dark, impacting the measured floc size which is based on the illuminated portion only. In this investigation, the depth of field (4 mm) is larger than the light sheet thickness (2.3 mm), so the floc's position within the light sheet is the limiting factor. To evaluate the impact of floc position within the light sheet, a simple Monte Carlo simulation was performed by randomly placing a hypothetical, spherical floc at various locations within the light sheet and determining the frequency at which the floc size was accurately measured based on the illuminated portion of the sphere. For each hypothetical floc size, the distribution of measured floc sizes was compared with

the actual size and plotted in terms of its probability of occurrence (Figure 6(a)). The probability of the measured to actual floc diameter ratio was evaluated for floc sizes ranging from 0.2 to 7 mm based on the expected equivalent floc diameter range in this investigation. To provide a generalized estimate of how frequently measured floc diameters would be near their actual diameter, Figure 6(b) displays the measured floc diameter range for 75% of all random floc placements for a particular floc diameter. Two laser light sheet thicknesses were evaluated to determine the impact of the laser light sheet thickness on accurate floc size measurement. The laser light sheet thickness of 2.3 mm represents the laser light sheet used in this experiment, while the laser light sheet thickness of 4.0 mm is a hypothetical thickness used for comparison purposes.

Based on the Monte Carlo simulation, larger particles had a higher probability of being incorrectly measured when compared to smaller particles. While this Monte Carlo simulation is performed assuming perfectly spherical flocs, flocs are best described as fractal shapes as discussed in Section 1. However, regardless of floc shape, measurement error due to location within the laser light sheet is expected to only underestimate floc size following the trends of this Monte Carlo simulation due to the nature of the floc illumination and measurement of the projected illuminated area. Particularly, floc size underestimation is expected to be more pronounced when smaller laser light sheet thicknesses are employed (Figure 6(b)). This Monte Carlo simulation is useful to generalize measurement error in due to the methodology but is not intended to provide a method for measurement error correction. Rather, results of this Monte Carlo simulation provide insights into methods to reduce anticipated measurement error, such as increasing the laser light sheet thickness, which results in a closer adherence of the measured to actual floc diameter as shown in Figure 6.

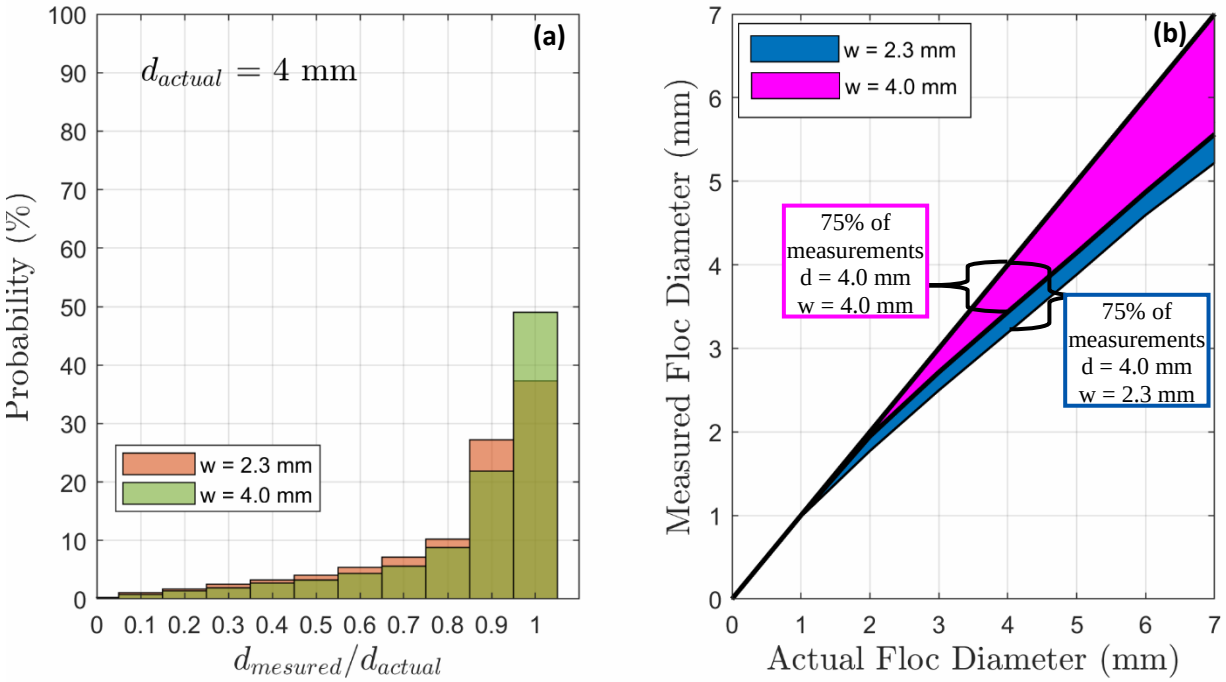

Figure 6: Monte Carlo simulation to determine the probability a spherical floc will be accurately measured based on location within the laser light sheet with two different light sheet thicknesses, w (w = 2.3 mm and w = 4.0 mm); (a) probability distribution of measured to actual floc sizes for an example 4 mm spherical floc; (b) range of 75% of all measured diameters for a given actual floc diameter

2.3. Particle Image Velocimetry and Reactor Mixing Characterization

2.3.1. Particle Image Velocimetry Analysis

Velocity field estimation using PIV is typically accomplished by adding artificial particles to the fluid and then tracking their displacement. The particle characteristics (e.g., diameter, reflectance, density) are selected based on the experimental conditions (e.g., fluid velocity, field of view, lighting conditions, fluid properties) such that the particles follow the flow streamlines without impacting the flow itself [32, 56, 64]. To enable the simultaneous characterization of

flocculation and reactor mixing, a PIV analysis using artificial particles is impractical as the particles would obscure clear floc imaging and measurement and would become enveloped in the floc throughout the experiment, ultimately impacting flocculation characterization. Therefore, flocs generated by CC and EC are used as tracking particles in this investigation since they are critical in the flocculation characterization and are expected to follow the fluid motion without impacting the flow, considering their density and porosity. To ensure quality correlations between image pairs, a minimum of 10 tracking particles is suggested [31] and a homogenous particle distribution is key to reduce bias in velocity results [64]. During flocculation, the flocs generated by CC and EC change in size distribution and number and thus use of flocs as tracking particles for PIV analyses may be more optimal at different stages in flocculation.

The reactor mixing data sets were analyzed using a combination of two open-source particle image velocimetry software fully within the MATLAB platform: PIVLab [65] and MPIV [66]. By combining these two software, both the strong FFT cross-correlation core of PIVLab and the robust post-processing schemes of MPIV were leveraged in this analysis. The PIVLab FFT cross-correlation core is equipped with autocorrelation suppression, which suppresses the impact of image background noise on the cross-correlation process. The autocorrelation suppression facilitates detection of the correlation peak representing the actual particle displacement instead of background noise, which would have a zero displacement [65]. In preliminary trials, pre-processing of the reactor mixing image data sets were determined to be unnecessary prior to PIV analysis and autocorrelation suppression was used to reduce impacts of background noise on the results.

PIV analysis was performed using an iterative multi-pass algorithm for linear window deformation, starting with an interrogation window size of 64 by 64 pixels and ending with a

window size of 32 by 32 pixels in the second pass with a 50% overlap for both passes. The larger initial interrogation window was selected to capture large particle displacements. The smaller final interrogation window size was selected to maximize the resulting velocity grid resolution and thus capture the dissipative scales of turbulent motion while also maintaining an adequate number of particles for correlation between image pairs. Although a smaller final interrogation window size would increase the velocity field resolution, heightened spatial resolution without a sufficient number of tracking particles would result in high errors that would compound in subsequent turbulent analyses, yielding questionable results [27, 31, 45, 67]. Additionally, the average floc equivalent diameter was expected to be in the range of 5 to 7 pixels, with some flocs reaching much greater sizes; thus, the interrogation window size was selected to ensure several flocs could be viewed within the final interrogation window.

3000 images were obtained during each velocity data collection instance (3000 images over 30 seconds every three minutes), resulting in a time step of 0.01 seconds between each image pair. The mixing speed was such that the floc displacement calculated using the PIV analysis above was relatively small (< 3 pixels) for a majority of the vectors. Even with ideal experimental conditions, the total error cannot be fully eliminated and contributes approximately 0.1 pixels to the calculated particle displacement [64, 68]. For small displacements, this total error constitutes a significant portion of the displacement vector, leading to erroneous velocity estimates. Therefore, to reduce the influence of error on the final results, image pairs with sufficient time differentials to induce larger displacements should be analyzed. At the same time, the tracking particle displacement should be small enough that the PIV processing algorithm can effectively track the particle. If particles move too much between in an image pair, most particles could escape the current interrogation window and the PIV program will poorly correlate the particle displacement,

resulting in erroneous velocity estimates. The result is that image pairs should be selected such that there is sufficient time for the particles to travel an adequate distance to minimize the impact of total error on overall results but not so much time such that particles travel more than 25% of the smallest interrogation window size [51, 69]. For the present study, image pairs were selected with a time differential of 0.02 seconds by trial-and-error, resulting in a sample size of 1,500 image pairs over the data collection period of 30 seconds.

Spurious vectors were removed through standard deviation and median filtering and the resulting displacement data was converted into velocity data using the known time differential (0.02 seconds) and the pixel length conversion (67.5 μm per pixel). The resulting velocity grid contained 9,801 horizontal and velocity vectors (99 by 99 grid), at a spatial resolution of 1.1 mm (16 pixels), each element containing 1,500 data points documenting the velocity variation over the 30 second data collection period. The center region of each image and corresponding vector field was omitted from subsequent analyses due to the mixing shaft's interference with the measurement. Additionally, noisy edge regions at the image border were not considered in subsequent analyses.

2.3.2. Particle Image Velocimetry Control

Reactor mixing characterization analyses were performed in duplicate for both CC and EC. In addition, a separate reactor mixing analysis using distilled water artificially seeded with polyamide particles (Danteck Dynamics, 50 μm mean particle size, 1.03 g/cm^3) was performed as a control and was not performed in duplicate. These polyamide particles are commonly used in PIV measurement for determining fluid kinematics. Reactor mixing conditions and water temperatures were the same as the analysis performed using CC and EC flocs. For the artificially

seeded analysis, laser power was lowered to 5W as less light was required for clear illumination of the seeding particles with their relatively high reflecting nature.

2.3.3. Turbulent Flow Detection

The presence of turbulent flow was evaluated through a spectral analysis of the temporal velocity signal. Each velocity grid element contains a time series of 1,500 velocity data points over the 30 second data collection period, corresponding to the number of image pairs evaluated in the PIV analysis. Due to the removal of spurious vectors, certain velocity grid elements do not have velocity information for all 1,500 velocity data points. A spectral analysis was performed for grid element containing velocity information for at least 90% of the time series (i.e., velocity grid elements with 150 or more spurious vectors out of 1,500 were not evaluated). If at least 90% of the time series was available for analysis, missing velocity information was replaced using linear interpolation based on surrounding time series data. After mixing velocity information was replaced, the velocity signal for each grid element was converted into the frequency domain through the FFT and then the energy spectrum was calculated as per Equation 14. The energy spectrum was evaluated at the left top, left middle, and left bottom regions of the cross section for a 9 x 9 subset of velocity grid elements, which were then averaged to produce a characteristic spectrum for each data collection instance region.

3. RESULTS

Based on the methodology described in Section 2, flocculation and reactor mixing characterization experiments were performed for CC and EC experiments, along with a control experiment for reactor mixing using artificial beads as tracking particles. A summary of the data sets and their roles are described in Table 1. Data set #1.b was used as both the data set for reactor mixing characterization and control as well as the duplicate test for flocculation characterization, highlighting the unique aspect of this methodology where both flocculation and reactor mixing can be characterized using the same data set.

Table 1: Summary of Data Sets and Roles

Data Set (DS)	**Role**
DS#1.a	Flocculation Characterization (reported herein)
DS#1.b	Reactor Mixing Characterization (reported herein) Reactor Mixing Control (reported herein) Flocculation Characterization Duplicate (reported in Appendix B)
DS#2	Reactor Mixing Characterization Duplicate (reported in Appendix C)

3.1. Flocculation Characterizations

Flocculation characteristics of interest in this investigation include the temporal evolution of the floc size distribution, the maximum floc size produced, and the fractal dimension. Each of these characterizations is informed by the image processing steps, floc identification, and filtering outlined in Section 2.

3.1.1. Floc Size Distribution

Floc size is characterized herein by the floc's equivalent diameter based on the projected floc area, which is a commonly used characterization of floc size [25, 26, 70]. Although flocs are irregularly shaped and the floc equivalent diameter is unlikely to represent an actual floc length,

this method provides a means to quantify and observe temporal changes in floc size, facilitating comparisons among independent investigations. Floc size distributions presented herein represent the size distribution captured in the single cross section (10.8 cm by 10.8 cm) with a depth of approximately 2.3 mm based on the laser light sheet thickness, resulting in a total analyzed volume of approximately 26.8 mL. Therefore, these distributions reveal how floc size distribution and number evolve, with the understanding that the total floc quantity within the reactor is much greater. Additionally, based on the image resolution (67.6 μm per pixel) and the size criteria established for minimum detectable flocs (area greater than 4 pixels), the minimum detectable floc equivalent diameter in this investigation is approximately 153 μm. Since flocs smaller than 4 pixels are undoubtedly present especially during early flocculation stages the actual floc quantity is likely higher than represented in these results.

Floc cumulative counts and size distributions are presented in Figure 7 at different times during flocculation for CC and EC. Floc generation exhibits a more rapid initial growth phase for CC, as shown by a higher cumulative particle count early during flocculation (Figure 7(a)), reaching approximately 1,400 flocs (~52 flocs/mL) at 2 minutes compared to 225 flocs (8.4 flocs/mL) for EC at the same time (Figure 7(b)). This rapid initial growth phase for CC is also observed in the floc size distributions (Figure 7(c)), which exhibit an earlier transition to lager floc sizes than EC (Figure 7(d)). In contrast to CC, flocs generated using EC exhibit a slower initial growth phase, but ultimately reach a higher total floc count later in flocculation, with a maximum floc count of 1,750 flocs (65 flocs/mL) at 23 minutes. The floc count for CC reaches its maximum value much earlier, with approximately 1,400 flocs (~52 flocs/mL) present at 2 minutes. This slower initial growth phase is observed in the EC's floc size distribution evolution, which depicts a slower transition from smaller to larger floc sizes.

Although the CC floc size distribution initially exhibits a more rapid shift to larger floc sizes, as flocculation proceeds, the floc size distribution shifts to a higher frequency of smaller flocs paired with an increase in flocs larger than 2,400 μm. During this phase, the overall cumulative count decreases from its maximum value, likely due to the flocculation of smaller flocs into larger flocs. During the latter half of flocculation, the total floc count oscillates between 600 (22 flocs/mL) and 1,000 (37 flocs/mL) and the maximum floc size fluctuates between 3,000 and 4,000 μm. In this stage, the floc size distribution remains relatively stable, indicating the CC experiment reached a pseudo steady-state condition. Such oscillations were not observed in the temporal evolution of the floc size distribution for EC. Rather, as flocculation proceeded, EC exhibited a gradual shift towards larger flocs as shown in Figure 7(d) with the cumulative particle count increasing up to approximately 24 minutes of flocculation and then steadily decreasing to the end of data collection (Figure 7(b)). In contrast to CC, EC produced fewer flocs larger than 2,400 μm and instead maintained a larger frequency of medium sized flocs between 1,000 and 2,000 μm towards the end of the experiment. The floc size distribution for EC exhibits a slight shift to larger particle sizes between 27 and 37 minutes and although the rate of change in size distribution and cumulative particle count appears to slow towards the end of data collection, the EC experiment does not appear to reach the same pseudo steady-state condition as CC. Similar trends are observed in the duplicate test for CC and EC and the results are presented in Figure B-39.

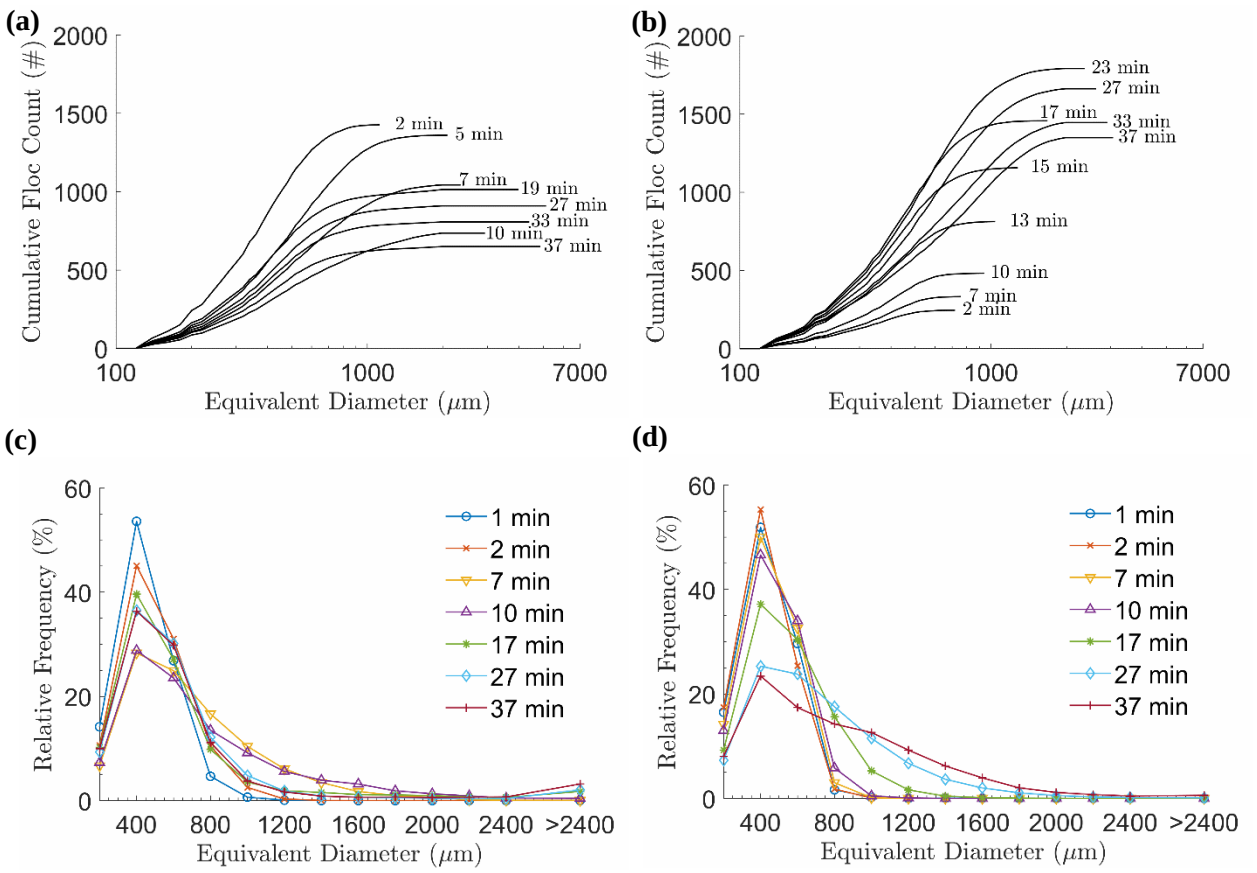

Figure 7: Temporal evolution of floc size for DS#1.a including: (a) cumulative floc count for CC; (b) cumulative floc count for EC; (c) floc size distribution for CC; (d) floc size distribution for EC. Note: Floc size distributions were obtained by accumulating the total number of flocs for size intervals of 200 μm and are represented by a data point at the maximum of the size interval.

3.1.2. Mean Floc Size

While the floc size distributions reveal shifts in the entire floc size range over time, examination of the trends and maximum and mean floc size also provides insights into the different flocculation characteristics of CC and EC. The top 10% mean floc size is determined as the mean of the top 10% of flocs ranked by their equivalent diameter. The total mean floc size is determined as the mean of all flocs identified in the cross section. Figure 8 displays the temporal evolution of these mean values for both CC and EC flocs. While CC exhibits an initial increase in the mean

floc size during the first 11 minutes, afterwards decreasing slowly and reaching a pseudo steady-state at around 20 minutes, the mean floc size for EC exhibits a monotonically increasing trend after 2 minutes and does not obtain a steady-state during the experiment. The top 10% mean floc size follows a similar trend as the mean floc size for both CC and EC. The top 10% mean floc size for CC increases until approximately 15 minutes, after which it fluctuates but averages to approximately 1,750 μm for the remainder of flocculation. In contrast, the top 10% mean floc size for EC increases throughout flocculation, increasing rapidly after approximately 10 minutes and until 31 minutes, where it increases at a slower rate. Given the resolution limitations, the mean total floc size presented here likely overestimates the actual total mean floc size as flocs with equivalent diameters less than 153 μm are not included in the floc identification. This impact is expected to be more pronounced earlier in flocculation where smaller flocs generally constitute a larger portion of the total floc number. Similar trends are observed in the duplicate test for CC and EC (Figure B-40) as shown in the parity plots for both the top 10% mean and the total mean in Figure 9 and Figure 10.

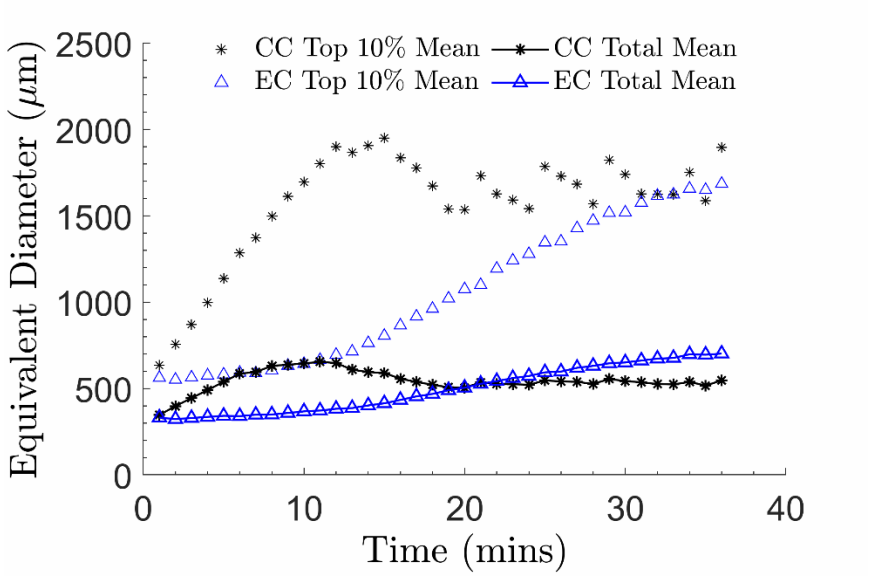

Figure 8: Temporal evolution of floc mean size for CC and EC in terms of the total mean and the top 10% mean for DS#1.a.

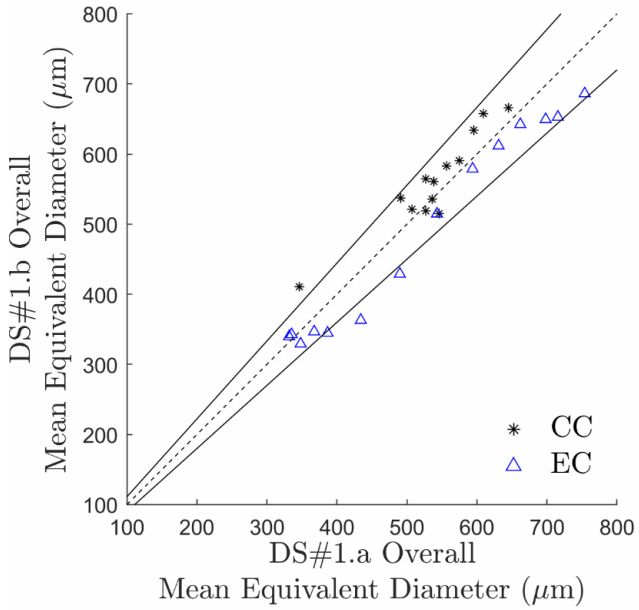

Figure 9: Parity plot of the overall mean equivalent diameter for CC and EC experiments for duplicate tests (DS#1.a and DS#1.b). The dashed line represents complete agreeance of the two data sets. The solid lines represent +/- 10% off the values of the dashed line.

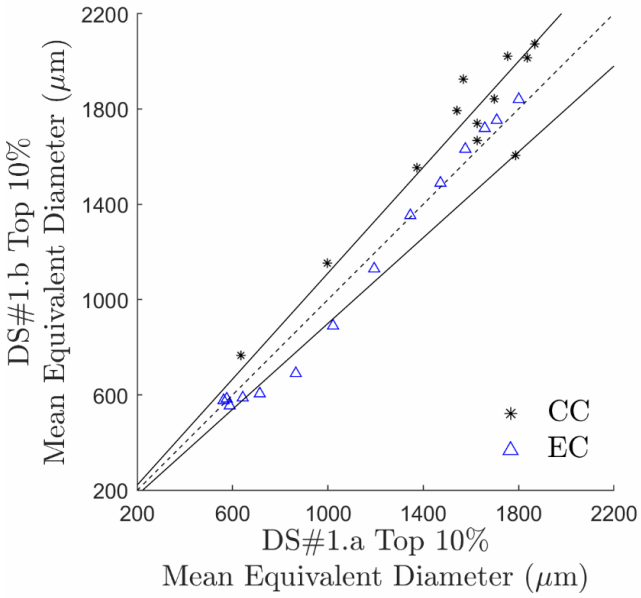

Figure 10: Parity plot of the top 10% mean equivalent diameter for CC and EC experiments for duplicate tests (DS#1.a and DS#1.b). The dashed line represents complete agreeance of the two data sets. The solid lines represent +/- 10% off the values of the dashed line.

3.1.3. Two-Dimensional Fractal Dimension

The 2D fractal dimension, D_2, is presented in Figure 11 for CC and EC. The fractal dimension for flocs produced using CC exhibited an initial rapid increase until approximately 4 minutes followed by a slight decrease before achieving steady state at approximately 20 minutes. Flocs produced using EC exhibit a lower initial fractal dimension than CC which increases slowly until 11 minutes, after which the fractal dimension rises rapidly until 20 minutes. After this period of rapid increase, the fractal dimension rises slowly, ultimately reaching a higher fractal dimension than CC by the end of flocculation. These temporal patterns are consistent with both the floc size distributions and mean size characterizations. Temporal fractal dimension variations for both CC and EC exhibit a trend towards a higher 2D fractal dimension, indicating a shift towards a more spherical, and compact, and less porous floc throughout flocculation [1, 6, 35]. Similar trends were

observed in the duplicate test results, included as Figure B-41 and as shown in the parity plot in Figure 12.

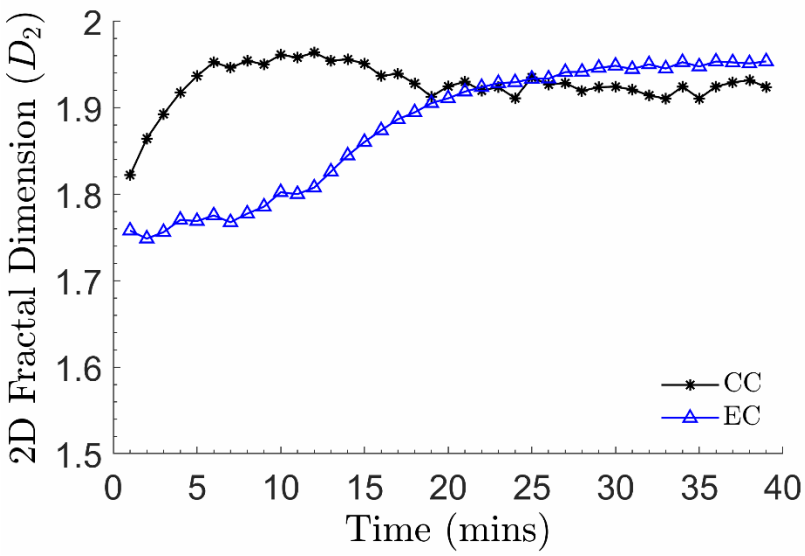

Figure 11: Temporal evolution of the 2D fractal dimension for CC and EC experiments of DS#1.a

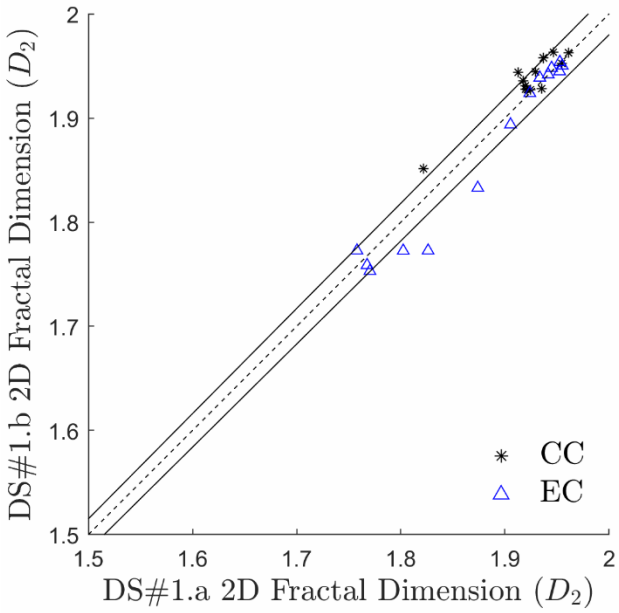

Figure 12**:** Parity plot of the 2D fractal dimension data for CC and EC experiments for the duplicate tests (DS#1.a and DS#1.b). The dashed line represents complete agreeance of the two data sets. The solid lines represent +/- 1% off the values of the dashed line.

3.2. Reactor Mixing Characterizations

In this section, reactor mixing is characterized using the velocity information obtained using PIV. First, the velocity field is evaluated to determine its suitability for turbulent flow analyses by evaluating the percentage of rejected, spurious vectors and through a spectral analysis of the time-series velocity data. Secondly, the 2D turbulence intensity, I_{2D}, is evaluated as a basic indicator of the turbulence level within the reactor. The local TKED rates within the reactor are then evaluated and compared with the average TKED rate for the entire cross section. As a final reactor mixing characterization, the time and length scales of turbulent motion are determined based on the average and range of the TKED rate. Comparative results are presented for a subset of data comparing reactor mixing characterizations from velocity information obtained using both flocs generated *in-situ* (CC and EC) and artificial beads as tracking particles. The reactor mixing

experiments were performed in duplicate and comparisons between the data reported herein (DS#1.b) and the duplicate test (DS#2, reported in Appendix C), are provided both herein and in Appendix D.

3.2.1. Flow Field Evaluation

Each data set was first evaluated to determine the percentage of spurious vectors. Vector fields with higher than 5% rejection were not evaluated. Secondly, each dataset was then evaluated to determine if it exhibits the Kolmogorov -5/3 spectrum when viewed in the frequency domain, indicating turbulent flow [44]. The flow fields measured using CC flocs exhibited a low vector rejection rate throughout the entire duration, never exceeding the 5% vector rejection threshold as shown in Figure 13. Additionally, the spectral analysis of the flow fields measured using CC flocs exhibited a clear adherence to the Kolmogorov -5/3 spectrum from the first data collection instance (2 minutes) until approximately 23 minutes, after which the energy spectrum deviated from the Kolmogorov -5/3 spectrum. In contrast, the flow fields measured using EC flocs were marked by insufficient correlations and poor adherence to the Kolmogorov -5/3 early in flocculation (prior to 14 minutes) with vector rejection rates exceeding the 5% vector rejection threshold between 5 and 11 minutes (Figure 13), indicating the velocity data was unreliable during this period. By 14 minutes, the flow field measured using EC flocs achieved sufficient correlations and exhibited close adherence to the Kolmogorov -5/3 spectrum until approximately 29 minutes. The artificially seeded experiment exhibited a low vector rejection rate (<1%) and adherence to the Kolmogorov -5/3 spectrum. Results reported herein are based solely on data sets that maintained less than a 5% vector rejection rate and exhibit the Kolmogorov -5/3 spectrum when viewed in the frequency domain.

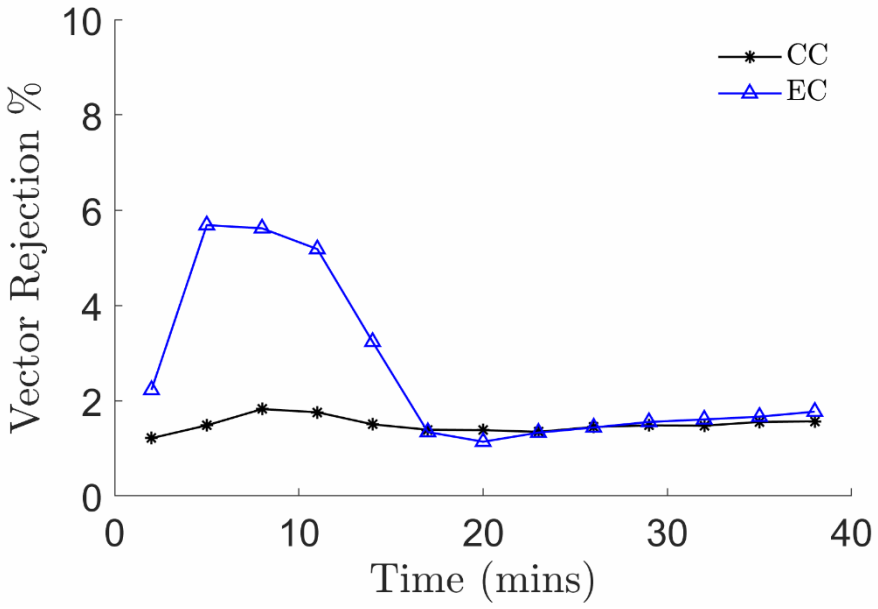

Figure 13: Vector rejection percentage for CC and EC experiments of DS#1.b.

The spectral analysis results for the left center of the cross section are presented in Figure 14 for both CC and EC, respectively. Analysis was performed for both the horizontal (U) and vertical (W) component of the velocity time series data. Significant differences were not observed between the results for horizontal and vertical time series data. Complete results documenting the horizontal (U) and vertical (W) components of the velocity time series at the beginning (2 minutes), middle (17 minutes), and end (38 minutes) of flocculation are provided in Figure A-27 and Figure A-28 for CC and EC, respectively. The artificially seeded system was not impacted by flocculation time thus a single time instance is reported in Figure A-29.

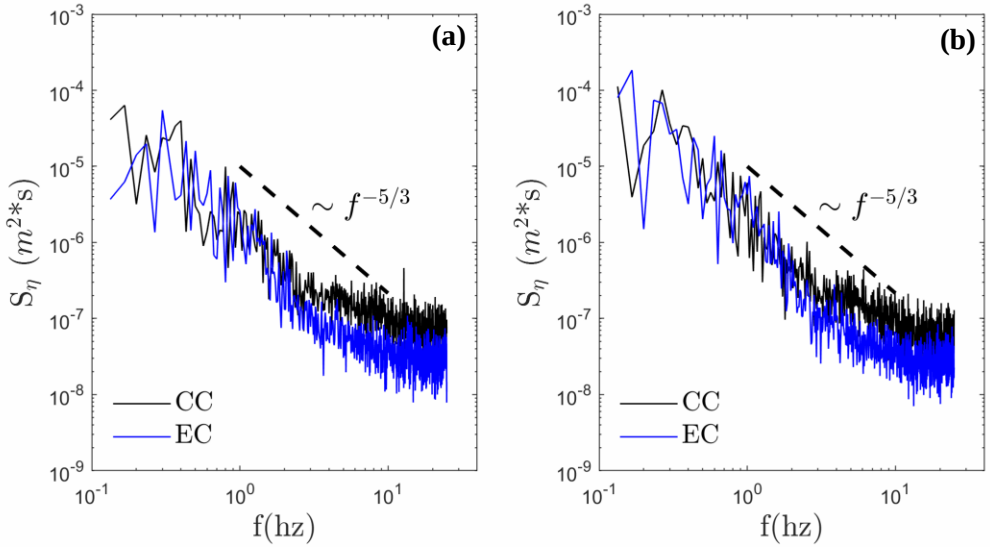

Figure 14: Energy spectrum for the: (a) horizontal (U) velocity components and (b) vertical (W) velocity components for CC at 11 minutes and EC at 20 minutes of DS#1.b for the left center of the field of view (x = 2.7 cm, z =5.4 cm).

The duplicate test results (Appendix C) indicate a wider range of data suitable for turbulent analyses, but also exhibit similar trends in terms of vector rejection rates (Figure C-42), where the EC experiment has a high vector rejection rate early in flocculation The spectral analysis results for the left center of the cross section are presented in Figure C-43 and Figure C-44. Based on the vector rejection rates and the spectral analysis results, data sets from 14 minutes to 38 minutes for the EC experiment and from 2 minutes to 38 minutes for CC were suitable for turbulent flow analyses.

The Reynold's numbers for the experiment was evaluated based on the reactor diameter as the characteristic length and a characteristic velocity derived using the mixing speed and diameter of the mixing impeller. Based on this evaluation, the Reynold's numbers for slow and rapid mixing phases are 6,030 and 40,200, respectively, both of which are in the turbulent flow regime. Although

some data sets were rejected for not meeting the vector rejection criteria or the Kolmogorov -5/3 spectrum criteria, these rejected data sets were subjected to the same mixing conditions and likely were within the turbulent flow regime as the data sets deemed suitable for further turbulent analyses. Therefore, these data sets were rejected, not because they were captured non-turbulent flow, but rather because the velocity information obtained was insufficient or too noisy to accurately portray the turbulent flow within in the reactor.

3.2.2. Turbulence Intensity

The average 2D turbulence intensity (I_{2D}) for the turbulent flows of the CC, EC, and artificially seeded experiments are presented in Figure 15, Figure 16, and Figure 17 respectively. For each experiment, the I_{2D} is highest at the bottom of the cross section directly above the paddle mixer. Additionally, for each experiment, the I_{2D} exhibits an asymmetry in the horizontal distribution, skewing to higher I_{2D} values in the direction of the mean velocity ($\overline{U}$). A similar trend of horizontal asymmetries in the mean flow direction was observed in the duplicate test (Figure C-45 and Figure C-46) which had a mean velocity in the opposite direction.

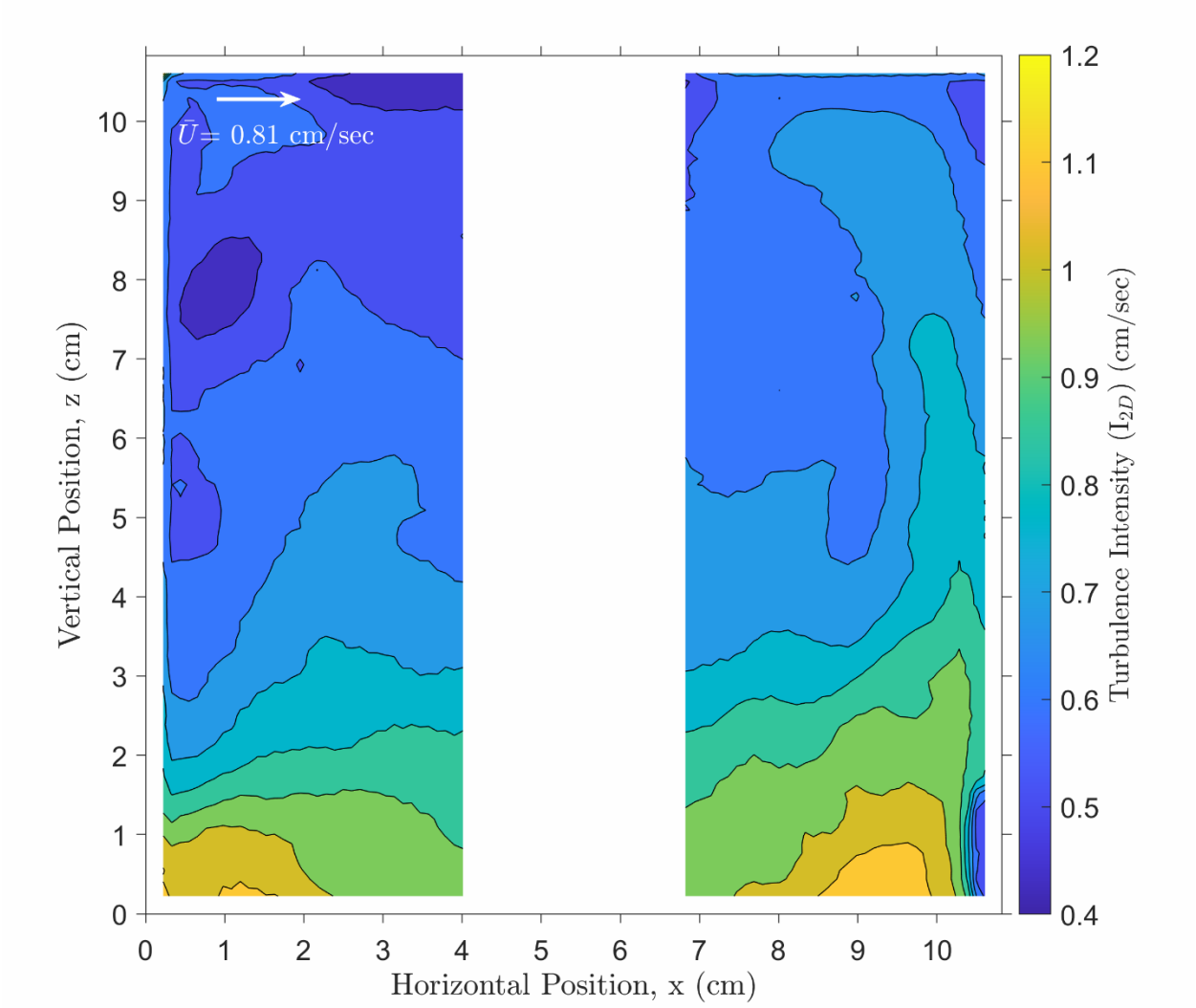

Figure 15: Average 2D turbulence intensity for the CC experiment of DS#1.b. Average mean velocities in the horizontal and vertical directions are 0.81 cm/sec and 0.02 cm/sec, where positive values velocities in the positive x (horizontal) and z (vertical) direction as shown.

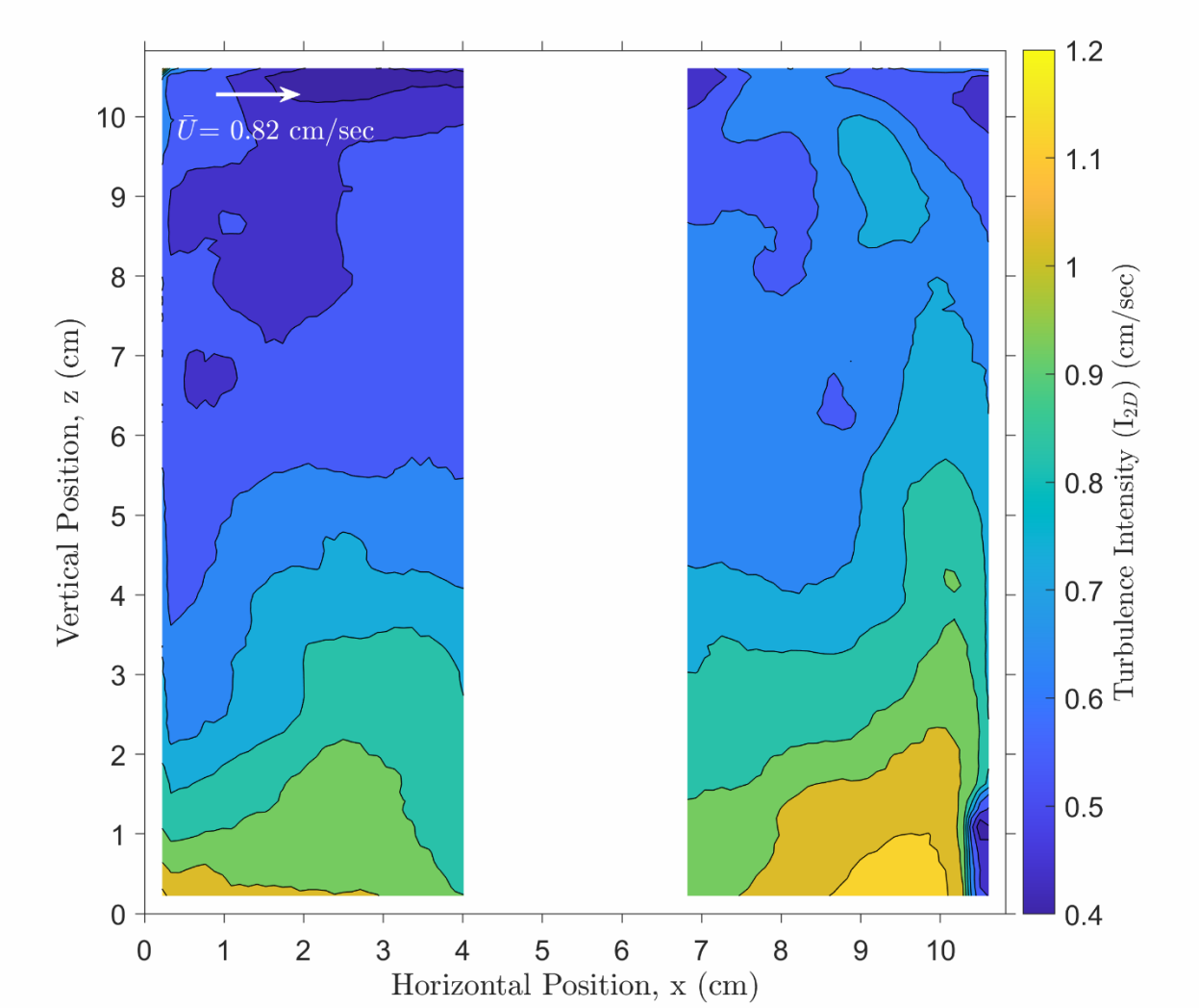

Figure 16: Average 2D turbulence intensity for the EC experiment of DS#1.b. Average mean velocities in the horizontal and vertical directions are 0.82 cm/sec and 0.02 cm/sec, where positive values velocities in the positive x (horizontal) and z (vertical) direction as shown.

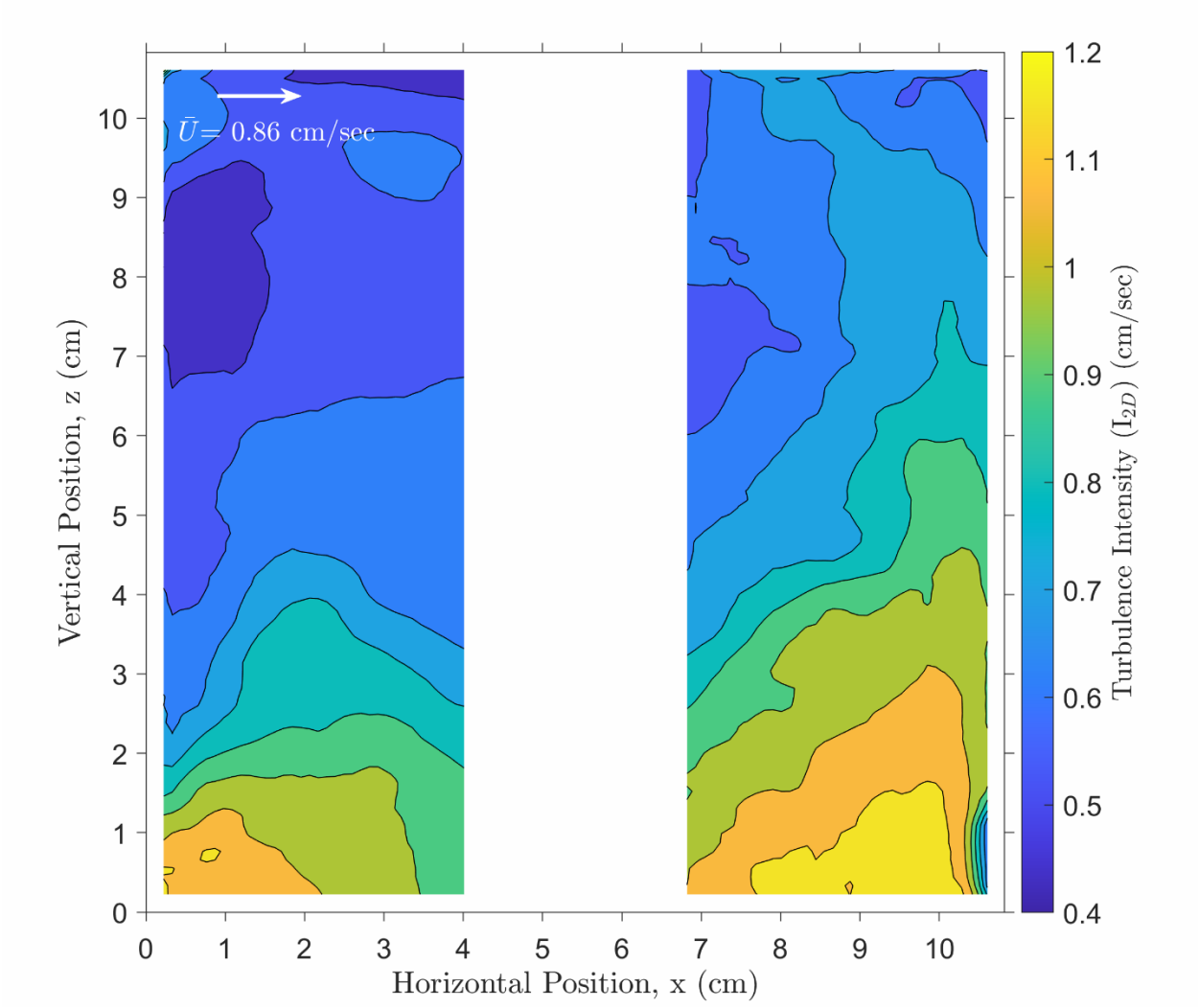

Figure 17: Average 2D turbulence intensity for the artificially seeded experiment of DS#1.b. Average mean velocities in the horizontal and vertical directions are 0.86 cm/sec and 0.01 cm/sec, where positive values velocities in the positive x (horizontal) and z (vertical) direction as shown.

In addition to the visual comparison between the CC, EC, and artificially seeded systems, and between the two duplicate tests, I_{2D} was also compared among each of the different valid flow data sets, as shown in Table 2. As each of the individual experiments were performed at the same mixing speed, I_{2D} was expected to be similar. To quantitively evaluate difference between the individual data sets, the ratios of the mean I_{2D} were compared amongst the two floc-seeded

experiments (CC and EC) for both of the duplicate tests (DS#1.b and DS#2), as shown in Figure A-30 and Figure C-47 and across the duplicate tests (e.g., DS#1.b vs. DS#2), as shown in Figure D-54 and Figure D-55. Comparisons within each of the duplicate test data sets indicate a similar result for reactor mixing characterization by the floc-seeded experiments, as shown by a mean ratio value of approximately one in Table 2. When the two duplicate tests were compared, DS#1.b had a higher I_{2D} on average than DS#2 for both the CC and EC experiments, as shown by a mean ratio value greater than one in Table 2.

Table 2: 2D turbulence intensity data comparison between CC, EC, DS#1.b and DS#2

Data Source	**DS#1.b**	**DS#2**	**CC**	**EC**
Comparison	**CC:EC**	**CC:EC**	**DS#1.b:DS#2**	**DS#1.b:DS#2**
Mean Ratio	1.01	1.00	1.14	1.13
Standard Deviation	0.07	0.07	0.16	0.17

Additionally, the relative difference was evaluated between the floc-seeded experiment for DS#1.b and the artificially-seeded experiment, which acts as the control and is assumed as the more accurate experiment. Results from the relative comparison between indicate the CC and EC floc-seeded experiments had an average percent relative difference compared to the artificially-seeded experiment of approximately 7.7% and 8.0%, respectively. The absolute values of the relative difference are provided visually in Figure A-31 and Figure A-32.

3.2.3. Turbulent Kinetic Energy Dissipation Rate

The TKED rate was evaluated using the five equations presented in Section 2 for all velocity data sets suitable for turbulent flow analysis as shown by the vertical TKED rate distributions at various horizontal locations included as Figure A-33, Figure A-34, and Figure A-

35. The resulting TKED rate data maintains the same resolution as the velocity grid, resulting in a 99 by 99 grid of TKED rate information, representing the TKED rate at various points in the cross section. Similar to the velocity grid data, the center region of the data grid influenced by the paddle mixer shaft and the noisy edge areas are not included in this analysis. During flocculation, the mixing speed was constant and significant temporal variations in the spatially averaged TKED rate are not observed, as shown in Figure 18 and in Figure D-53. The spatially averaged TKED results for the CC and EC experiments are similar, but together, they are slightly higher than the spatially averaged TKED rate of 0.169 cm^2 sec^{-3} for the artificially seeded experiment (Table 4).

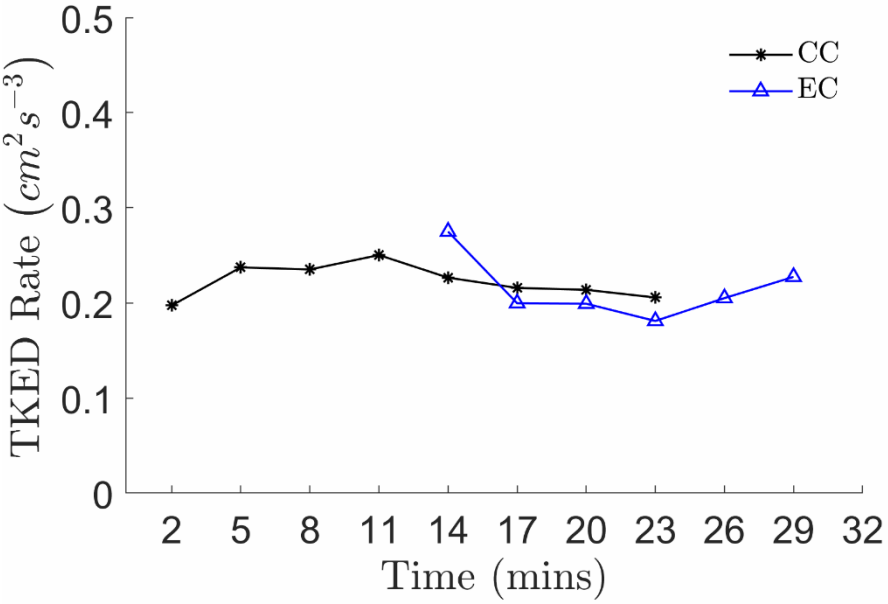

Figure 18: Mean TKED rate over time for CC and EC for DS#1.b.

Representative local TKED rates for the CC, EC, and artificially seeded experiments were obtained by averaging the spatially distributed TKED rate over time, incorporating the data from each turbulent flow data sets to produce a representative spatially-distributed TKED rate and are provided in Figure 19, Figure 20, and Figure 21 for the CC, EC, and artificially seeded experiments, respectively. Similar to the I_{2D}, the TKED rate is greater at the bottom of the cross

section, which is closest to the paddle mixer and increases radially outward from the mixing shaft, with the greatest dissipation rates near the edges of the cross section. The TKED rate is asymmetric in the horizontal direction, skewing to higher TKED rates in the direction of the mean velocity. The average TKED rate for CC, EC, and artificially seeded experiments are 0.223 cm^2 sec^{-3}, 0.214 cm^2 sec^{-3}, and 0.169 cm^2 sec^{-3} as shown in Table 4. The duplicate test showed similar trends and results are included in Figure C-48 and Figure C-49.

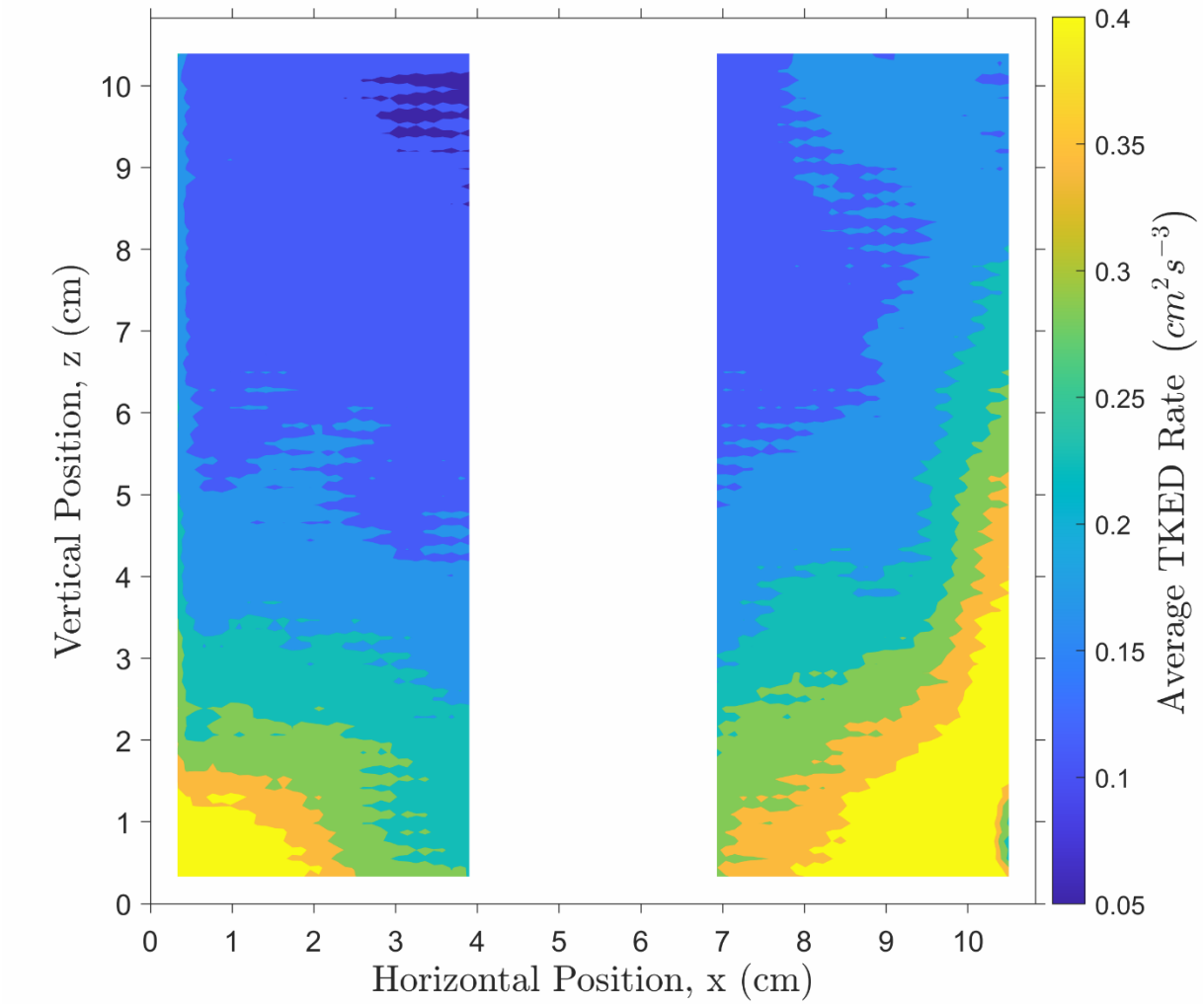

Figure 19: Average local TKED rate for the CC experiment of DS#1.b.

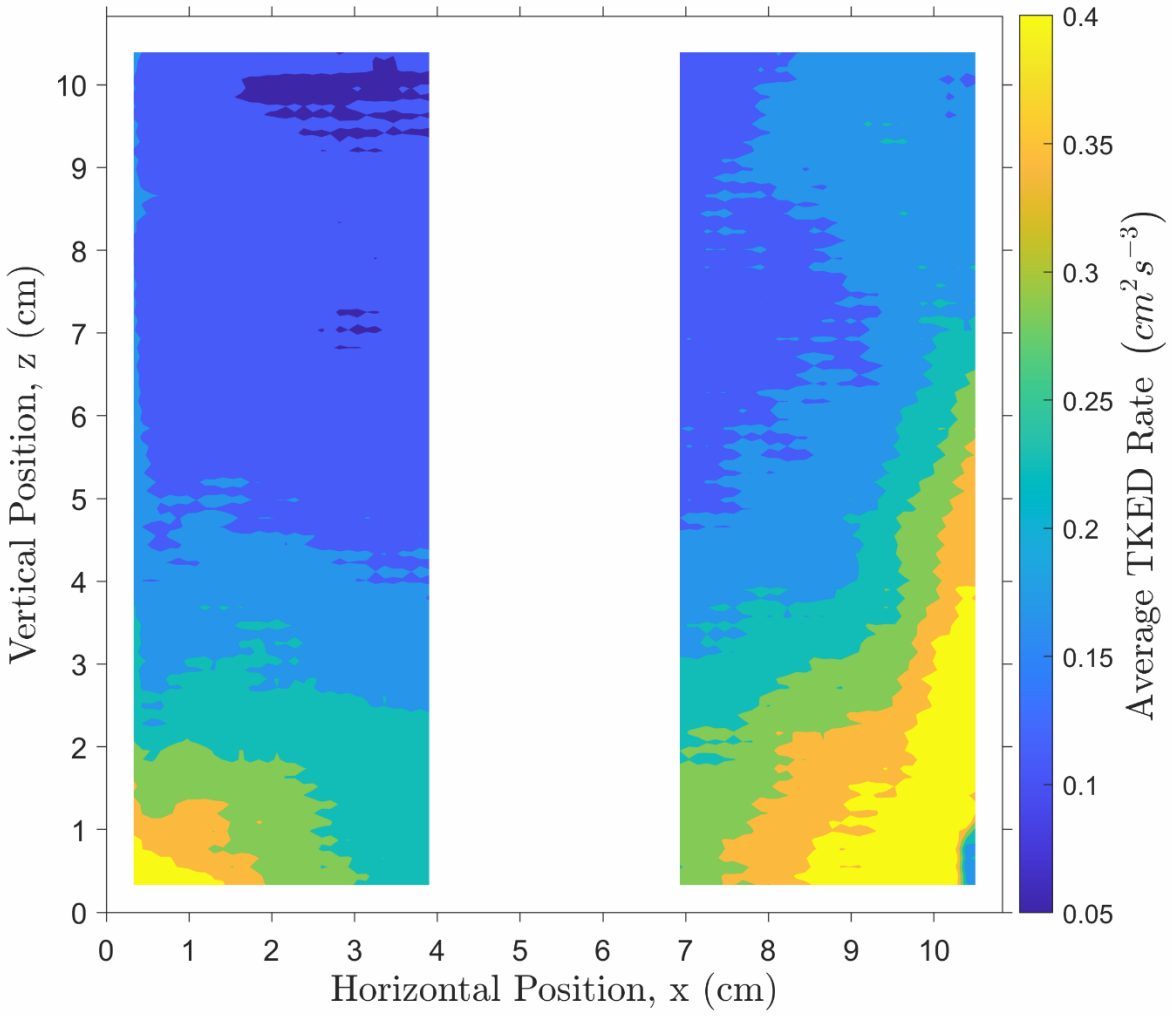

Figure 20: Average local TKED rate for the EC experiment of DS#1.b.

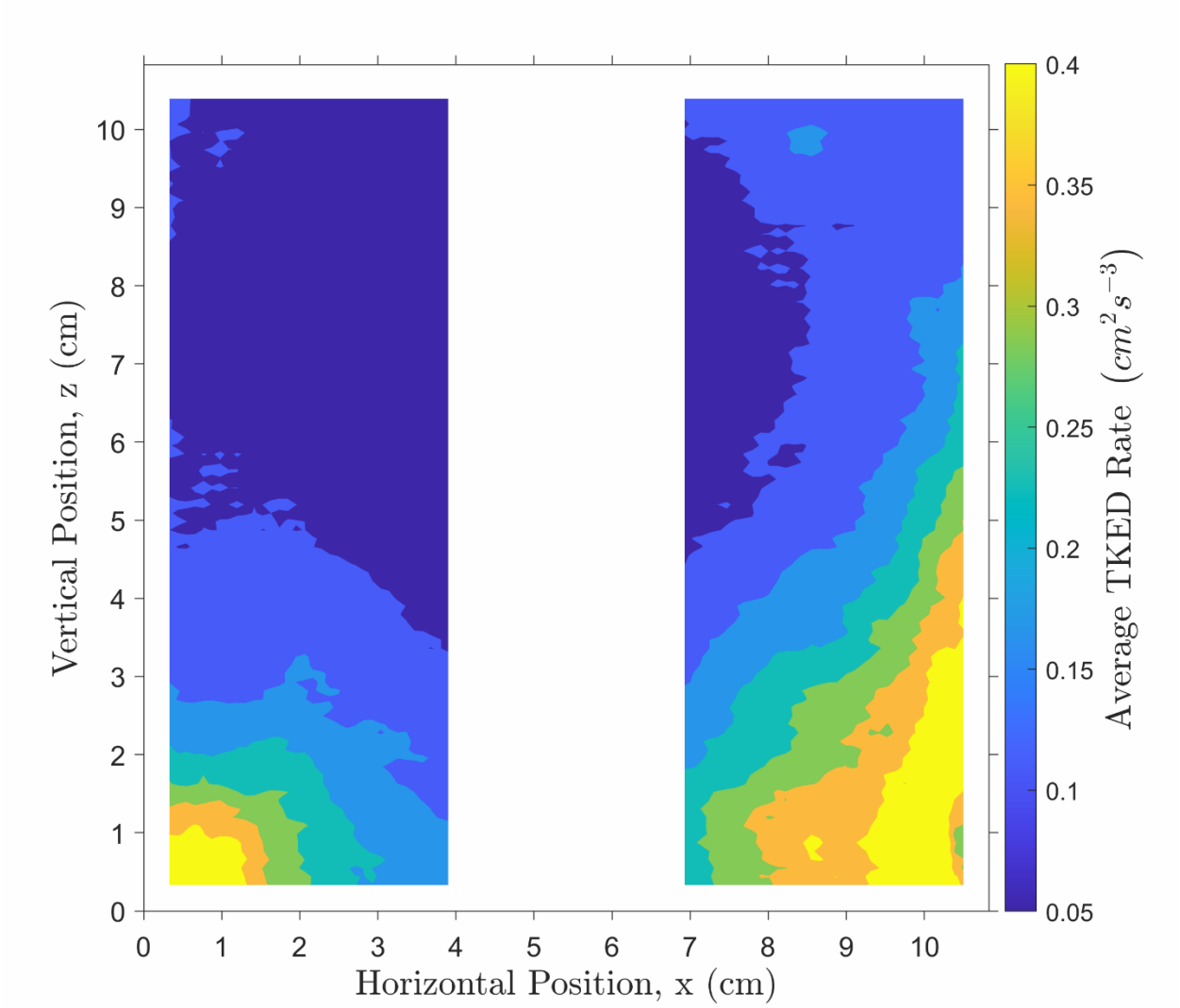

Figure 21: Average local TKED rate for artificially seeded experiment for DS#1.b

The local TKED rates for the two floc-seeded experiments (CC and EC) for both duplicate tests (DS#1.b and DS#2) were compared with each other, as shown in Figure A-36 and Figure C-50 and across the duplicate tests (e.g., DS#1.b vs DS#2), as shown in Figure D-56 and Figure D-57. Again, as each of the individual experiments were performed at the same mixing speed, the local TKED rates were expected to be similar across all experiments. Comparisons within each of the duplicate test data sets indicate a similar result for the TKED rates derived using CC and EC flocs, as marked by a mean ratio close to one and a small standard deviation in Table 3. When the

two duplicate tests were compared, DS#1.b yielded higher TKED rates than DS#2 as shown by a mean ratio greater than 1 and a large standard deviation, as shown in Table 3.

Table 3: TKED rate data comparison between CC, EC, Seeded, DS#1.b and DS#2

Data Source	**DS#1.b**	**DS#2**	**CC**	**EC**
Comparison	**CC:EC**	**CC:EC**	**DS#1.b:DS#2**	**DS#1.b:DS#2**
Mean Ratio	1.00	0.85	1.55	1.34
Standard Deviation	0.10	0.14	0.35	0.38

Additionally, the relative difference was evaluated between the TKED rate derived from the floc-seeded experiments and the artificially seeded experiment for DS#1.b, which acts as the control and is assumed as the more accurate experiment. Results from the relative comparison of the TKED rate between indicate the CC and EC floc-seeded experiments had an average percent relative difference in TKED rate compared to the artificially-seeded experiment of approximately 45% and 40% respectively. Absolute relative difference values are provided visually in Figure A-37 and Figure A-38, which display a variability between the local TKED rates derived from flocs vs. artificial beads as tracking particles.

3.2.4. Kolmogorov Length and Time Scales

Based on the mean TKED rates and the associated range for the flow fields measured with the CC and EC flocs, the Kolmogorov length (η) and time (τ) scales are presented in Table 4. Given the spatial resolution is approximately 1.1 mm, the velocity resolution is approximately two times the average Kolmogorov length scale, indicating the smallest scales of turbulent motion will not be fully captured; however, the velocity resolution is within a few multiples of η and thus will likely provide useful results. Based on the Nyquist criteria, the sampling frequency of 100 images

per second is many multiples more than the inverse of the Kolmogorov time scale, indicating the image capture rate is sufficient.

Table 4: Summary of the average TKED rate and the Kolmogorov length and time scales for CC, EC, and seeded water experiments and based on the G-Curve produced by Cornwell and Bishop [57] for DS#1.b.

Parameter		**CC Flocs**	**EC Flocs**	**Seeded Water**	**G-Curve**
$\bar{\varepsilon}$ (ε_{range})	($cm^2\ sec^{-3}$)	0.223 ± 0.018 (0.088-0.657)	0.214 ± 0.033 (0.090-0.614)	0.169 ± 0.016 (0.061-0.530)	0.729*
$\bar{\eta}$ (η_{range})	(mm)	0.507 (0.387-0.639)	0.516 (0.394-0.636)	0.543 (0.408-0.700)	0.377
$\bar{\tau}$ (τ_{range})	(sec)	0.226 (0.132-0.359)	0.230 (0.136-0.356)	0.259 (0.147-0.430)	0.125

*$\bar{\varepsilon}$ determined using Equation 16 and the value of G from the G-calibration curve.

3.3. Global Velocity Gradient Evaluation

As discussed in Section 2, the global velocity gradient, G, is evaluated by different methods depending on the available data. In this section, G is evaluated through the spatially-averaged TKED rate ($\bar{\varepsilon}$), and through an established G-calibration curve relating mixing speed to G for a square 2-liter jar test reactor equipped with a Phipps and Bird paddle mixer [57]. Additionally, this section provides a comparison between the local and global velocity gradients to identify regions where G accurately characterizes local velocity gradients.

3.3.1. Global Velocity Gradient Estimations

Based on the turbulent flow analyses for the flow fields evaluated using CC and EC flocs, $\bar{\varepsilon}$ is approximately 0.219 $cm^2\ sec^{-3}$ for all turbulent data sets, corresponding to an average G of 4.38 sec^{-1} per Equation 16 and as shown in Table 5. In comparison, the $\bar{\varepsilon}$ determined using an artificially seeded water is approximately 0.169 $cm^2\ sec^{-3}$, corresponding to an average G of 3.85

sec^{-1}. Per the established G-curve, a mixing speed of 15 rpm and a water temperature of 15°C, G is determined as approximate 8 sec^{-1}. The three estimations of G are all within the same order of magnitude, and the G value determined from the G-curve is the highest estimation.

Table 5: Spatially-averaged TKED rate ($\bar{\varepsilon}$) and the global velocity gradient (G), for flow field measurements using flocs, seeded water, and the G-curve from DS#1.b.

	Floc Average	**Seeded Water**	**G-Curve**
$\bar{\varepsilon}$ ($cm^2\,sec^{-3}$)	0.219	0.169	0.729*
G (sec^{-1})	4.38	3.85	8

*$\bar{\varepsilon}$ determined using Equation 16 and the value of G from the G-calibration curve.

3.3.2. Local Velocity Gradients vs. G

While G is determined using the spatial average of the local TKED rate, the local velocity gradients are also evaluated herein to identify regions where G accurately characterizes the local velocity gradients. In Figure 22, Figure 23, and Figure 24 the average ratio of the local velocity gradient to G is displayed spatially across the reactor cross section for CC, EC, and seeded experiments, respectively. For all experiments, G underestimated the velocity gradients near the paddle mixer at the bottom of the cross section and overestimated the velocity gradients near the water surface at the top of the cross section. Additionally, similar to the trends observed in the TKED rate and the $I_{2D,}$ the ratio of the local velocity gradient to G is asymmetric in the horizontal direction, skewing to higher TKED rates in the direction of the mean velocity. Duplicate results (Figure C-51 and Figure C-52) showed similar trends but the asymmetry was not as pronounced.

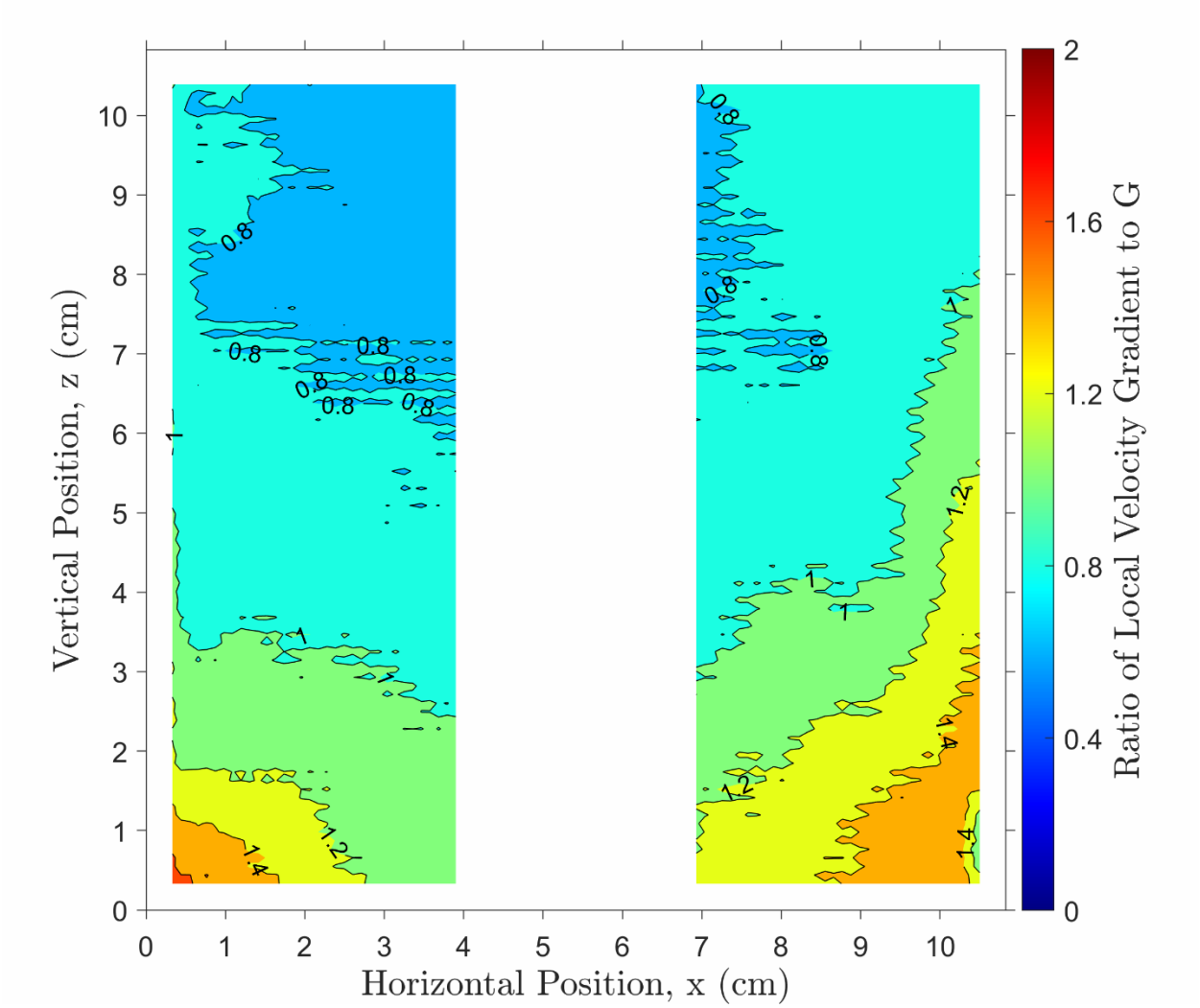

Figure 22: Contours of the average ratio of the local velocity gradients to the global velocity gradient, G, as determined by the spatially averaged TKED rate for the CC experiment of DS#1.b.

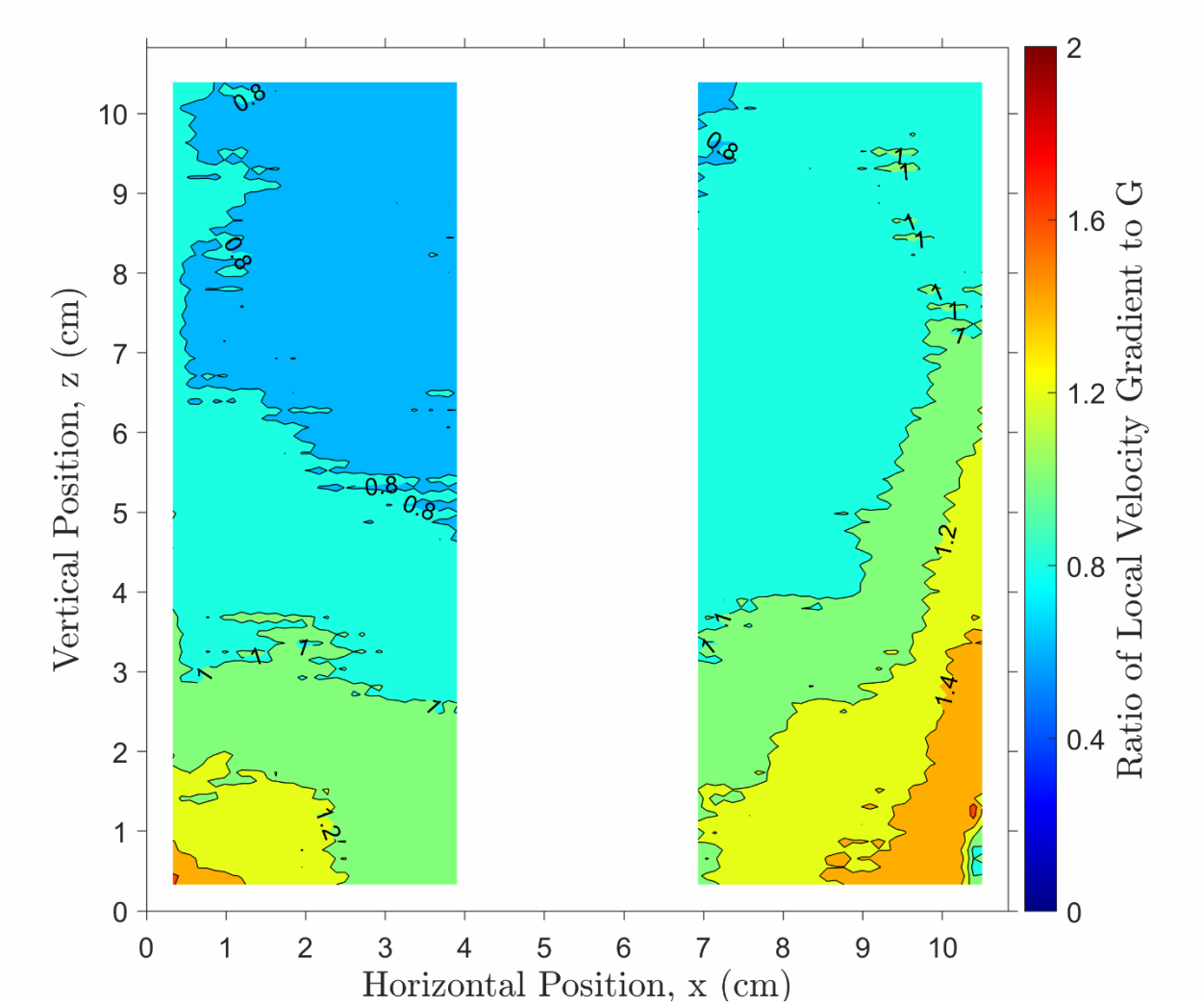

Figure 23: Contours of the average ratio of the local velocity gradients to the global velocity gradient, G, as determined by the spatially averaged TKED rate for the EC experiment of DS#1.b.

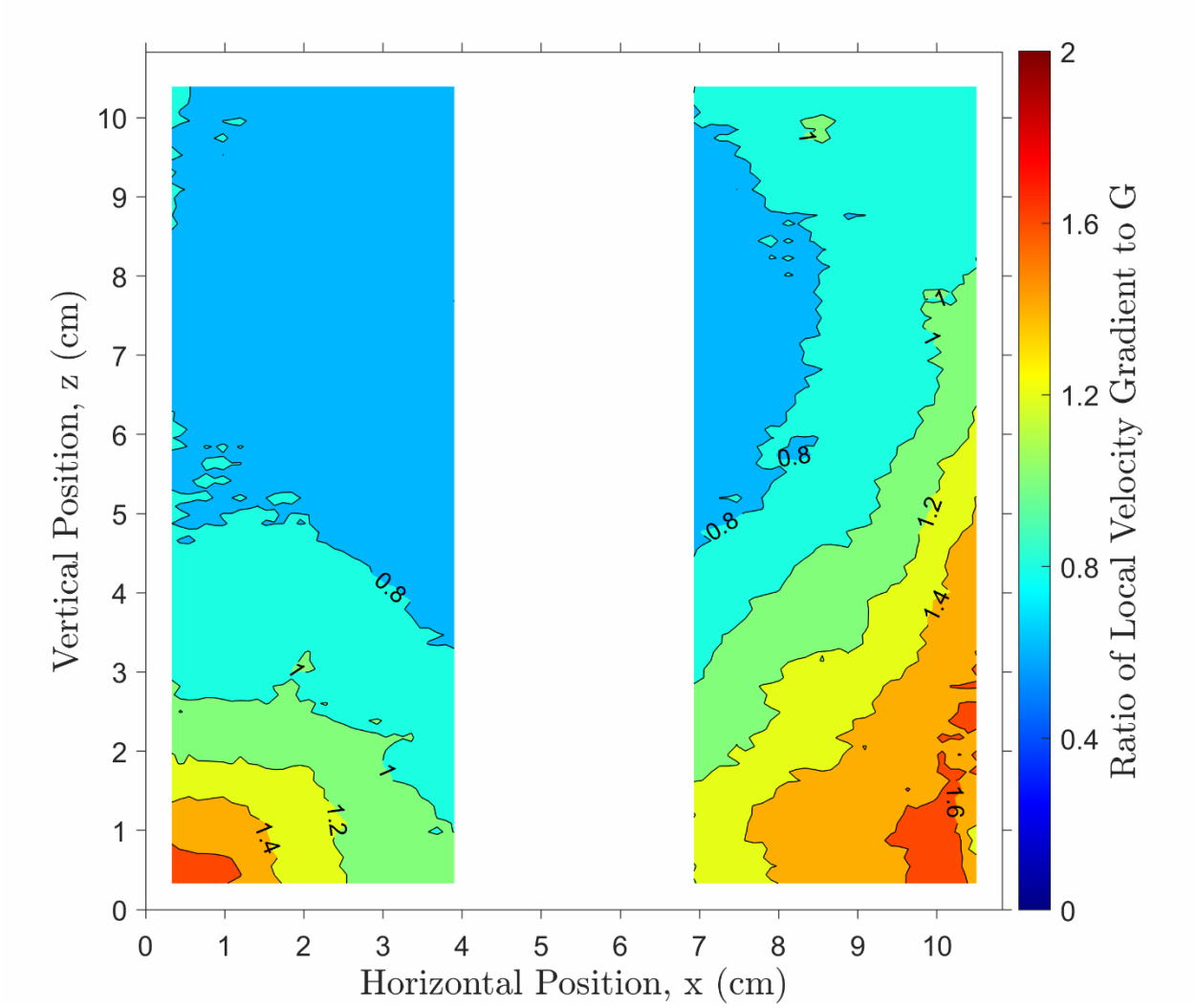

Figure 24: Contours of the average ratio of the local velocity gradients to the global velocity gradient, G, as determined by the spatially averaged TKED rate for the artificially seeded experiment of DS#1.b.

4. DISCUSSION

4.1. Flocculation Characterization

Temporal trends during flocculation for CC and EC experiments exhibited distinct differences including the rapidity with which smaller flocs agglomerated into larger flocs (Figure 7(c)(d)), the maximum floc size and floc number attained through flocculation (Figure 7(a)(b)) and in the trends of maximum floc size and fractal dimension (Figure 8 and Figure 11). These differences may be due to fundamental differences between CC and EC, including the speciation of the iron coagulant. Iron electrolysis first produces soluble Fe(II) that oxidizes to insoluble Fe(III), the kinetics of which depend on the dissolved oxygen concentration and pH. In contrast, $FeCl_3$ salts are added in the CC experiments directly resulting in Fe(III) in the solution. Although both CC and EC experimental systems were saturated with dissolved oxygen and buffered to maintain a pH of 8.3 resulting in rapid oxidation of Fe(II) to Fe(III) for the EC experiment, the initial difference in the coagulant form remains a fundamental difference between the CC and EC experiments.

While some of the temporal trend differences may be due to fundamental differences between CC and EC, the coagulant dosing timeline is also an important consideration. In CC, the coagulant is introduced into the system in a discrete method, with all the chemical added at one time, similar to full-scale water treatment plants. In contrast, for EC, the coagulant is generated within the system over the electrocoagulation duration. In this investigation, the coagulant addition began at the same time for both CC and EC. Given that EC required approximately 138 seconds to reach the target concentration, the target concentration was present during the CC experiment for approximately 138 seconds before the target concentration was present in the EC experiment. Therefore, while conditions for CC flocculation were present immediately upon coagulant addition, the EC experiment reached flocculation conditions only at the end of the

electrocoagulation process. Once each experiment reached flocculation conditions, miniscule flocs form first, which are not detectable given the image resolution (67.6 μm per pixel). These miniscule flocs then flocculate and begin to grown in size, ultimately reaching detectable sizes. Since CC flocculation began earlier, flocs had a longer time to grow into detectable sizes before data collection began during the slow mixing flocculation phase. This difference is evident in the cumulative floc count for CC and EC in Figure 7(a)(b). The maximum cumulative count is observed at the first data collection instances (2 minutes) for the CC experiment, with no observable transition from a few detectable flocs to many detectable flocs as observed for the EC experiment. By the start of the slow mixing flocculation phase for CC, the flocs had likely grown to detectable sizes, whereas that transition likely occurred throughout the beginning of the slow mixing flocculation phase for EC.

The impact of the different timelines for flocculation conditions between CC and EC is compounded by the fact that the coagulants were added/generated during the rapid mixing phase of the experiment, which lasted approximately 2.6 minutes. During rapid mixing, the increased energy input into the system likely resulted in higher floc collision frequencies, which increased the initial floc growth rate. Given that the CC experiment had approximately 138 seconds more than the EC experiment at flocculation conditions during the rapid mixing phase, the initial CC floc growth rate is different than that of EC, resulting in different initial trends that persisted during the slow mixing flocculation phase. These differing trends are particularly evident in Figure 8 and Figure 11, which depict trends in mean floc size and floc fractal dimension. In these figures, initial EC mean floc size and fractal dimension differ from CC, but reach similar values towards the end of data collection. Since the initial growth phase is different and initiates different trends for floc growth during flocculation, results cannot be simply shifted by 138 seconds to correct for the extra

flocculation time and enable a temporal comparison of the floc growth profiles. Instead, for comparative characterizations of flocculation between CC and EC, coagulant addition for CC should be added over a similar time span as the EC generation to ensure similar initial precipitation and flocculation conditions.

While comparative conclusions between CC and EC flocs are limited by the different initial conditions, the trends observed for each coagulant dosing method allow for individual observations. The oscillations observed in both the floc size distributions and the top 10% mean floc size for CC suggest floc breakage and regrowth, reaching a pseudo steady-state at approximately 15 minutes. The top 10% mean floc size for CC was larger than EC during the flocculation time measured, consistent with work produced by Lee and Gagnon [18]; however, a clear steady-state for EC flocs is not observed and thus EC may eventually produce flocs with a top 10% mean size equal to or greater than the CC experiment. While the absence of a steady state condition for EC is in contrast to the work of Lee and Gagnon [18], wherein both EC and CC experiments obtained steady state conditions by 10 minutes of flocculation at a pH of 8.3 at a mixing speed of 200 rpm, the flocculation mixing speed employed for this investigation was 15 rpm and thus results are not directly comparable. A steady state fractal dimension is attained earlier in the CC experiment, similar to results of Zhu et al., [35], who found that flocs exposed to a higher shear rate reached steady state earlier.

As an additional observation, the reversion back to a higher small floc frequency over time observed for the CC experiment is coupled with an increase in the large floc frequency, with flocs larger than 2,400 μm constituting approximately 3.2% at 37 minutes (Figure 7(c)). This increased large floc frequency and the decreased medium floc frequency is explained by the agglomeration of these medium sized flocs into larger flocs. The relatively high small (<400 μm) floc frequency

throughout flocculation for both EC and CC is similar to that of Kilander et al., [2], who used a similar flocculation characterization method. While small flocs may actually be present within the system, throughout flocculation, these small flocs are expected to agglomerate into larger flocs. Therefore, their continued presence in the floc size distribution throughout the experiment may possibly be due to the floc imaging and identification methodology used herein. This methodology is based on 2D floc images illuminated by a 2.3 mm light sheet, which results in limitations surrounding 3D characterizations of floc size and geometry, as discussed in Section 2. During the data collection, flocs may not be not completely within the laser light sheet, either because the floc size exceeds the light sheet thickness or because the floc is moving into or out of the light sheet. In these cases, the illuminated floc portion represents cross-sectional view of the floc within the light sheet and constitutes an area less than or equal to the largest cross section of the actual floc. Given the irregular floc shape, there is a higher probability that equivalent diameter for the actual floc is undersized because as the floc passes into and out of the light sheet, smaller cross sections are more frequently represented. The result is that the measured floc sizes tend to produce a greater frequency of small flocs, which may inaccurately characterize the actual floc size distribution. For this reason, changes in the frequency of medium and large floc sizes are more reliable as a means of describing changes in the floc size evolution.

4.2. Reactor Mixing Characterization

Reactor mixing characterization results agree qualitatively with results from past mixing analyses, with higher dissipation rates occurring near the paddle mixer, where the shear rate is stronger [27, 71]. Additionally, similar to results found by Cheng et al., [27], the TKED rate is higher near the edges of the cross section, likely due to interaction between the turbulent flow and the wall. Based on the estimated TKED rate for both CC and EC experiments, the velocity spatial

resolution is within a few multiples of the Kolmogorov length scale, and thus the velocity information is sufficiently resolved to inform turbulent flow analyses.

The use of flocs as tracking particles yielded higher TKED rates than that of the artificially seeded analysis, particularly in regions far from the mixing impeller when comparing valid turbulent data sets (Figure A-37 and Figure A-38). Visually, the flocs appear to faithfully follow the fluid motion without impacting the motion itself; however, a quantitative evaluation of the presence of floc on fluid motion is not within the scope of this investigation and is not apparent based on the data collected herein. Given the physical characteristics of flocs (e.g., high porosity, low density), flocs are not expected to impact the flow motion and the resulting discrepancy in the TKED results are more likely due to application of the PIV methodology using flocs as tracking particles. The region far from the impeller is marked by smaller velocity gradients and smaller particle displacements. Therefore, reactor mixing characterization in this region may be more impacted by the total error in the PIV methodology. Further, even in the most optimal data collection instances, floc number density was significantly less than that of the artificially seeded water, likely resulting in poorer correlations in the PIV analysis than for a traditional artificially seeded PIV analysis. The compound effect of both the smaller displacement away from the impeller region and the lower tracking particle density than that of the artificially seeded water, likely results in this discrepancy between the floc seeded and artificially seeded reactor mixing characterization.

Due to high vector rejection rates and/or poor adherence to the Kolmogorov -5/3 spectrum, several data collection instances using CC and EC flocs as tracking particles were unsuitable for turbulent flow mixing analyses. Since the same mixing rate was applied through the entire flocculation period in this investigation, a characteristic reactor mixing profile was developed by

selecting the most optimal data sets. However, for investigations where a variable mixing rate is applied and several characteristic reactor mixing profiles are needed throughout flocculation, floc size and number should be carefully evaluated to determine if the flocculation conditions are suitable to inform the PIV analysis. Otherwise, a traditional PIV analysis using artificially seeded water may be required.

A notable asymmetry was observed throughout the turbulent analyses, with higher I_{2D}, TKED rates, and local velocity gradients observed in the direction of the mean flow. One possibility for this asymmetry is a slight offset of the paddle mixer. If the paddle mixer was located slightly off-center within the reactor, the turbulent flow properties would be expected to be asymmetric as the energy is introduced to the system unevenly. In future experiments, restricting the paddle mixer and shaft oscillation and ensuring the paddle mixer is located in the exact center of the reactor will be crucial to eliminate the uneven energy distribution in the system and the resulting impacts on turbulent flow analyses. The fact that the asymmetry was significantly less in the duplicate experiment, may be due to repositioning of the paddle mixer shaft between experiments.

4.3. Global Velocity Gradient Evaluation

The global velocity gradient informed by the spatially averaged TKED rate calculated from the flow fields from CC and EC flocs as well as that of the seeded water are of the same order of magnitude as the G determined from the G-curve. However, when the local velocity gradients were compared with G, G was found to deviate by more 40% from the actual local velocity gradients. Given the spatial dependency of certain flocculation outcomes, particularly in regions close to the impeller, G's use to characterize reactor mixing will not provide the depth of information required to understand and predict flocculation. While G is generally within the same order of magnitude as the local velocity gradients, similar to the results of Cheng et al., [27], differences in reactor

shape and size, the presences of baffles, and use of different mixing impellers can create even greater variations in the local velocity gradients that can impact flocculation efficiency. Thus, while G is useful as a general estimation of the degree of reactor mixing, its use should be limited and closer attention should be paid to local velocity gradients [23].

5. CONCLUSIONS

The combined use of image processing techniques and PIV analysis is a useful tool to non-intrusively evaluate the impact of different operating parameters (e.g., coagulant dosing method, mixing intensity) on the resulting flocculation performance (e.g., steady-state floc size distribution, mean floc size, floc fractal dimension). This methodology is fundamental for evaluating spatiotemporal differences in flocculation performance and relating these differences to the local reactor mixing conditions, both of which are useful inputs for modeling full-scale water treatment plant reactors. These relations are enabled by evaluating flocculation and reactor mixing through the same data set, which is made possible by using flocs generated *in-situ* as the tracking particles for the PIV analysis. Through this novel methodology, this investigation characterized flocculation and reactor mixing for two coagulant dosing methods (CC and EC) and resulting in the following general conclusions that are strictly applicable to our experimental conditions:

- Flocculation for the CC experiment reached a steady state at approximately 20 minutes into flocculation and reached a relatively high fractal dimension, indicating a more compact, spherical floc shape. Flocculation for the EC experiment did not reach steady state during the experiment, but flocculation changes were observably smaller at the end of the experiment. The EC experiment reached a higher total mean floc size and fractal dimension than CC at the end of flocculation.
- The turbulence intensity (I_{2D}) the turbulent kinetic energy dissipation rate (ε), and the global velocity gradient (G) were all higher in regions closest to the paddle mixer and increased radially outward from the mixing shaft.

- Global velocity gradient (G) estimations using the spatially averaged total kinetic energy dissipation rate ($\bar{\varepsilon}$) and the G-curve informed by the input power yield similar results of the same order of magnitude.
- The spatially-averaged global velocity gradient (G) mischaracterizes the local velocity gradient within the reactor and underestimates the actual velocity gradients by more than 40% near the paddle mixer.
- The use of flocs as seeding particles for the PIV analysis was more suitable during select stages of flocculation, where a sufficient number of smaller flocs were detectable by the PIV cross-correlation core. In early and later stages of flocculation, use of flocs as seeding particles for the PIV analysis was less reliable, likely due to an insufficient number of small detectable flocs.
- TKED rates determined using CC and EC flocs were similar to TKED rates determined using artificial beads for regions close to the mixing impeller. However, as the vertical distance from the mixing impeller increased, the TKED rates determined using CC and EC flocs was higher than that of the TKED rate determined using artificial beads, reaching almost double the value in some regions.

Based on this initial methodology implementation described herein, the combined usage of image analysis and PIV can be leveraged to explore impacts of a variety of operational parameters in terms of flocculation and reactor mixing characterization, provided experimental conditions are suitable. For example, a single impeller was used to provide mixing in an unbaffled square mixing reactor. Comparative studies of different impeller shapes, sizes, and speeds, of various baffle configurations, and of different reactor shapes and sizes can quantitively reveal how these different characteristics impact reactor mixing and in so doing, how they impact flocculation. Additionally,

further studies are necessary to evaluate the impact of coagulant addition timeline on flocculation characterization to determine if the dosing timeline differences between CC (discrete) EC (over time) impacts the ability for temporal comparisons of flocculation characterizations.

This methodology provides opportunity for modification based on the particular experimental conditions, which make this methodology useful to study a wide range of operational conditions. For different mixing speeds, the field of view (i.e., the cross-sectional area imaged in the study) can be adjusted to optimize floc clarity while providing sufficient PIV conditions. In slower mixing conditions, particle displacement is smaller and a large field of view is unnecessary to capture floc movement. In this scenario, the field of view could be decreased without hindering the PIV analysis, resulting in a higher pixel resolution (i.e., a smaller area per pixel) and a more detailed flocculation characterization since smaller particles could be captured. Additionally, the laser slight sheet thickness and camera aperture can be adjusted to optimize the illuminated region of the focal plane based on the anticipated maximum floc size, reducing floc size bias associated with flocs traveling into and out of the laser light sheet and focal plane. Finally, measurement conditions can be tailored to the specific flocculation period in question, to obtain the most useful results. Future investigations should carefully consider the target flocculation and reactor mixing characteristics and tailor the methodology described herein to the specific experimental conditions, taking into account the impact of image resolution and light sheet thickness on flocculation characterization and the impact of floc density and movement on reactor mixing characterizations using PIV.

REFERENCES

1. Gregory, J. and O'Melia, C.R., *Fundamentals of flocculation.* Critical Reviews in Environmental Control, 1989. **19**(3): p. 185-230.
2. Kilander, J., Blomström, S., and Rasmuson, A., *Scale-up behaviour in stirred square flocculation tanks.* Chemical Engineering Science, 2007. **62**(6): p. 1606-1618.
3. Nadella, M., Sharma, R., and Chellam, S., *Fit-for-purpose treatment of produced water with iron and polymeric coagulant for reuse in hydraulic fracturing: Temperature effects on aggregation and high-rate sedimentation.* Water Research, 2020. **170**: p. 115330.
4. Benjamin, M.M. and Lawler, D.F., *Water Quality Engineering: Physical/Chemical Treatment Processes*. 2013: Wiley. 912.
5. Shen, X. and Maa, J.P.Y., *A camera and image processing system for floc size distributions of suspended particles.* Marine Geology, 2016. **376**: p. 132-146.
6. Chakraborti, R.K., Atkinson, J.F., and Van Benschoten, J.E., *Characterization of Alum Floc by Image Analysis.* Environmental Science & Technology, 2000. **34**(18): p. 3969-3976.
7. Jarvis, P., Jefferson, B., Gregory, J., and Parsons, S.A., *A review of floc strength and breakage.* Water Research, 2005. **39**(14): p. 3121-37.
8. Tambo, N., *Physical characteristics of flocs—II. Strength of floc.* Water Research, 1979. **13**(5): p. 421-427.
9. Hopkins, D.C. and Ducoste, J.J., *Characterizing flocculation under heterogeneous turbulence.* Journal of Colloid and Interface Science, 2003. **264**(1): p. 184-94.

10. Spicer, P.T. and Pratsinis, S.E., *Shear-induced flocculation: The evolution of floc structure and the shape of the size distribution at steady state.* Water Research, 1996. **30**(5): p. 1049-1056.

11. Bouyer, D., Coufort, C., Line, A., and Do-Quang, Z., *Experimental analysis of floc size distributions in a 1-L jar under different hydrodynamics and physicochemical conditions.* Journal of Colloid and Interface Science, 2005. **292**(2): p. 413-28.

12. Liu, Y., Zhang, X., Jiang, W., Wu, M., and Li, Z., *Comprehensive review of floc growth and structure using electrocoagulation: Characterization, measurement, and influencing factors.* Chemical Engineering Journal, 2021. **417**.

13. Harif, T. and Adin, A., *Characteristics of aggregates formed by electroflocculation of a colloidal suspension.* Water Research, 2007. **41**(13): p. 2951-61.

14. Lee, S.Y. and Gagnon, G.A., *Growth and structure of flocs following electrocoagulation.* Separation and Purification Technology, 2016. **163**: p. 162-168.

15. Kim, K., Narayanan, J., Sen, A., and Chellam, S., *Virus Removal and Inactivation Mechanisms during Iron Electrocoagulation: Capsid and Genome Damages and Electro-Fenton Reactions.* Environmental Science & Technology, 2021. **55**(19): p. 13198-13208.

16. Nasrullah, M., Singh, L., Krishnan, S., Sakinah, M., Mahapatra, D.M., and Zularisam, A.W., *Electrocoagulation treatment of raw palm oil mill effluent: Effect of operating parameters on floc growth and structure.* Journal of Water Process Engineering, 2020. **33**.

17. Bagga, A., Chellam, S., and Clifford, D.A., *Evaluation of iron chemical coagulation and electrocoagulation pretreatment for surface water microfiltration.* Journal of Membrane Science, 2008. **309**(1-2): p. 82-93.

18. Lee, S.Y. and Gagnon, G.A., *Comparing the growth and structure of flocs from electrocoagulation and chemical coagulation.* Journal of Water Process Engineering, 2016. **10**: p. 20-29.

19. Garcia-Segura, S., Eiband, M.M.S.G., de Melo, J.V., and Martínez-Huitle, C.A., *Electrocoagulation and advanced electrocoagulation processes: A general review about the fundamentals, emerging applications and its association with other technologies.* Journal of Electroanalytical Chemistry, 2017. **801**: p. 267-299.

20. Harif, T., Khai, M., and Adin, A., *Electrocoagulation versus chemical coagulation: coagulation/flocculation mechanisms and resulting floc characteristics.* Water Res, 2012. **46**(10): p. 3177-88.

21. Vadasarukkai, Y.S. and Gagnon, G.A., *Influence of the Mixing Energy Consumption Affecting Coagulation and Floc Aggregation.* Environmental Science & Technology, 2017. **51**(6): p. 3480-3489.

22. Camp, T.R. and Stein, P.C., *Velocity gradient and internal work in fluid motion.* Journal of Boston Society of Civil Engineers, 1943. **30**(4): p. 28.

23. Clark, M.M., *Critique of Camp and Stein's RMS Velocity Gradient.* Journal of Environmental Engineering, 1985. **111**(6): p. 741-754.

24. Han, M. and Lawler, D., *The (Relative) Insignificance of G in Flocculation.* American Water Works Association, 1992. **84**(10): p. 13.

25. Ducoste, J.J. and Clark, M.M., *The Influence of Tank Size and Impeller Geometry on Turbulent Flocculation: I. Experimental.* Environmental Engineering Science, 1998. **15**(3): p. 215-224.

26. He, W., Xue, L., Gorczyca, B., Nan, J., and Shi, Z., *Experimental and CFD studies of floc growth dependence on baffle width in square stirred-tank reactors for flocculation.* Separation and Purification Technology, 2018. **190**: p. 228-242.

27. Cheng, C., Atkinson, J.F., and Bursik, M.I., *Direct Measurement of Turbulence Structures in Mixing Jar Using PIV*. Journal of Environmental Engineering, 1997. **123**(2): p. 115-125.

28. Bouyer, D., Escudié, R., and Liné, A., *Experimental Analysis of Hydrodynamics in a Jar-test.* Process Safety and Environmental Protection, 2005. **83**(1): p. 22-30.

29. Kilander, J., Blomström, S., and Rasmuson, A., *Spatial and temporal evolution of floc size distribution in a stirred square tank investigated using PIV and image analysis.* Chemical Engineering Science, 2006. **61**(23): p. 7651-7667.

30. Spicer, P.T., Pratsinis, S.E., Raper, J., Amal, R., Bushell, G., and Meesters, G., *Effect of shear schedule on particle size, density, and structure during flocculation in stirred tanks.* Powder Technology, 1998. **97**(1): p. 26-34.

31. Saarenrinne, P. and Piirto, M., *Turbulent kinetic energy dissipation rate estimation from PIV velocity vector fields.* Experiments in Fluids, 2000. **29**(7): p. S300-S307.

32. Raffel, M.W., Christian E.; Scarano, Fulvio; Kähler, Christian J.; Wereley, Steve T.; Kompenhans, Jürgen, *Particle Image Velocimetry: A Practical Guide*. 3 ed. 2018: Springer.

33. Wiesner, M.R., *Kinetics of aggregate formation in rapid mix.* Water Research, 1992. **26**(3): p. 379-387.

34. Veerapaneni, S. and Wiesner, M.R., *Hydrodynamics of Fractal Aggregates with Radially Varying Permeability.* Journal of Colloid and Interface Science, 1996. **177**(1): p. 45-57.

35. Zhu, Z., Peng, D., and Dou, J., *Changes in the two-dimensional and perimeter-based fractal dimensions of kaolinite flocs during flocculation: a simple experimental study.* Water Science & Technology, 2018. **77**(3-4): p. 861-870.

36. Chellam, S. and Wiesner, M.R., *Fluid mechanics and fractal aggregates.* Water Research, 1993. **27**(9): p. 1493-1496.

37. Serra, T. and Casamitjana, X., *Structure of the Aggregates During the Process of Aggregation and Breakup Under a Shear Flow.* Journal of Colloid and Interface Science, 1998. **206**(2): p. 505-511.

38. Stone, M. and Krishnappan, B.G., *Floc morphology and size distributions of cohesive sediment in steady-state flow.* Water Research, 2003. **37**(11): p. 2739-47.

39. Logan, B.E. and Kilps, J.R., *Fractal dimensions of aggregates formed in different fluid mechanical environments.* Water Research, 1995. **29**(2): p. 443-453.

40. Li, X.-Y. and Logan, B.E., *Permeability of Fractal Aggregates.* Water Research, 2001. **35**(14): p. 3373-3380.

41. Li, X. and Logan, B.E., *Collision Frequencies between Fractal Aggregates and Small Particles in a Turbulently Sheared Fluid.* Environmental Science & Technology, 1997. **31**(4): p. 1237-1242.

42. Chakraborti, R.K., Gardner, K.H., Atkinson, J.F., and Van Benschoten, J.E., *Changes in fractal dimension during aggregation.* Water Research, 2003. **37**(4): p. 873-83.

43. Zhong, R., Zhang, X., Xiao, F., Li, X., and Cai, Z., *Effects of humic acid on physical and hydrodynamic properties of kaolin flocs by particle image velocimetry.* Water Research, 2011. **45**(13): p. 3981-90.

44. Pope, S.B., *Turbulent Flows*. 2000, Cambridge: Cambridge University Press. 802.

45. Wang, G., Yang, F., Wu, K., Ma, Y., Peng, C., Liu, T., and Wang, L.-P., *Estimation of the dissipation rate of turbulent kinetic energy: A review.* Chemical Engineering Science, 2021. **229**.

46. George, W.K. and Hussein, H.J., *Locally axisymmetric turbulence.* Journal of Fluid Mechanics, 1991. **233**: p. 1-23.

47. Kimmoun, O. and Branger, H., *A particle image velocimetry investigation on laboratory surf-zone breaking waves over a sloping beach.* Journal of Fluid Mechanics, 2007. **588**: p. 353-397.

48. Luznik, L., Gurka, R., Nimmo Smith, W.A.M., Zhu, W., Katz, J., and Osborn, T.R., *Distribution of Energy Spectra, Reynolds Stresses, Turbulence Production, and Dissipation in a Tidally Driven Bottom Boundary Layer.* Journal of Physical Oceanography, 2007. **37**(6): p. 1527-1550.

49. Doron, P., Bertuccioli, L., Katz, J., and Osborn, T.R., *Turbulence Characteristics and Dissipation Estimates in the Coastal Ocean Bottom Boundary Layer from PIV Data.* Journal of Physical Oceanography, 2001. **31**(8): p. 2108-2134.

50. Cowen, E.A., Mei Sou, I., Liu, P.L.F., and Raubenheimer, B., *Particle Image Velocimetry Measurements within a Laboratory-Generated Swash Zone.* Journal of Engineering Mechanics, 2003. **129**(10): p. 1119-1129.

51. Sharp, K.V. and Adrian, R.J., *PIV study of small-scale flow structure around a Rushton turbine.* American Institute of Chemical Engineers Journal, 2001. **47**(4): p. 13.

52. Šulc, R., Pešava, V., and Ditl, P., *Estimating the local turbulent energy dissipation rate using 2-D PIV measurements and a 1-D energy spectrum function.* Theoretical Foundations of Chemical Engineering, 2015. **49**(2): p. 145-156.

53. Xu, D. and Chen, J., *Accurate estimate of turbulent dissipation rate using PIV data.* Experimental Thermal and Fluid Science, 2013. **44**: p. 662-672.

54. Pedocchi, F. and Piedra-Cueva, I., *Camp and Stein's Velocity Gradient Formalization.* Journal of Environmental Engineering, 2005. **131**(10): p. 1369-1376.

55. Cleasby, J.L., *Is Velocity-Gradient a Valid Turbulent Flocculation Parameter.* Journal of Environmental Engineering, 1984. **110**(5): p. 875-897.

56. Park, H. and Park, N.S., *Analysis of local velocity gradients in rapid mixer using particle image velocimetry technique.* Water Supply, 2002. **2**(5-6): p. 47-55.

57. Cornwell, D. and Bishop, M., *Determining velocity gradients in laboratory and full-scale systems.* American Water Works Association, 1983. **75**(9): p. 6.

58. Bovik, A., *Handbook of Image and Video Processing*, ed. A. Bovik. 2005.

59. Young, I.T., Gerbrands, J.J., and Van Vliet, L.J., *Fundamentals of Image Processing*. 2.2 ed. 1998, The Netherlands: Delft University of Technology.

60. Smith, S.J. and Friedrichs, C.T., *Image processing methods for in situ estimation of cohesive sediment floc size, settling velocity, and density.* Limnology and Oceanography: Methods, 2015. **13**(5): p. 250-264.

61. Smith, S.J. and Friedrichs, C.T., *Size and settling velocities of cohesive flocs and suspended sediment aggregates in a trailing suction hopper dredge plume.* Continental Shelf Research, 2011. **31**(10): p. S50-S63.

62. Lintern, G. and Sills, G., *Techniques for Automated Measurement of Floc Properties.* Journal of Sedimentary Research, 2006. **76**(10): p. 1183-1195.

63. Mikkelsen, O.A., Hill, P.S., Milligan, T.G., and Chant, R.J., *In situ particle size distributions and volume concentrations from a LISST-100 laser particle sizer and a digital floc camera.* Continental Shelf Research, 2005. **25**(16): p. 1959-1978.

64. Scharnowski, S. and Kähler, C.J., *Particle image velocimetry - Classical operating rules from today's perspective.* Optics and Lasers in Engineering, 2020. **135**.

65. Thielicke, W. and Sonntag, R., *Particle Image Velocimetry for MATLAB: Accuracy and enhanced algorithms in PIVlab.* Journal of Open Research Software, 2021. **9**.

66. Mori, N. and Chang, K.-A., *Introduction to MPIV*. 2003, user reference manual. p. 14.

67. Lourenco, L. and Krothapalli, A., *On the accuracy of velocity and vorticity measurements with PIV.* Experiments in Fluids, 1995. **18**(6): p. 421-428.

68. Huang, H., Dabiri, D., and Gharib, M., *On errors of digitial particle image velocimetry.* Measurement Science and Technology, 1997. **8**: p. 14.

69. Zhao, L., Wang, B., Armenante, P.M., Conmy, R., and Boufadel, M.C., *Characterization of Turbulent Properties in the EPA Baffled Flask for Dispersion Effectiveness Testing.* Journal of Environmental Engineering, 2016. **142**(1).

70. Jarvis, P., Jefferson, B., and Parsons, S.A., *Measuring Floc Structural Characteristics.* Reviews in Environmental Science and Bio/Technology, 2005. **4**(1-2): p. 1-18.

71. Kilander, J. and Rasmuson, A., *Energy dissipation and macro instabilities in a stirred square tank investigated using an LE PIV approach and LDA measurements.* Chemical Engineering Science, 2005. **60**(24): p. 6844-6856.

APPENDIX A

Auxiliary information for experimental analysis and results for the results reported in the manuscript (DS#1.a and DS#1.b).

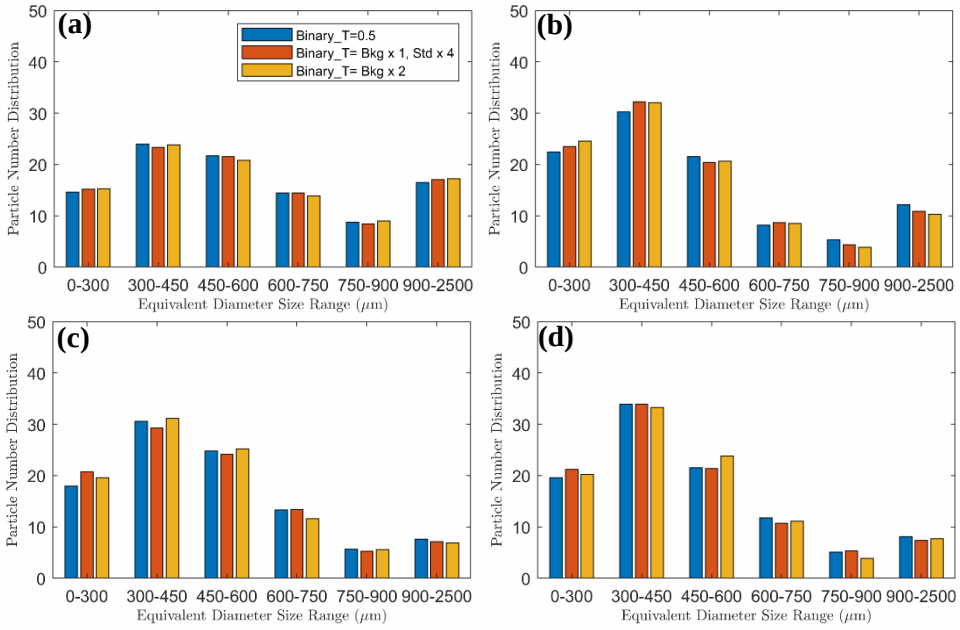

Figure A-25: Mean particle count based on different binary threshold methods at (a) 7 minutes; (b) 22 minutes; (c) 27 minutes; and (d) 36 minutes for CC, DS#1.a. ("Binary_T=0.5" represents a global threshold of 0.5. "Binary_T = Bkg x 1, Std. x 4" represents an adaptive threshold based on the background intensity plus four times the standard deviation. "Binary_T = Bkg x 2" represents an adaptive threshold based on two times the background intensity)

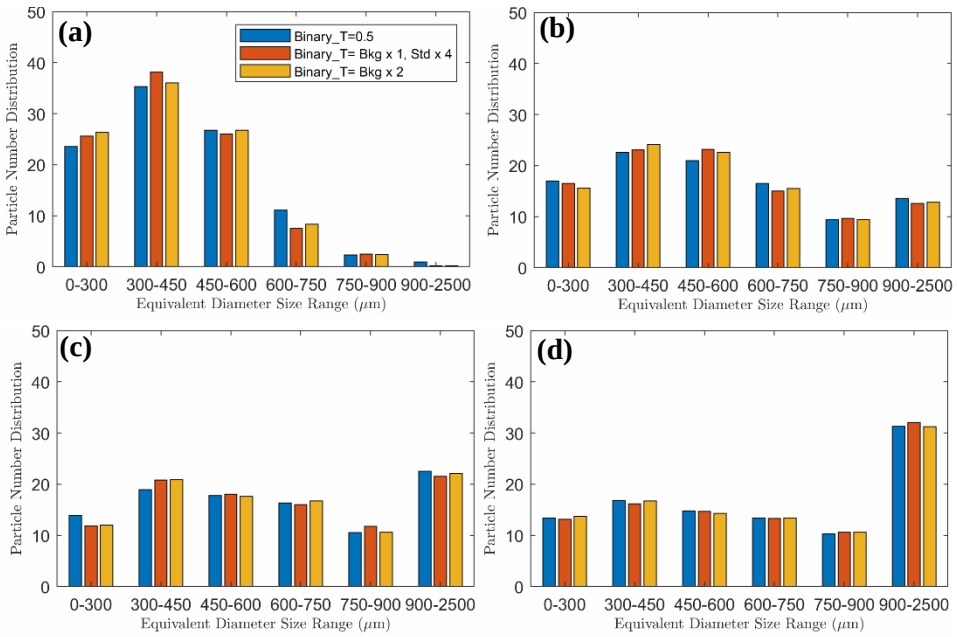

Figure A-26: Mean particle count based on different binary threshold methods at (a) 7 minutes; (b) 22 minutes; (c) 27 minutes; and (d) 36 minutes for EC, DS#1.a. ("Binary_T=0.5" represents a global threshold of 0.5. "Binary_T = Bkg x 1, Std. x 4" represents an adaptive threshold based on the background intensity plus four times the standard deviation. "Binary_T = Bkg x 2" represents an adaptive threshold based on two times the background intensity.)

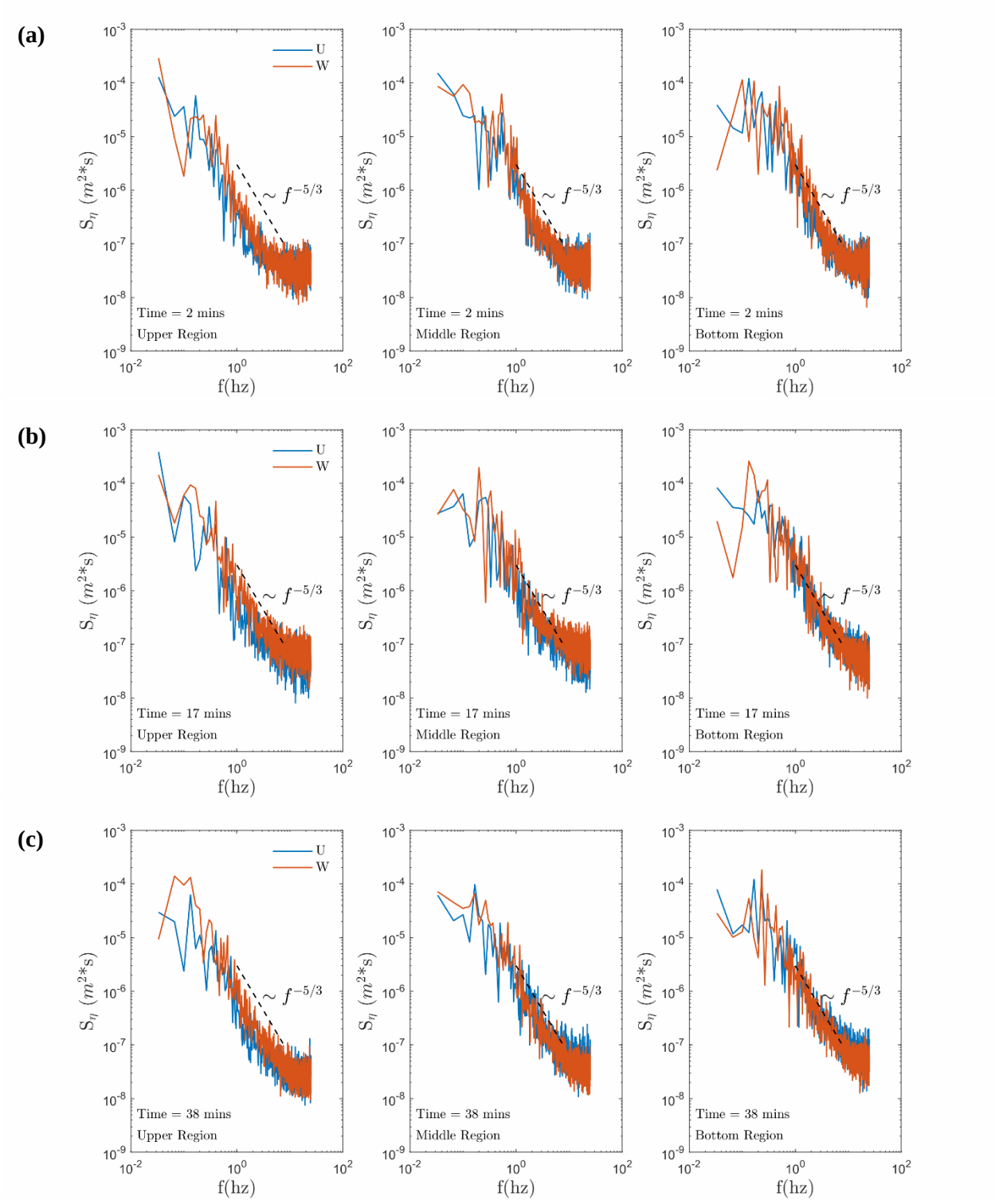

Figure A-27: Energy spectrum at the left upper, left middle, and left bottom region for horizontal (U) and vertical (W) velocity components for CC at (a) 2 minutes; (b) 17 minutes and (c) 38 minutes for DS#1.b

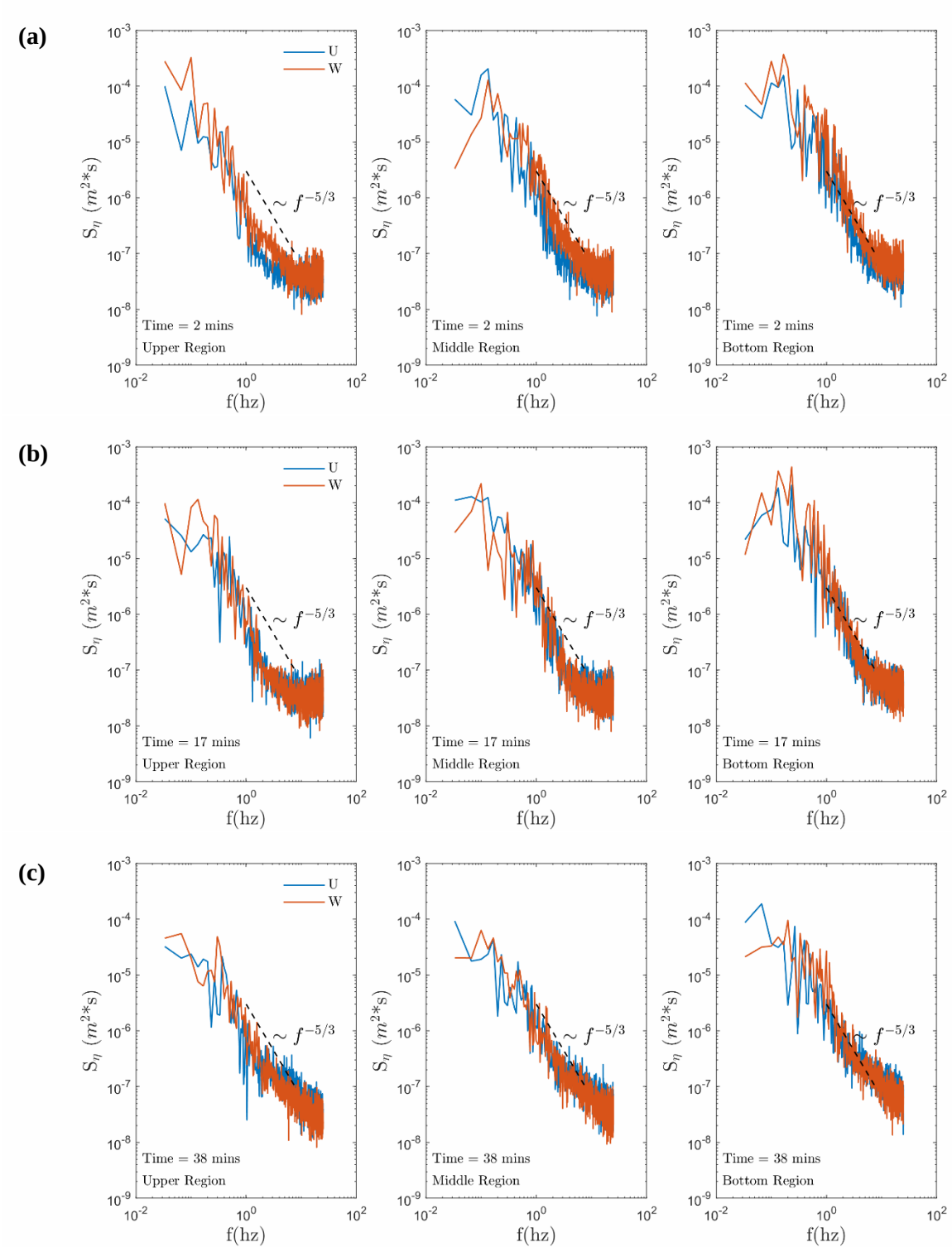

Figure A-28: Energy spectrum at the left upper, left middle, and left bottom region for horizontal (U) and vertical (W) velocity components for EC at (a) 2 minutes; (b) 17 minutes and (c) 38 minutes for DS#1.b

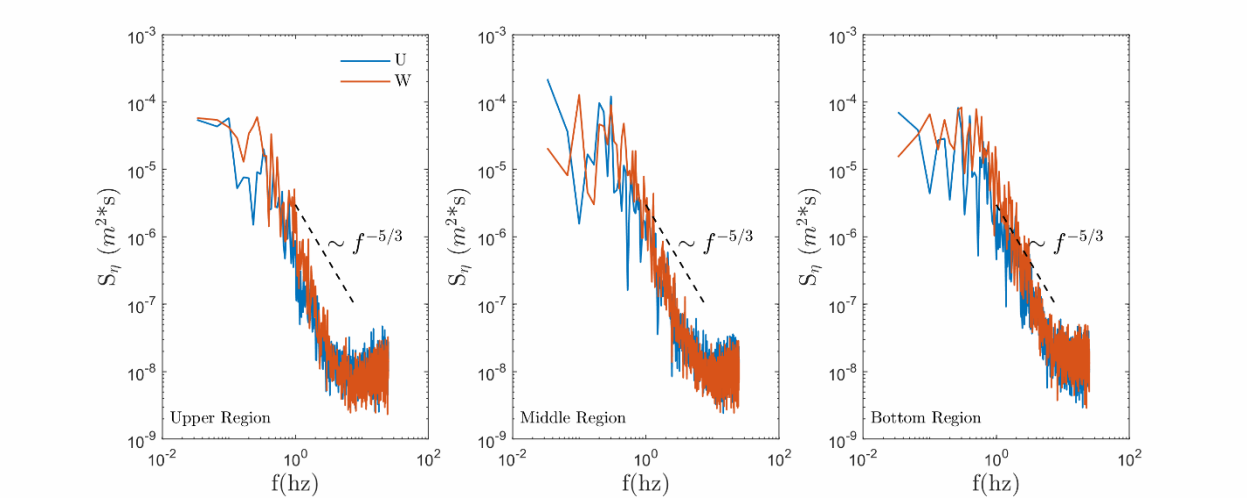

Figure A-29: Energy spectrum at the left upper, left middle, and left bottom region for horizontal (U) and vertical (W) velocity components for the artificially seeded system for DS#1.b. Note, the artificially seeded system was not impacted by flocculation time thus a single time instance is reported herein.

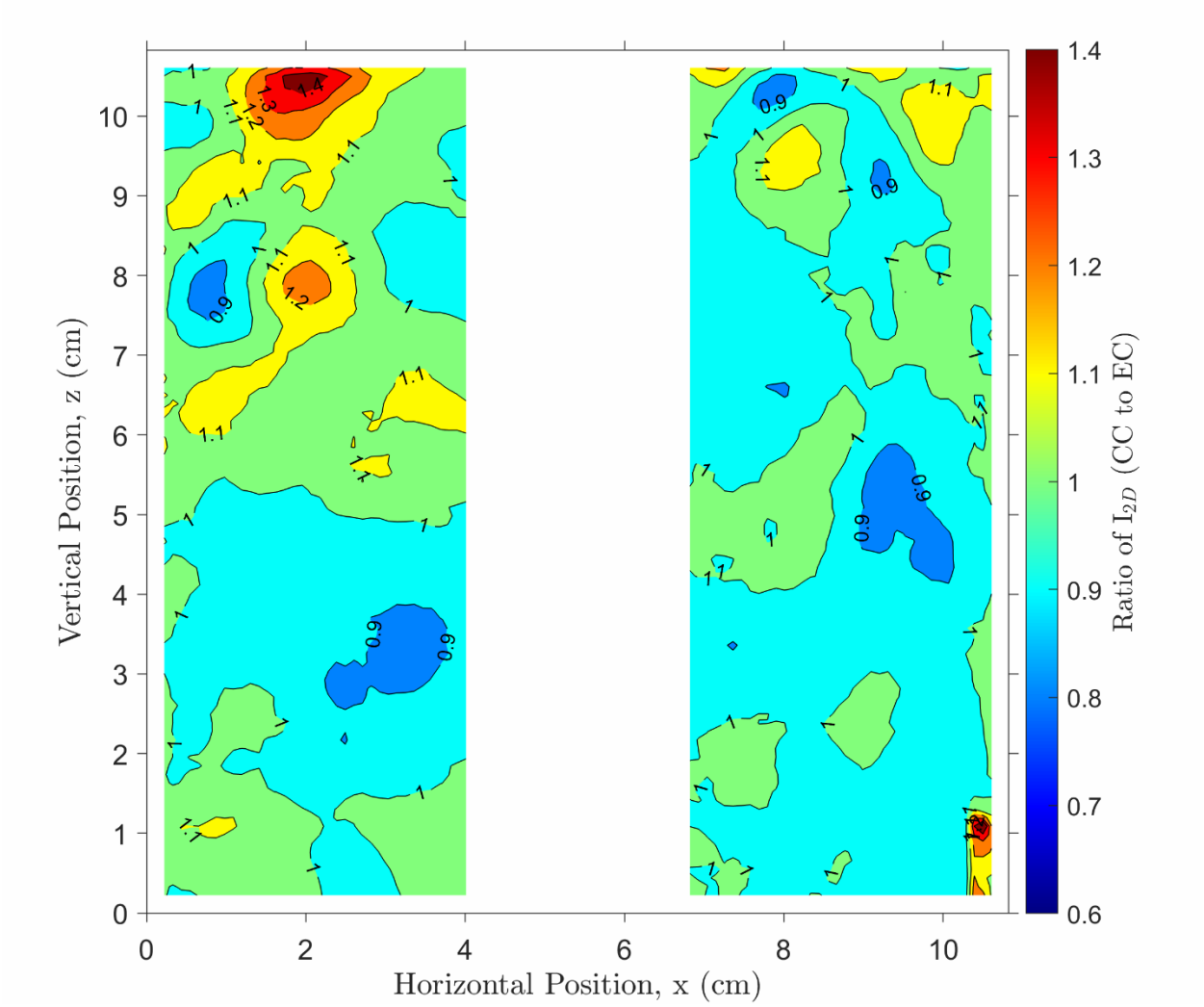

Figure A-30: Ratio of turbulence intensity values measured in the CC and EC experiments for DS#1.b.

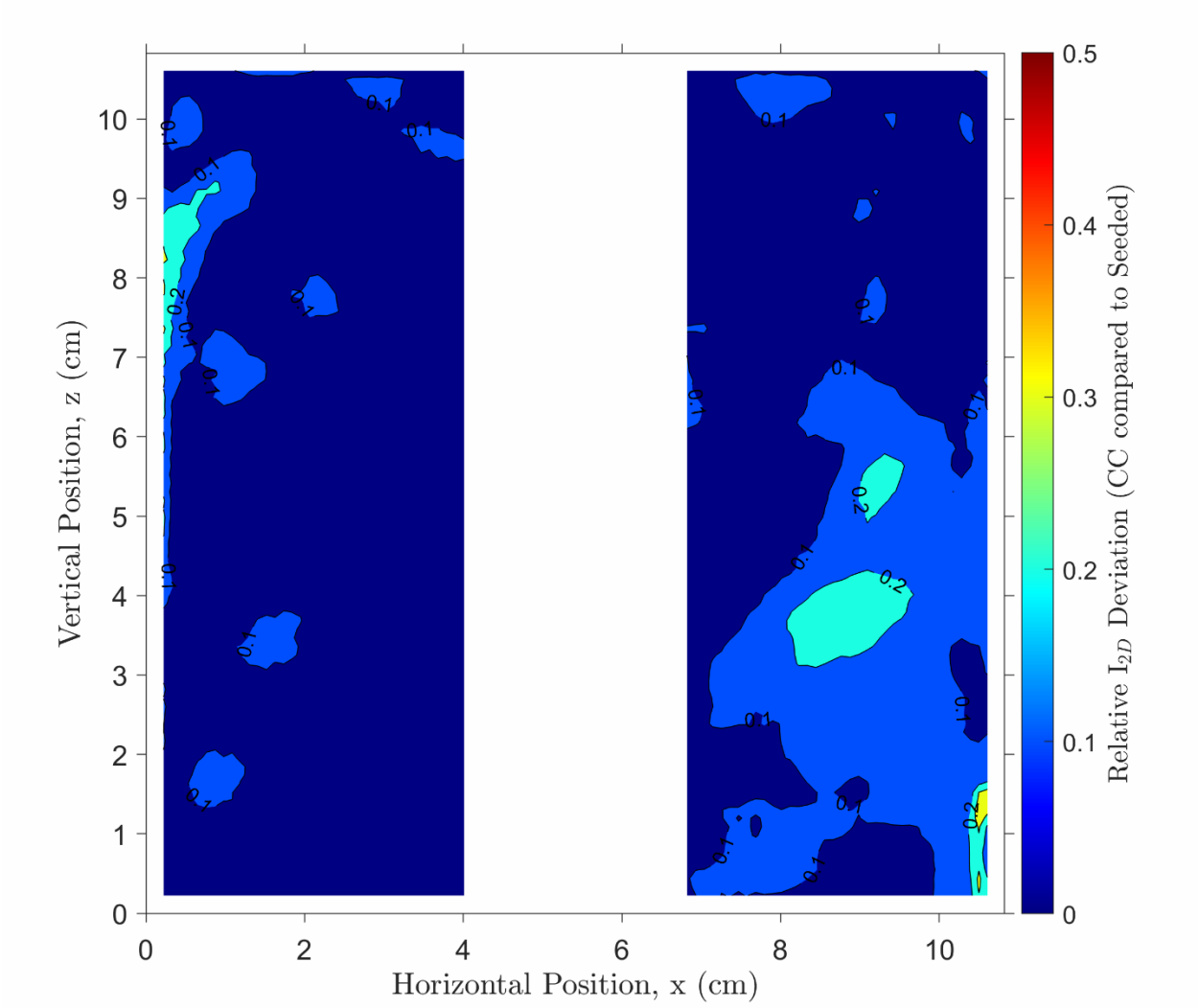

Figure A-31: Relative turbulence intensity deviation when comparing the turbulence intensity measurements between the CC and Seeded experiments for DS#1.b.

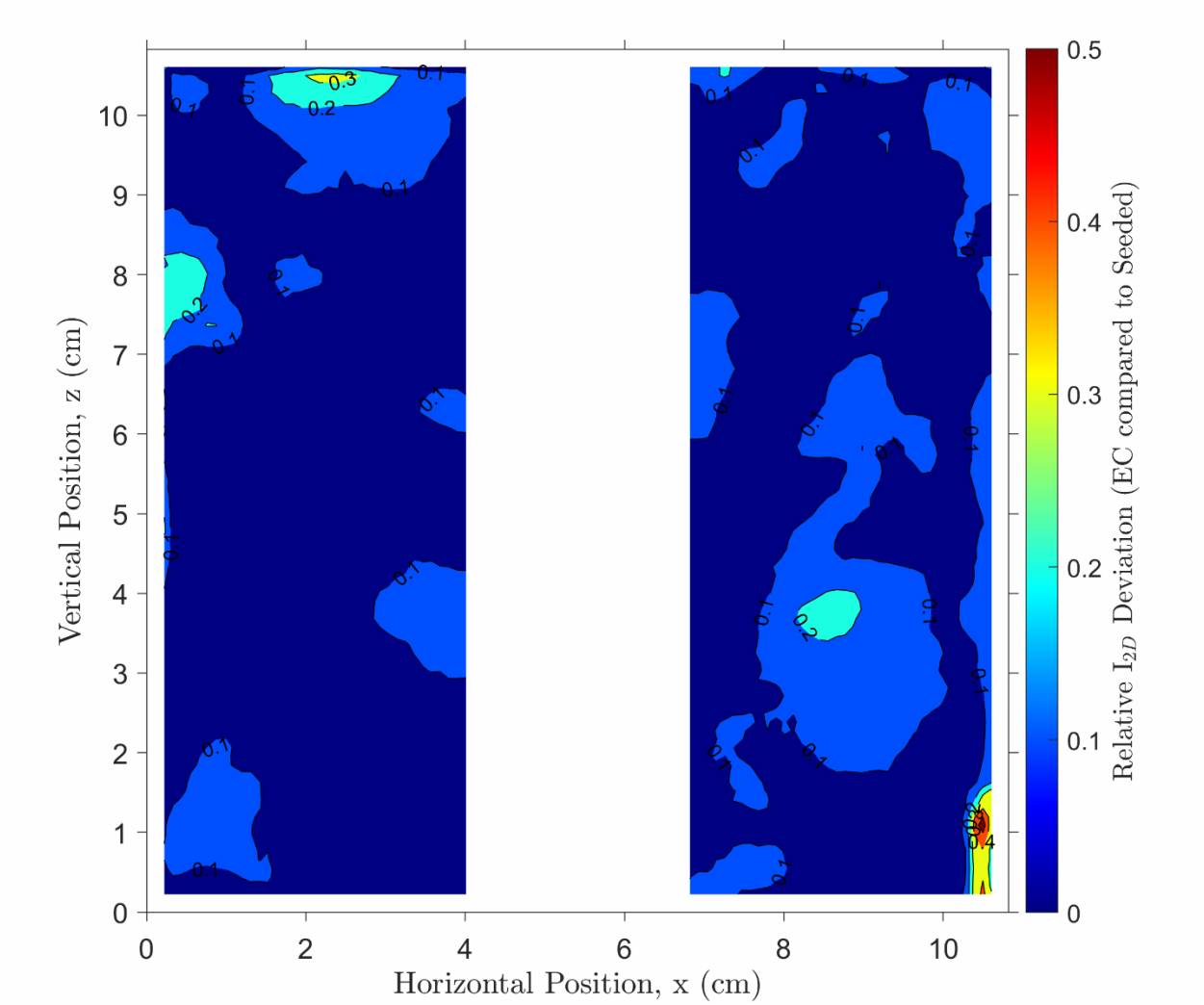

Figure A-32: Relative turbulence intensity deviation when comparing the turbulence intensity measurements between the EC and Seeded experiments for DS#1.b.

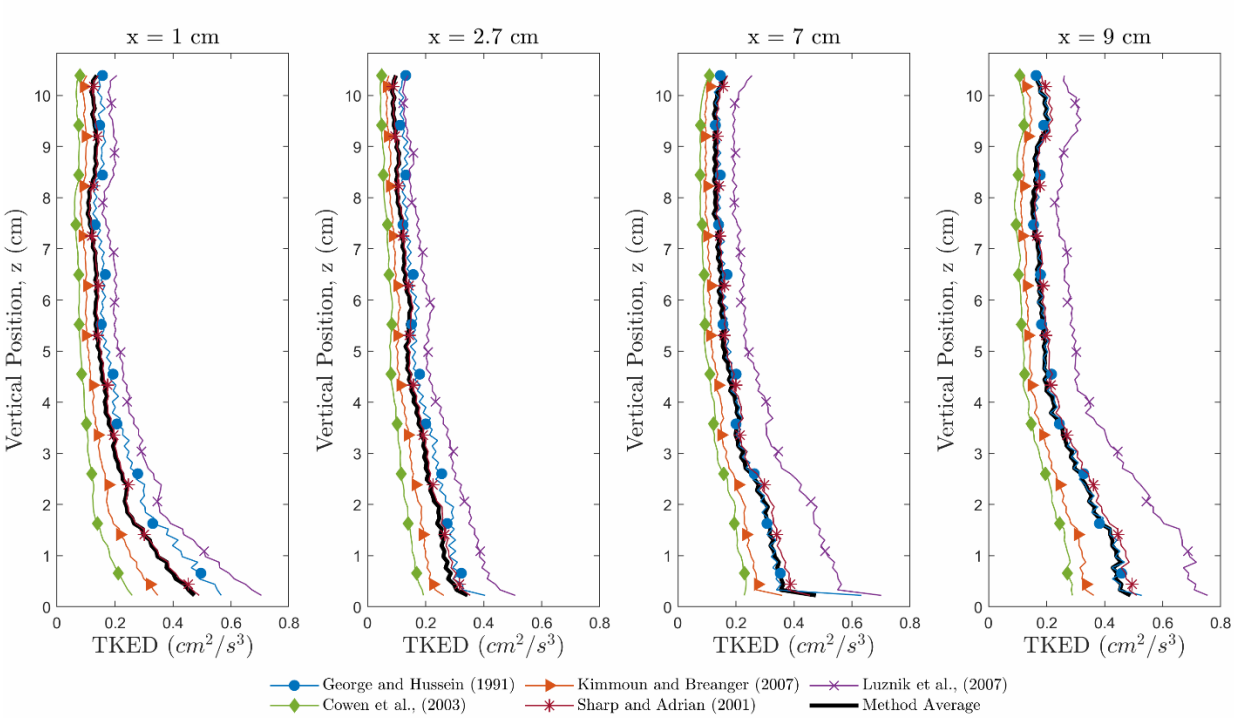

Figure A-33: Vertical variation of the TKED rate at 1 cm, 2.7 cm, 7 cm, and 9 cm along the horizontal axis by method and method average for the CC experiment for DS#1.b

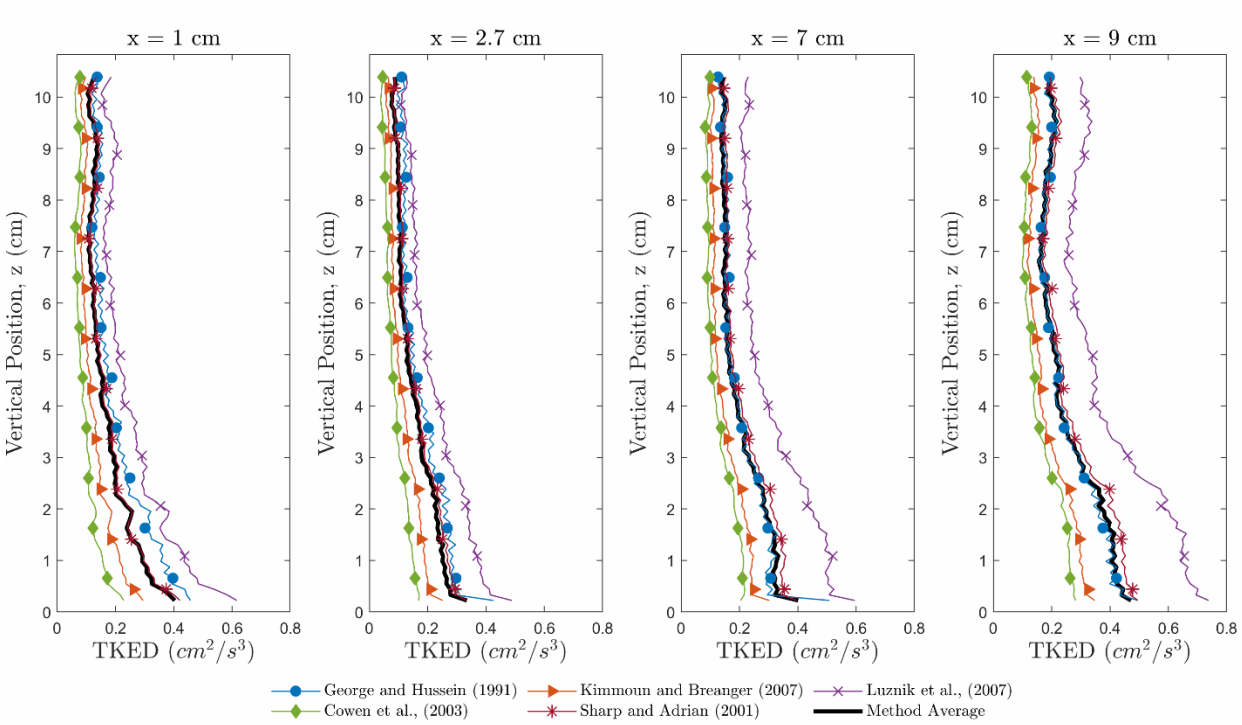

Figure A-34: Vertical variation of the TKED rate at 1 cm, 2.7 cm, 7 cm, and 9 cm along the horizontal axis by method and method average for the EC experiment for DS#1.b

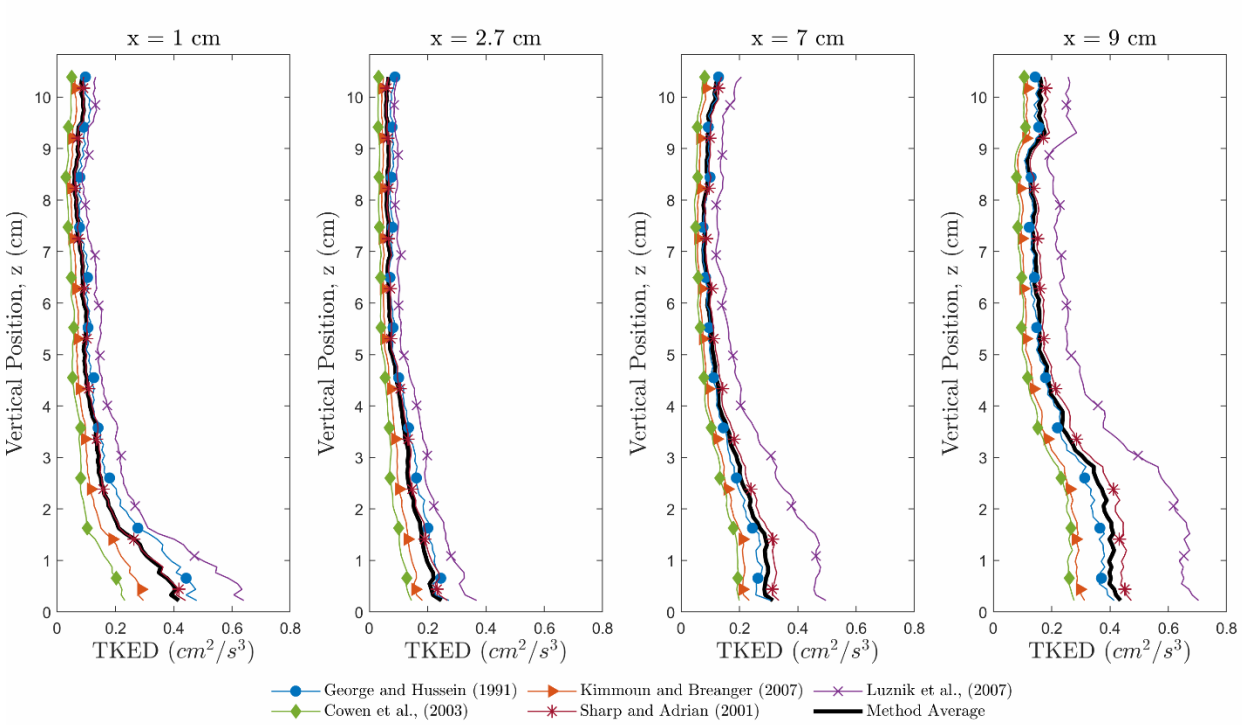

Figure A-35: Vertical variation of the TKED rate at 1 cm, 2.7 cm, 3 cm, and 3.9 cm along the horizontal axis by method and method average for the artificially seeded experiment for DS#1.b

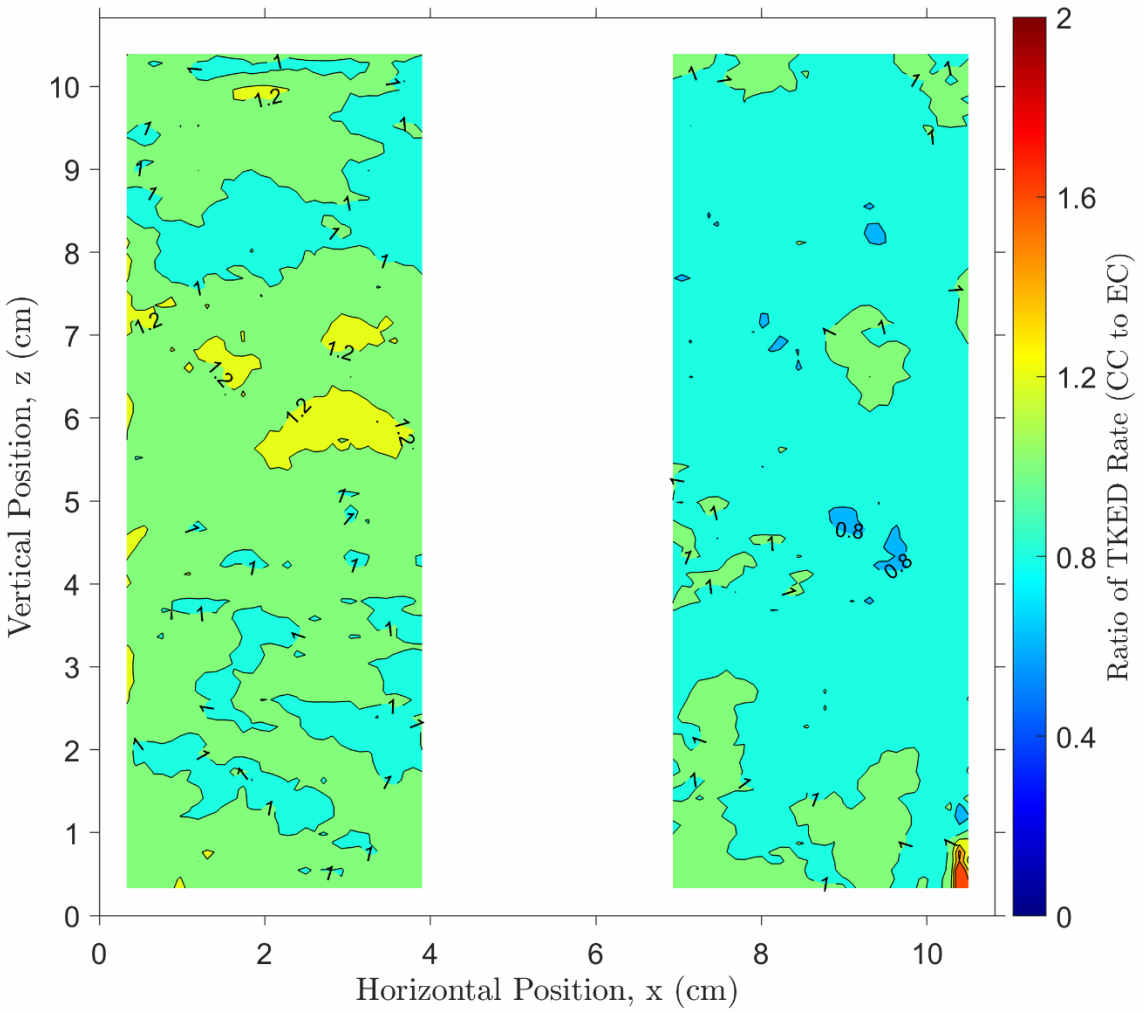

Figure A-36: Ratio of TKED rate from the CC and EC experiments for DS#1.b

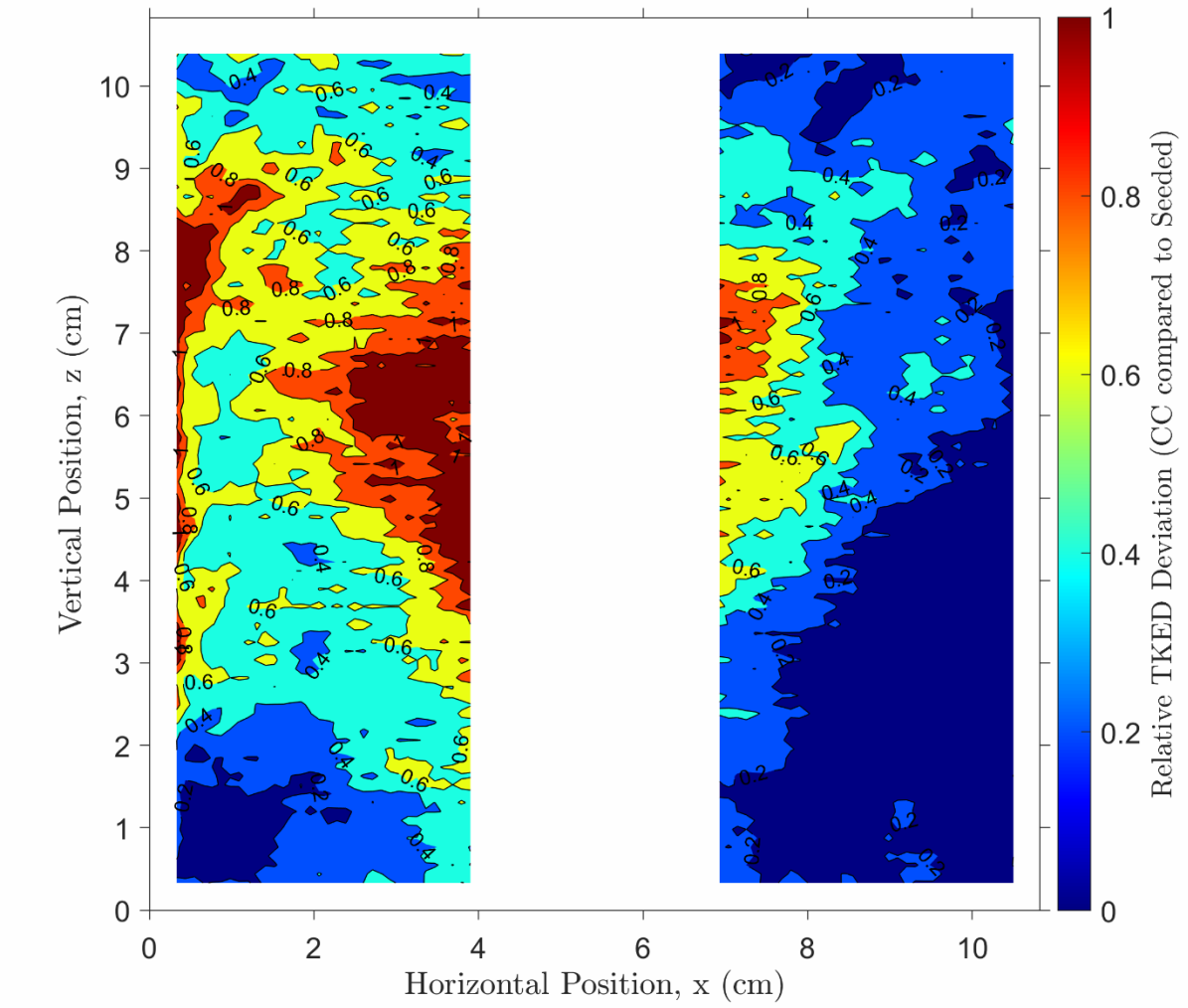

Figure A-37: Relative TKED rate deviation when comparing the TKED rate data from the CC and Seeded experiments for DS#1.b

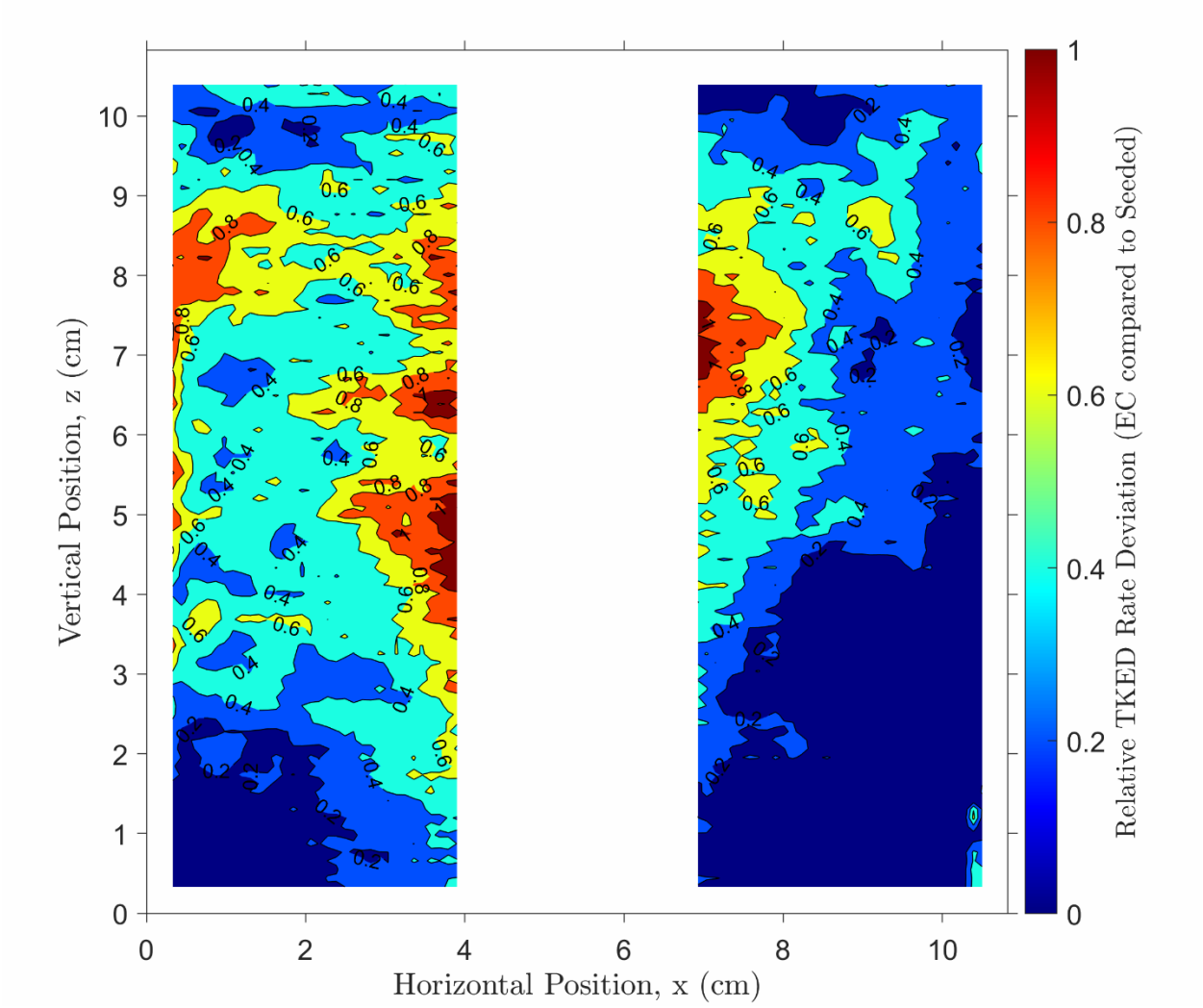

Figure A-38: Relative TKED rate deviation when comparing the TKED rate data from the EC and Seeded experiments for DS#1.b

APPENDIX B

Flocculation characterization duplicate (Data Set #1.b) experimental results and analysis.

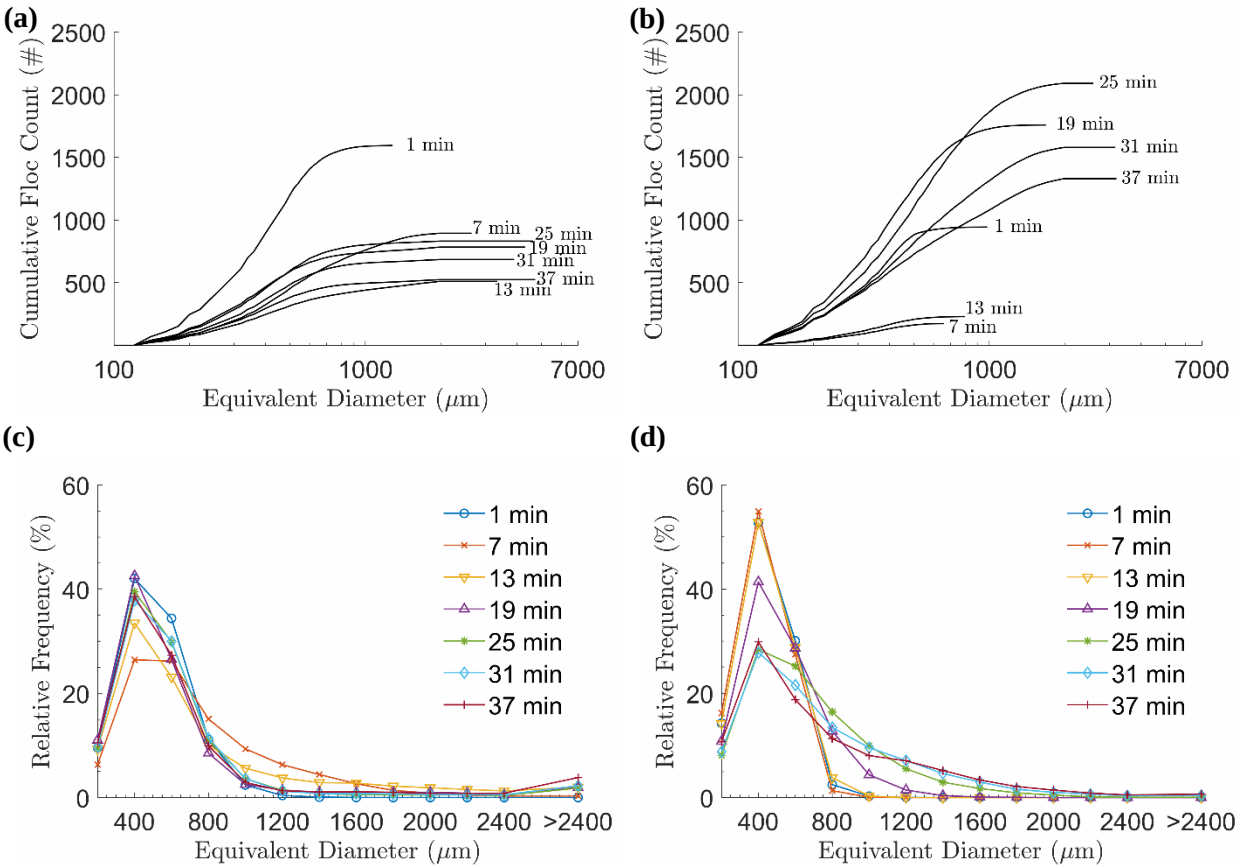

Figure B-39: Temporal evolution of floc size for DS#1.b (a) cumulative floc count for CC; (b) cumulative floc count for EC; (c) floc size distribution for CC; (d) floc size evolution for EC. Note: Floc size distributions were obtained by accumulating the total number of flocs for size intervals of 200 μm and are represented by a data point at the maximum of the size interval.

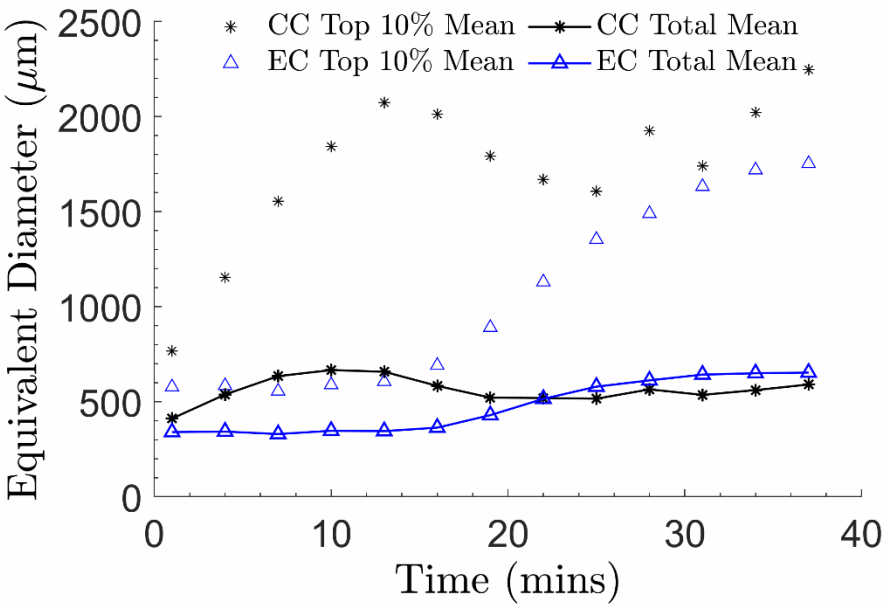

Figure B-40: Floc mean size evolution for CC and EC for DS#1.b

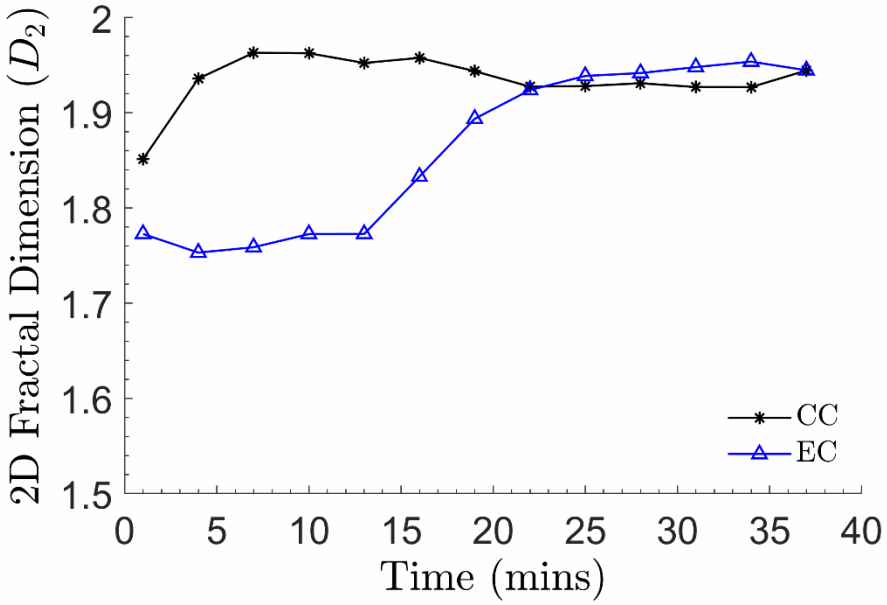

Figure B-41: 2D fractal dimension for CC and EC for DS#1.b

APPENDIX C

Experimental analysis results for duplicate test for reactor mixing characterization (DS#2)

For DS#2, the camera was equipped with a 65 mm Nikon AF NIKKOR lens at an effective lens focal plane distance of 237 mm, resulting in 108 mm by 108 mm field of view, a resolution of approximately 67.6 μm per pixel and a 3.2 mm depth of field. The field of view dimensions were confirmed by imaging a ruler located within the focal plane and verifying the pixel resolution. The camera aperture was set to f/2 to enable maximum light capture with an exposure time of 20 μs.

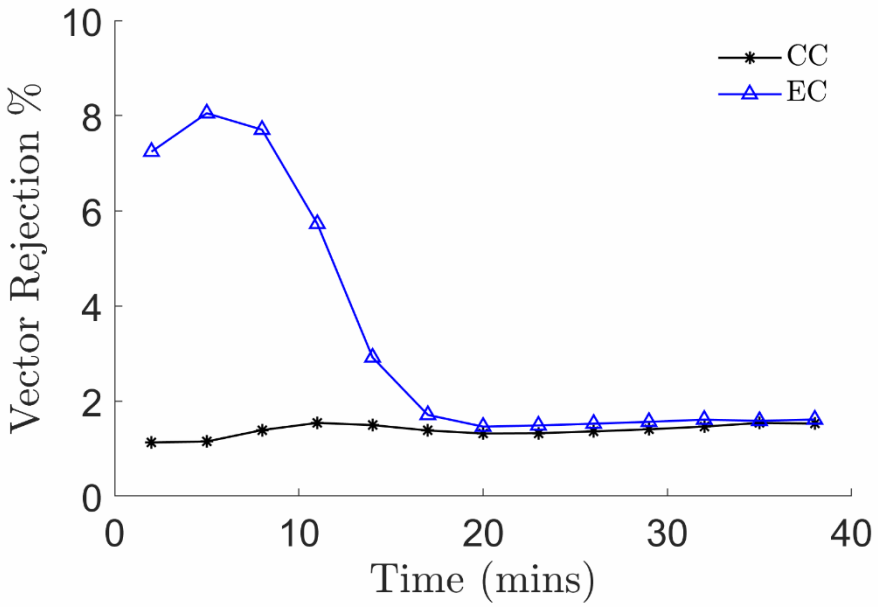

Figure C-42: Vector rejection percentage for the CC and EC experiments for DS#2

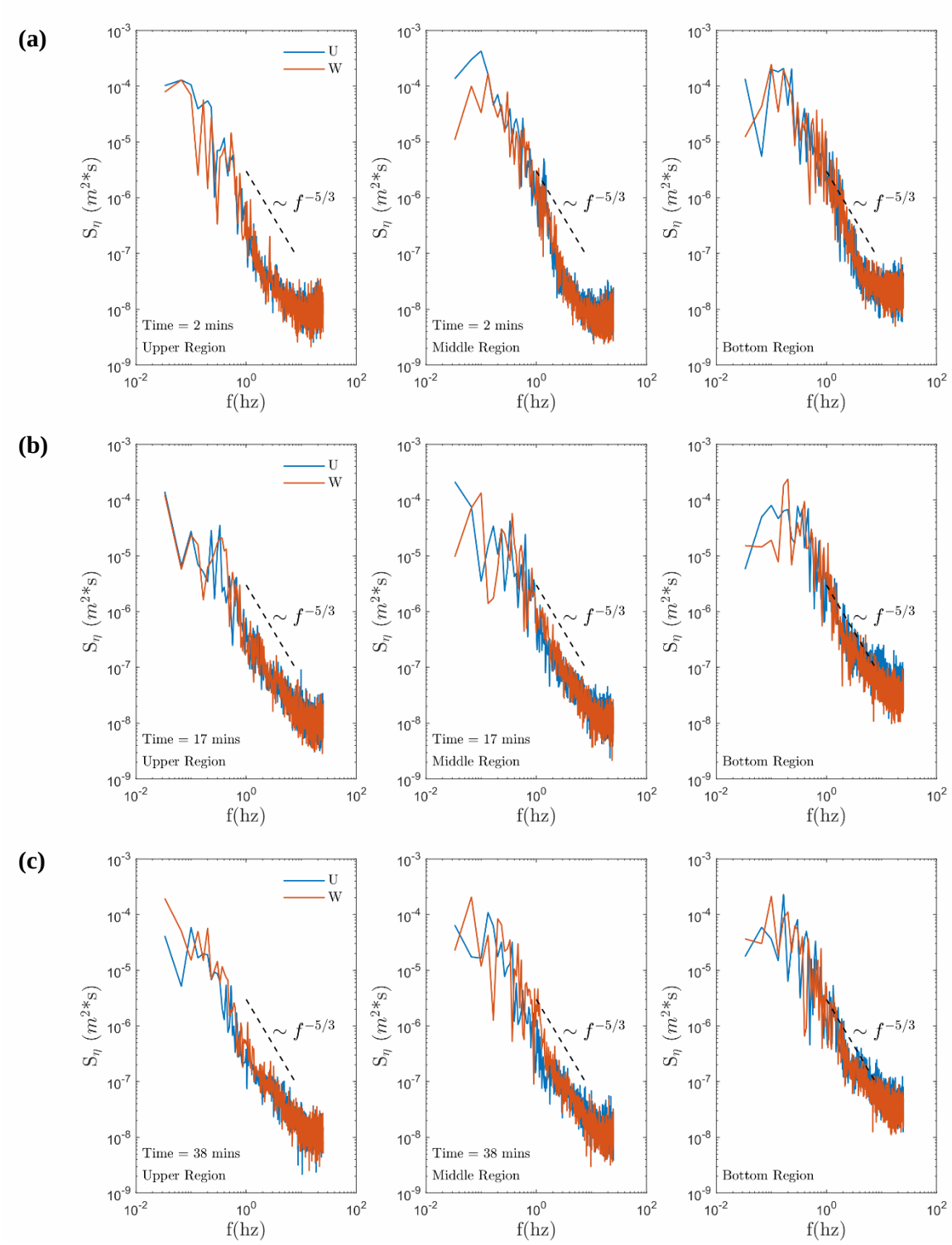

Figure C-43: Energy spectrum at the left upper, left middle, and left bottom region for horizontal (U) and vertical (W) velocity components for CC, DS#2 at (a) 2 minutes; (b) 17 minutes and (c) 38 minutes for DS#2

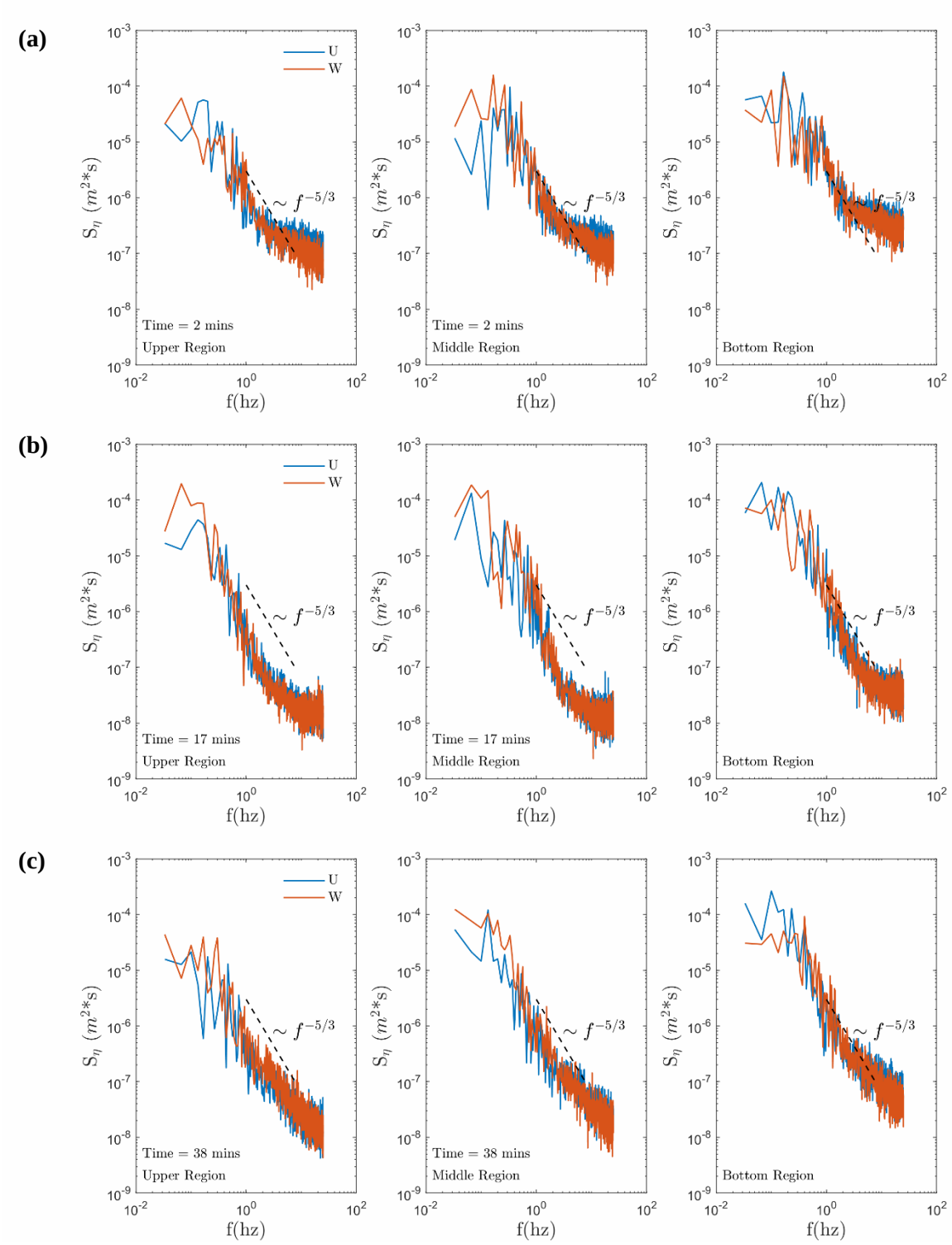

Figure C-44: Energy spectrum at the left upper, left middle, and left bottom region for horizontal (U) and vertical (W) velocity components for EC, DS#2 at (a) 2 minutes; (b) 17 minutes and (c) 38 minutes for DS#2

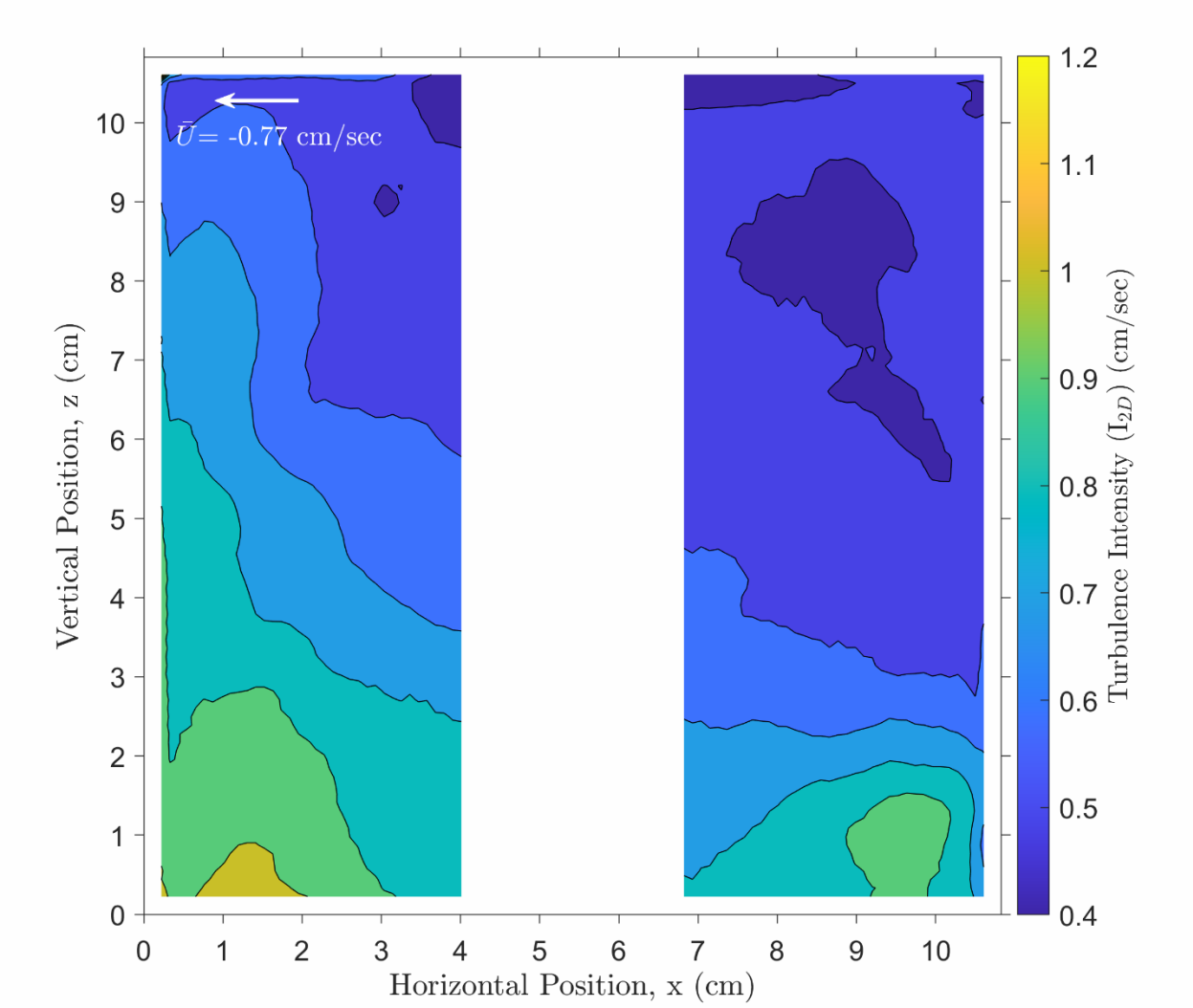

Figure C-45**:** Average 2D turbulence intensity for the CC experiment for DS#2. Average mean velocities in the horizontal and vertical directions are -0.77 cm/sec and 0.17 cm/sec, where positive values velocities in the positive x (horizontal) and z (vertical) direction as shown.

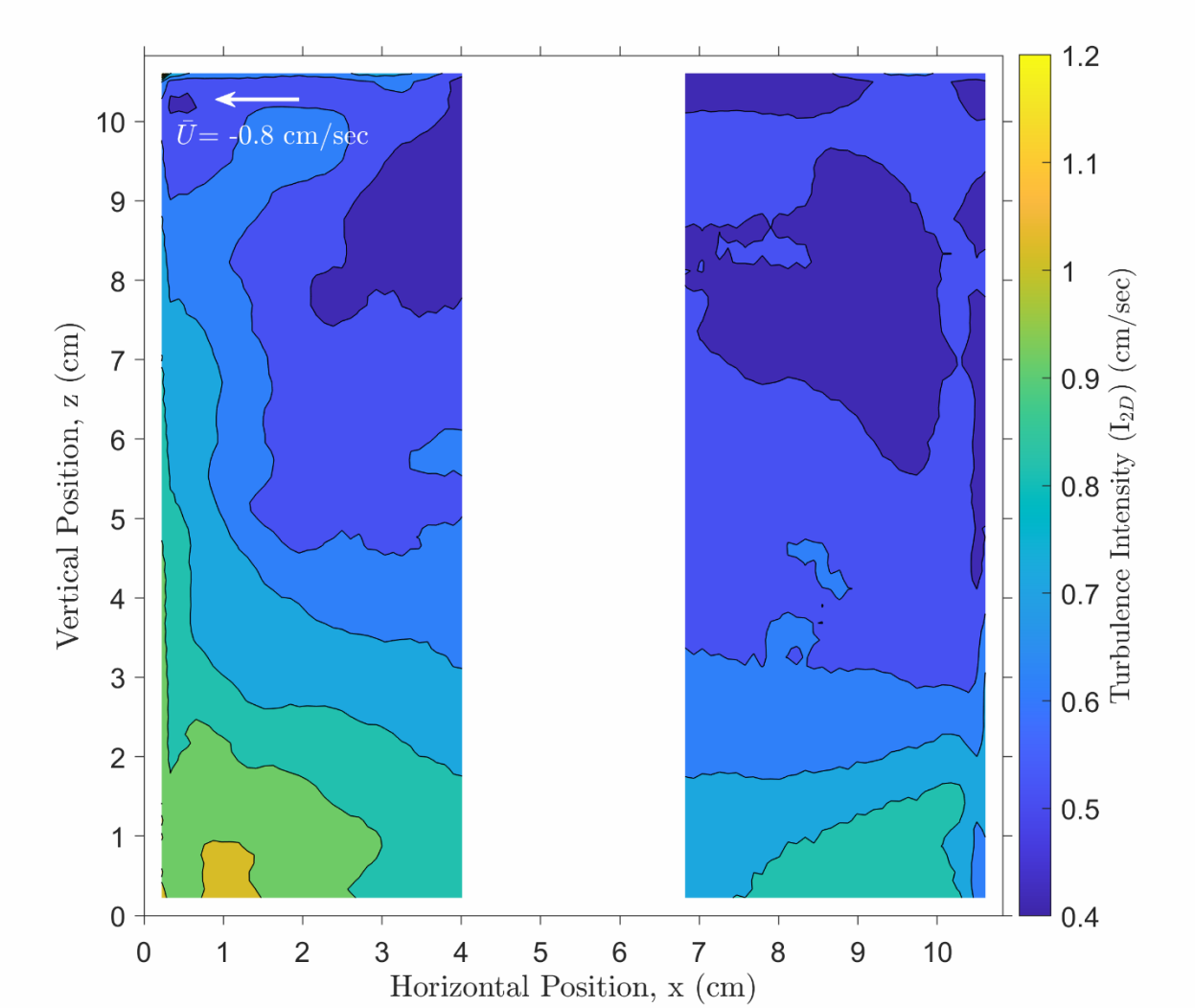

Figure C-46**:** Average 2D turbulence intensity for the EC experiment for DS#2. Average mean velocities in the horizontal and vertical directions are -0.80 cm/sec and 0.12 cm/sec, where positive values velocities in the positive x (horizontal) and z (vertical) direction as shown.

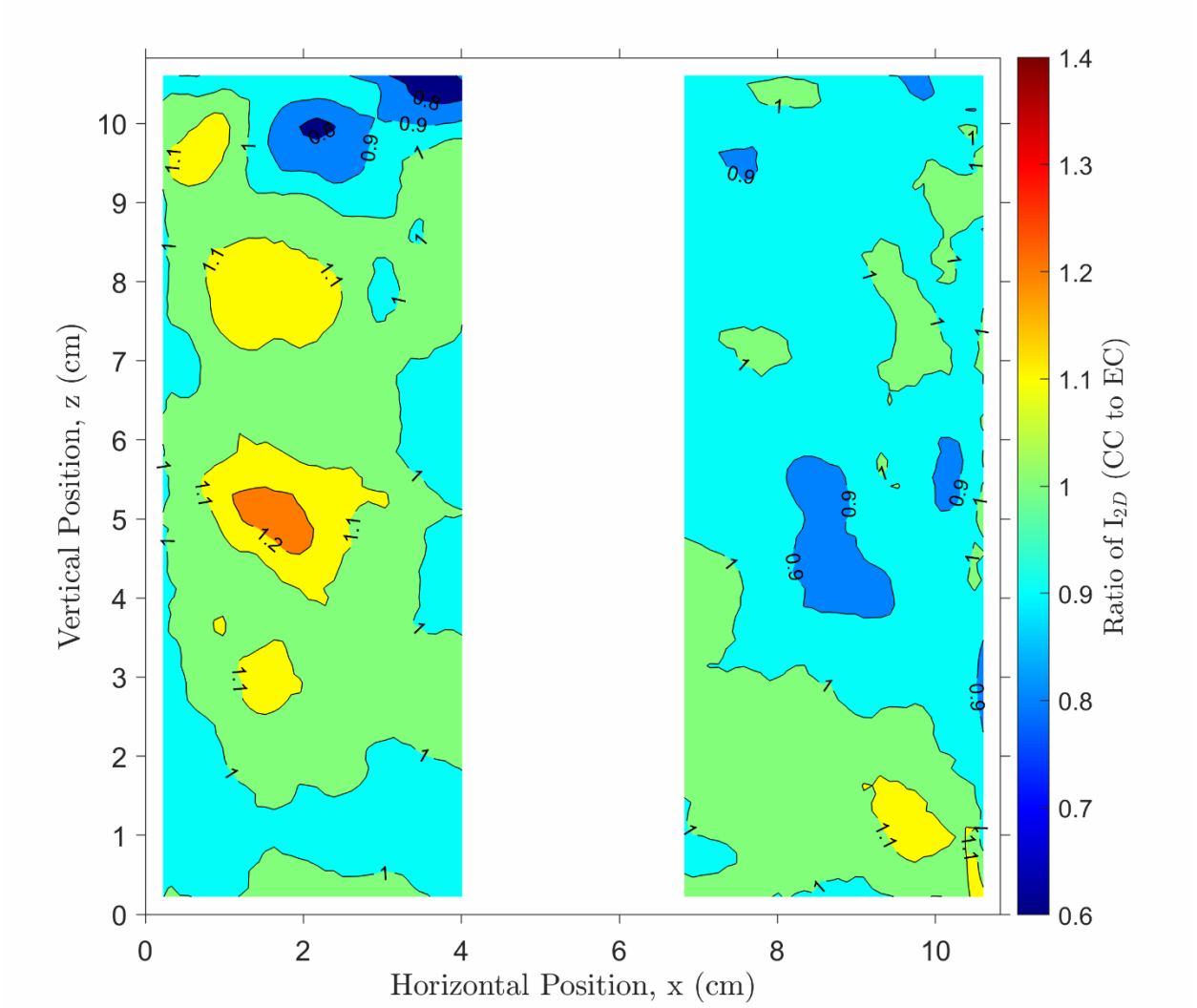

Figure C-47: Ratio of turbulence intensity values measured in the CC and EC experiments for DS#2.

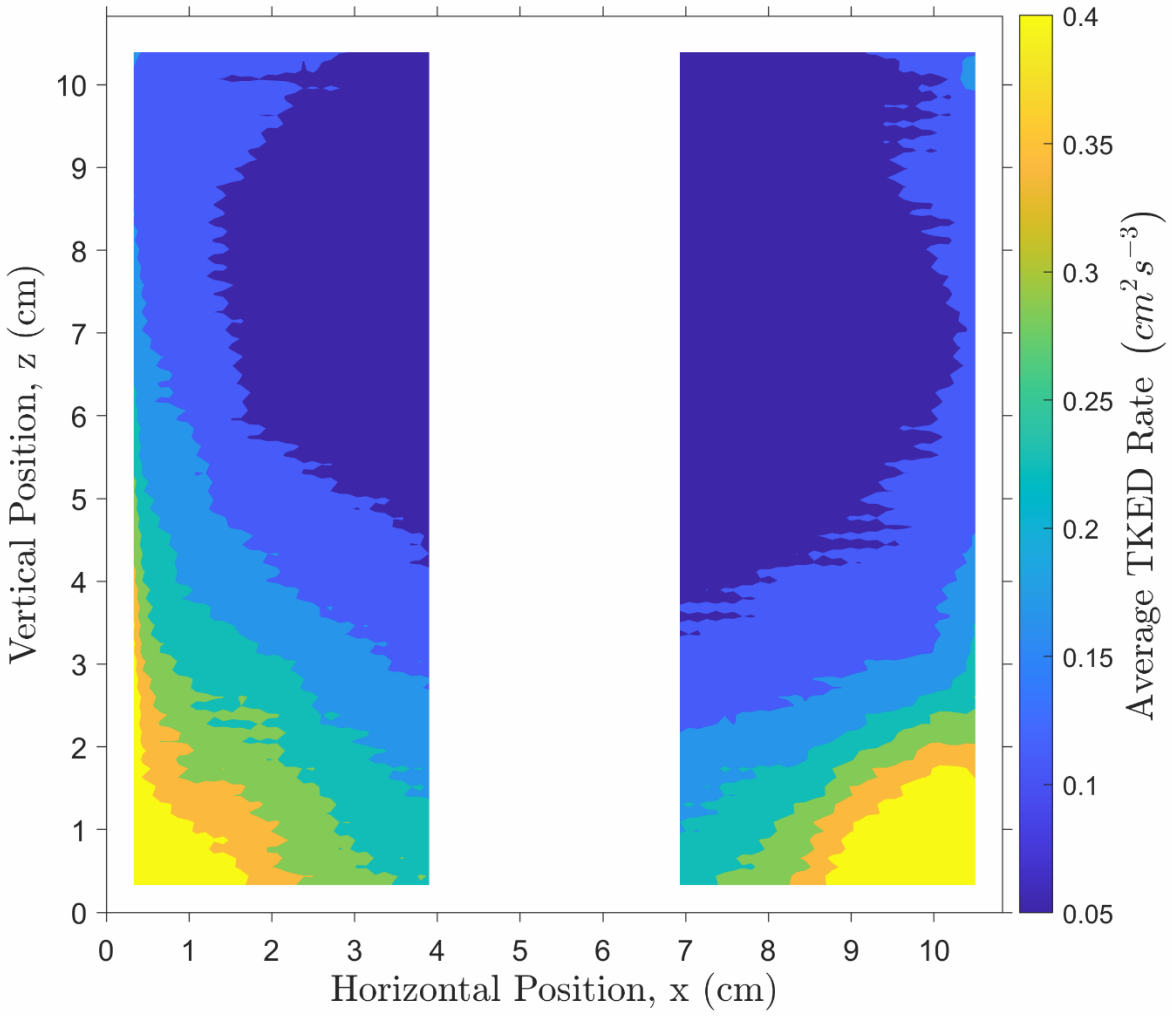

Figure C-48 Average local TKED rate for the CC experiment for DS#2

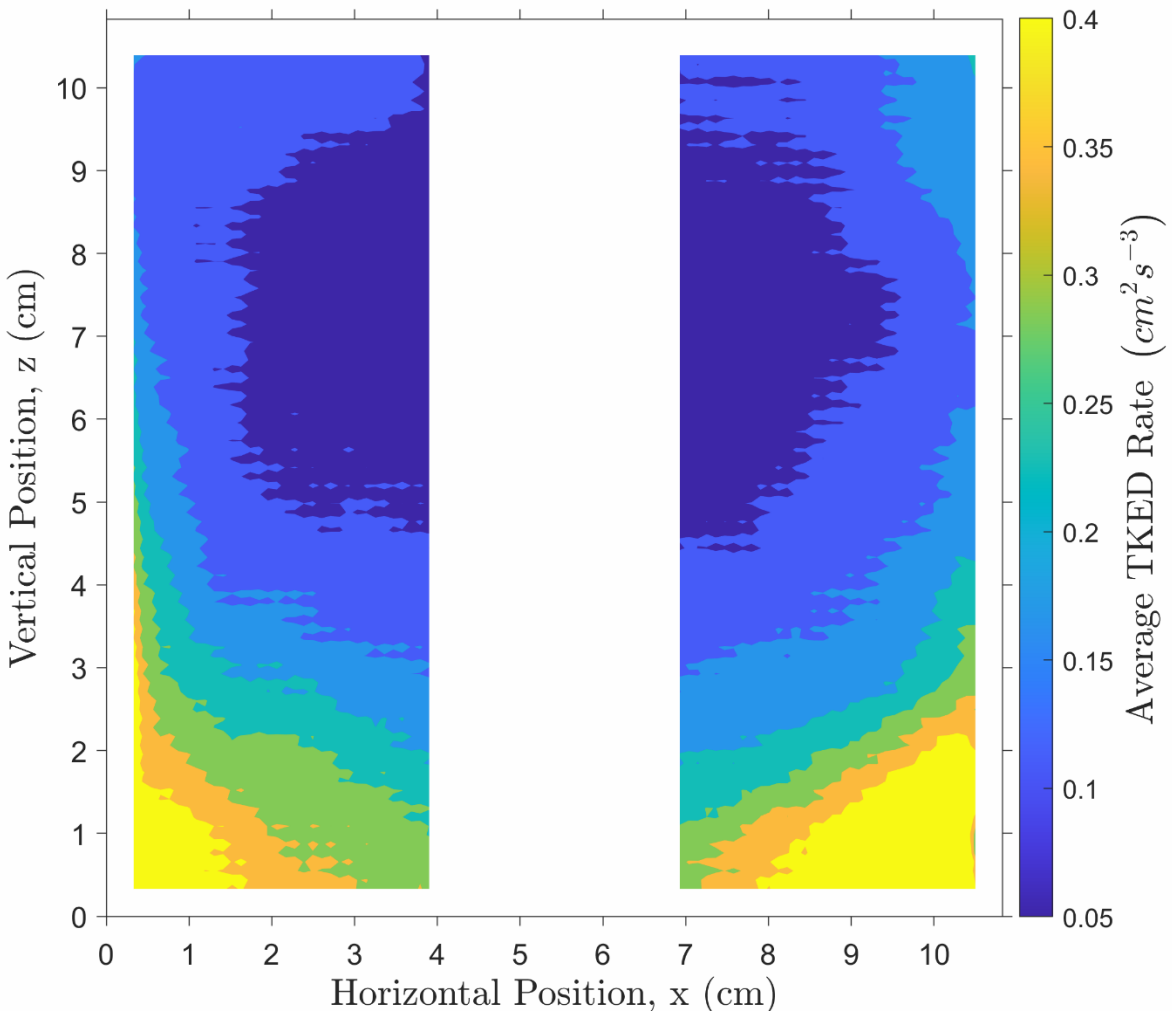

Figure C-49**:** Average local TKED rate for the EC experiment for DS#2

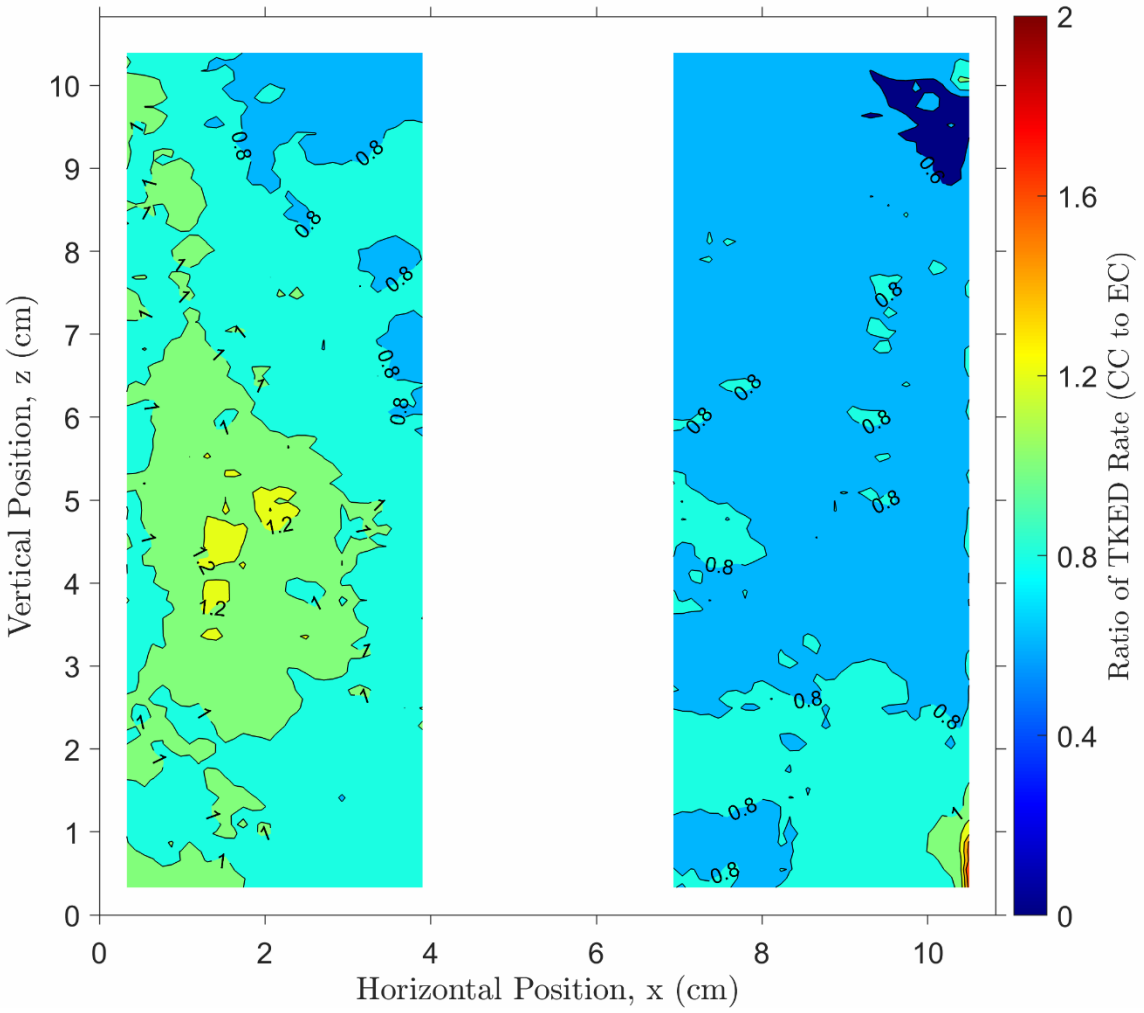

Figure C-50: Ratio of TKED rate from the CC and EC experiments for DS#2

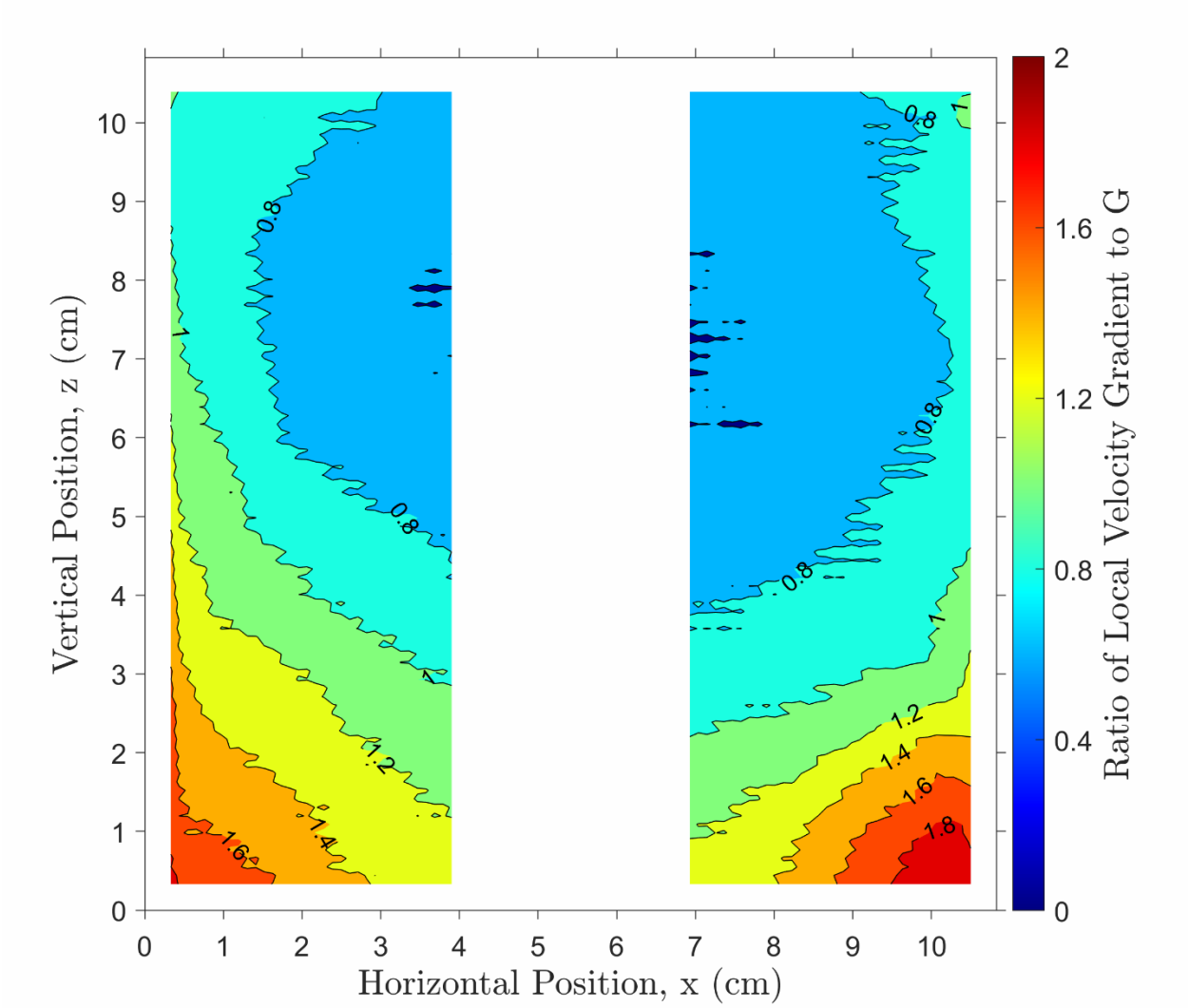

Figure C-51: Contours of the average ratio of the local velocity gradients to the global velocity gradient, G, as determined by the spatially averaged TKED rate for the CC experiment for DS#2

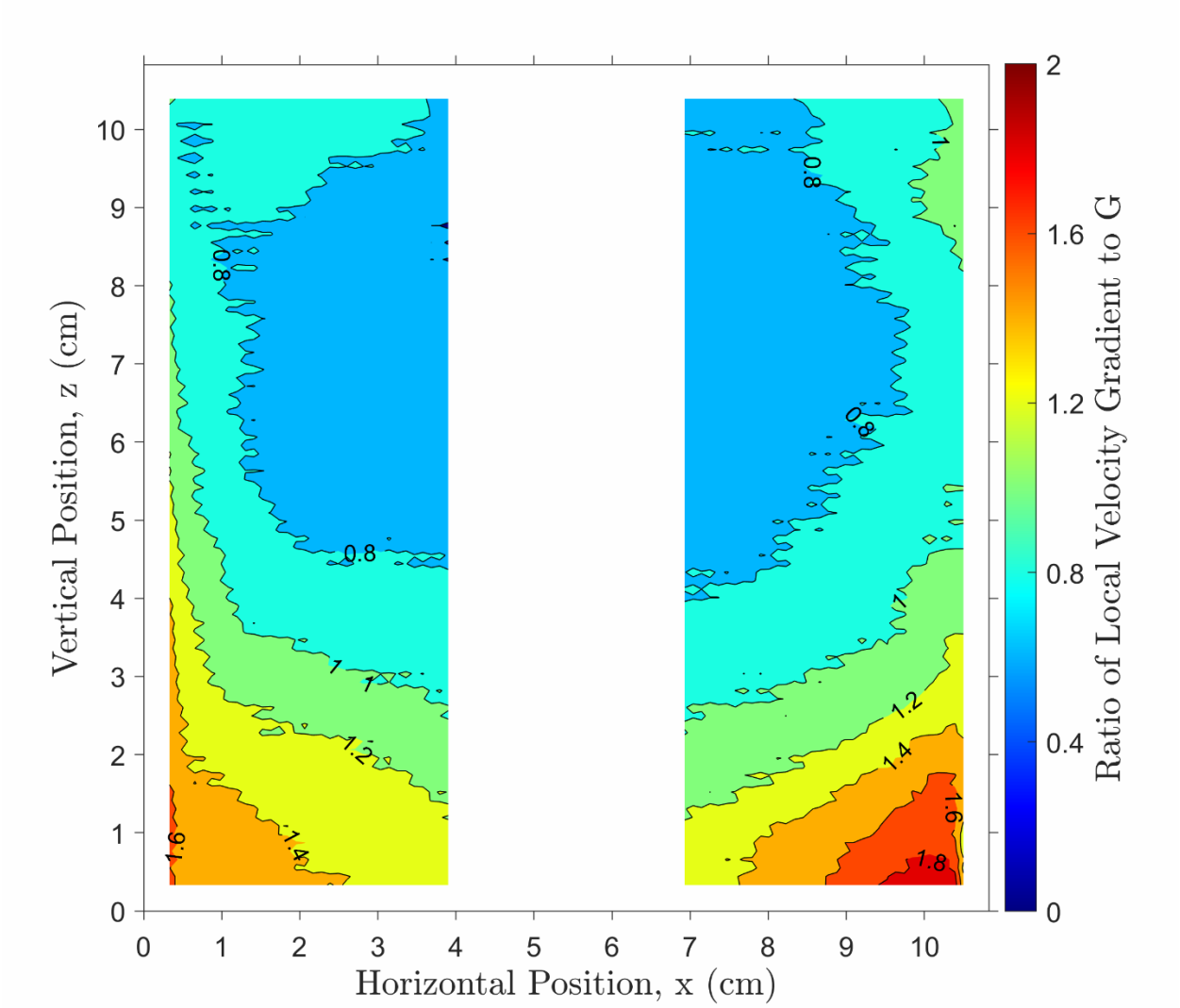

Figure C-52**:** Contours of the average ratio of the local velocity gradients to the global velocity gradient, G, as determined by the spatially averaged TKED rate for the EC experiment for DS#2

APPENDIX D

Duplicate reactor mixing characterization comparisons between DS#1.b (reported in the manuscript) and DS#2 (reported in Appendix C).

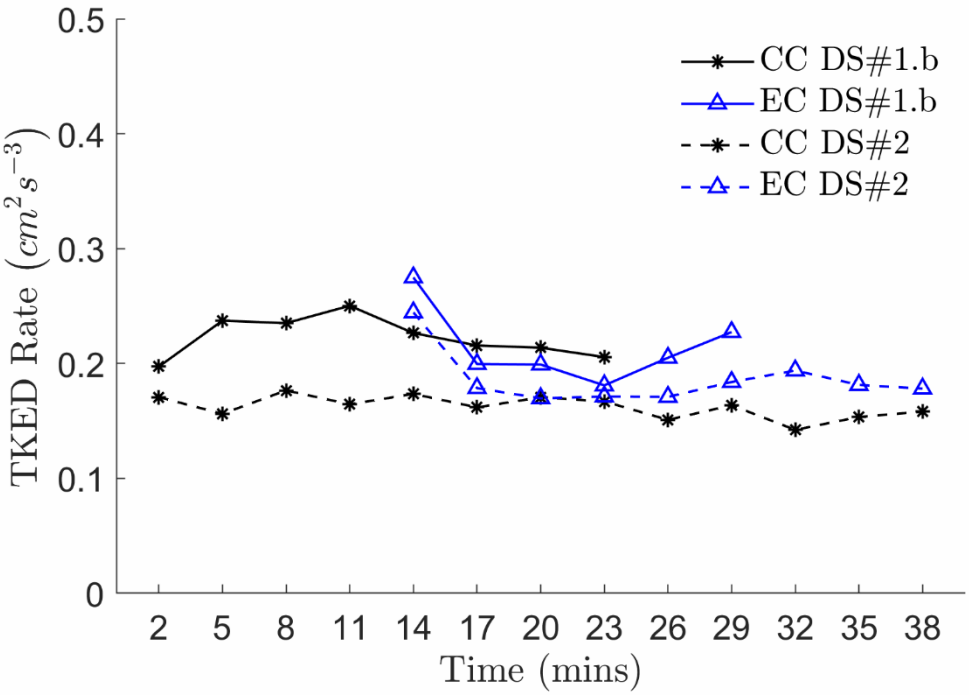

Figure D-53: Mean TKED rate over time for CC and EC for DS#1.b and DS#2.

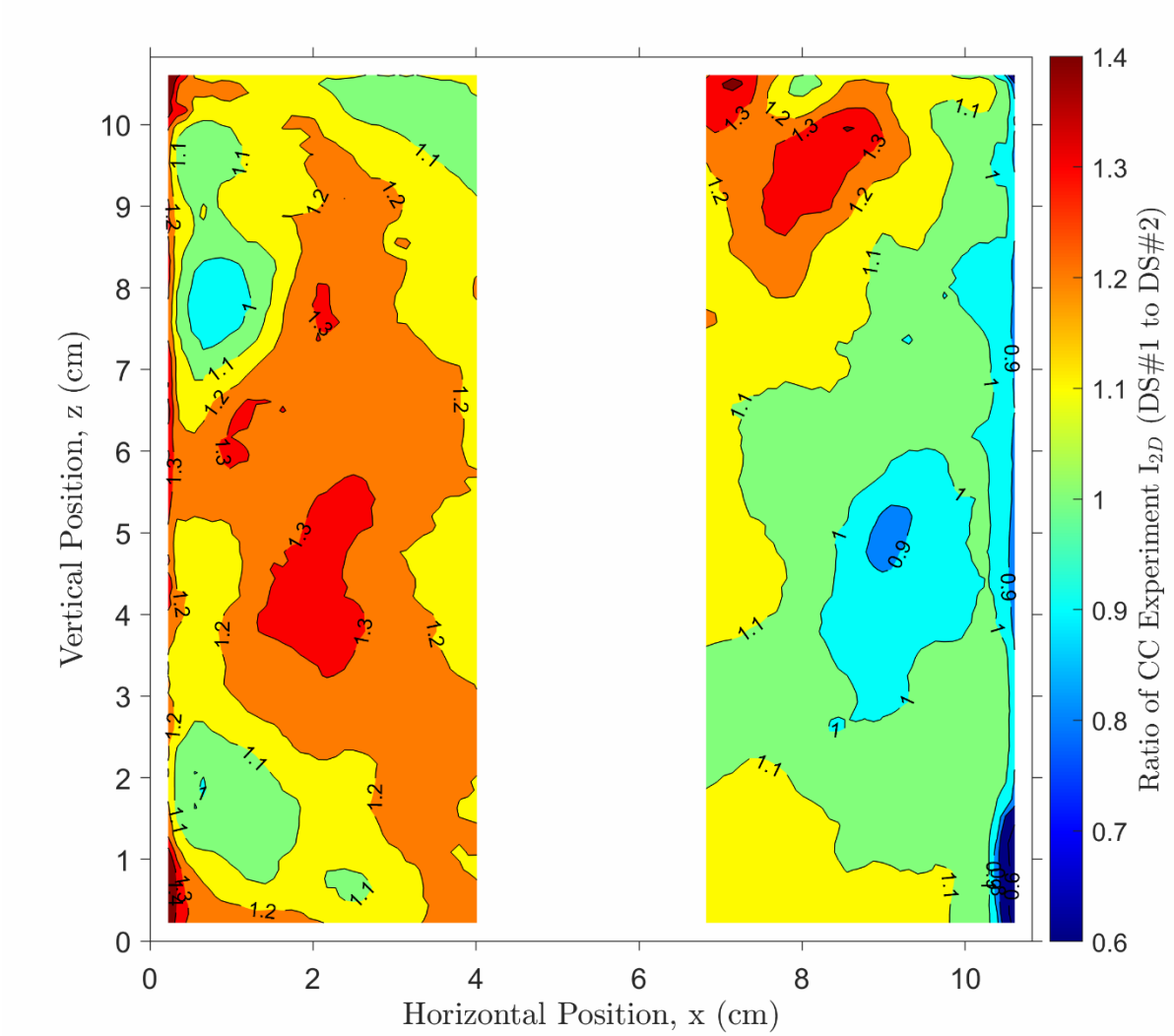

Figure D-54: Ratio of turbulence intensity results between DS#1.b to DS#2 for the CC experiment

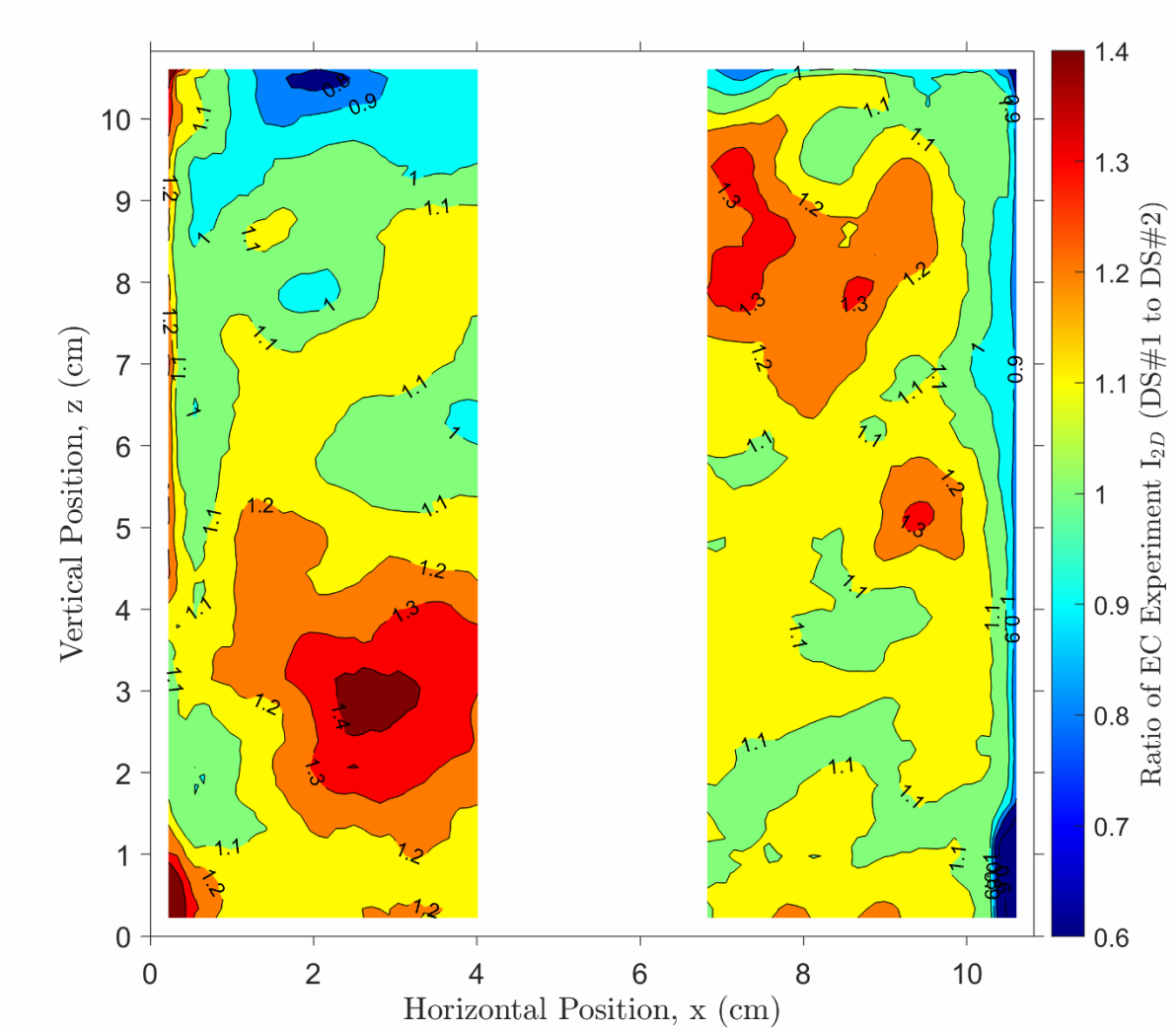

Figure D-55: Ratio of turbulence intensity results between DS#1.b to DS#2 for the EC experiment

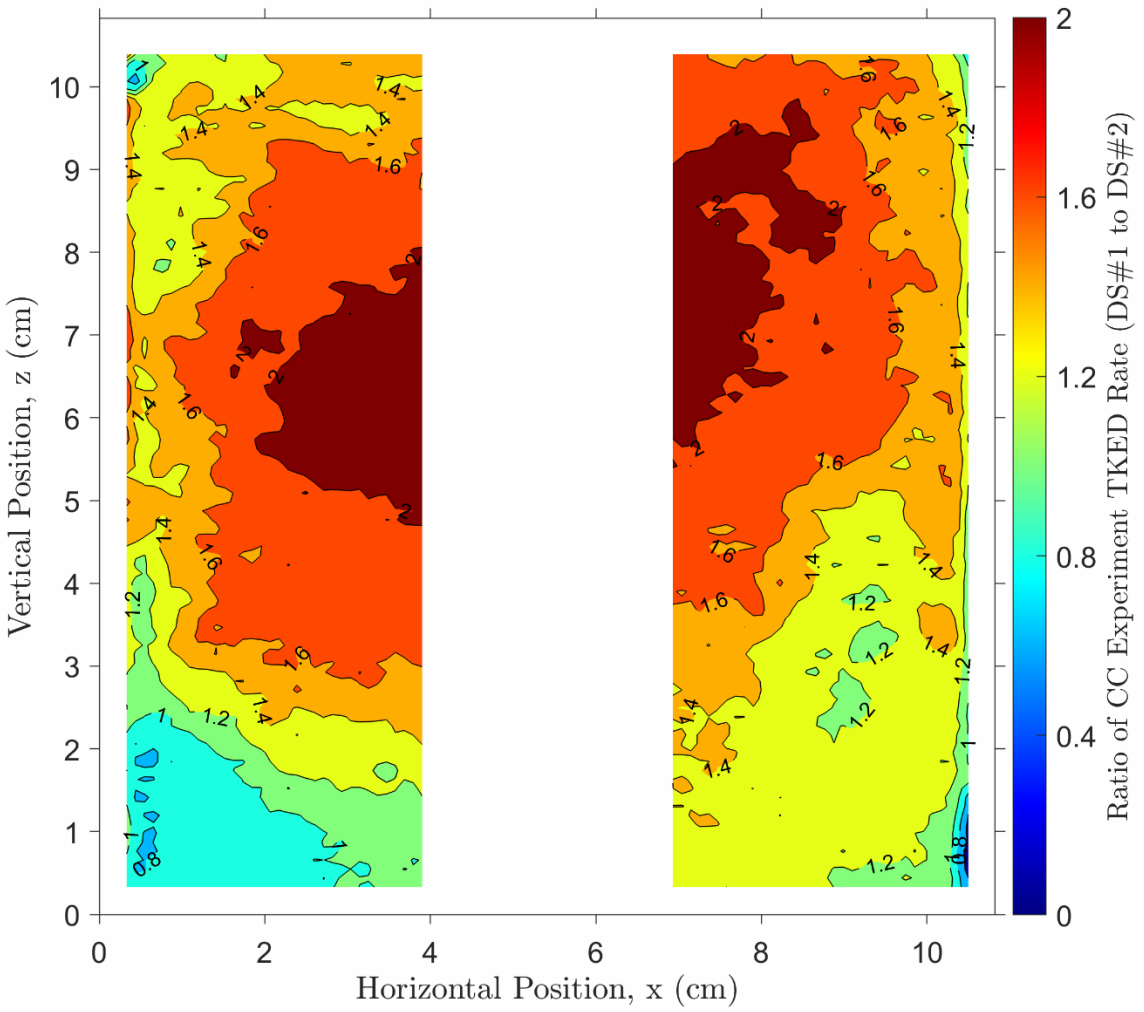

Figure D-56: Ratio of CC experimental results of TKED rate between DS#1.b to DS#2

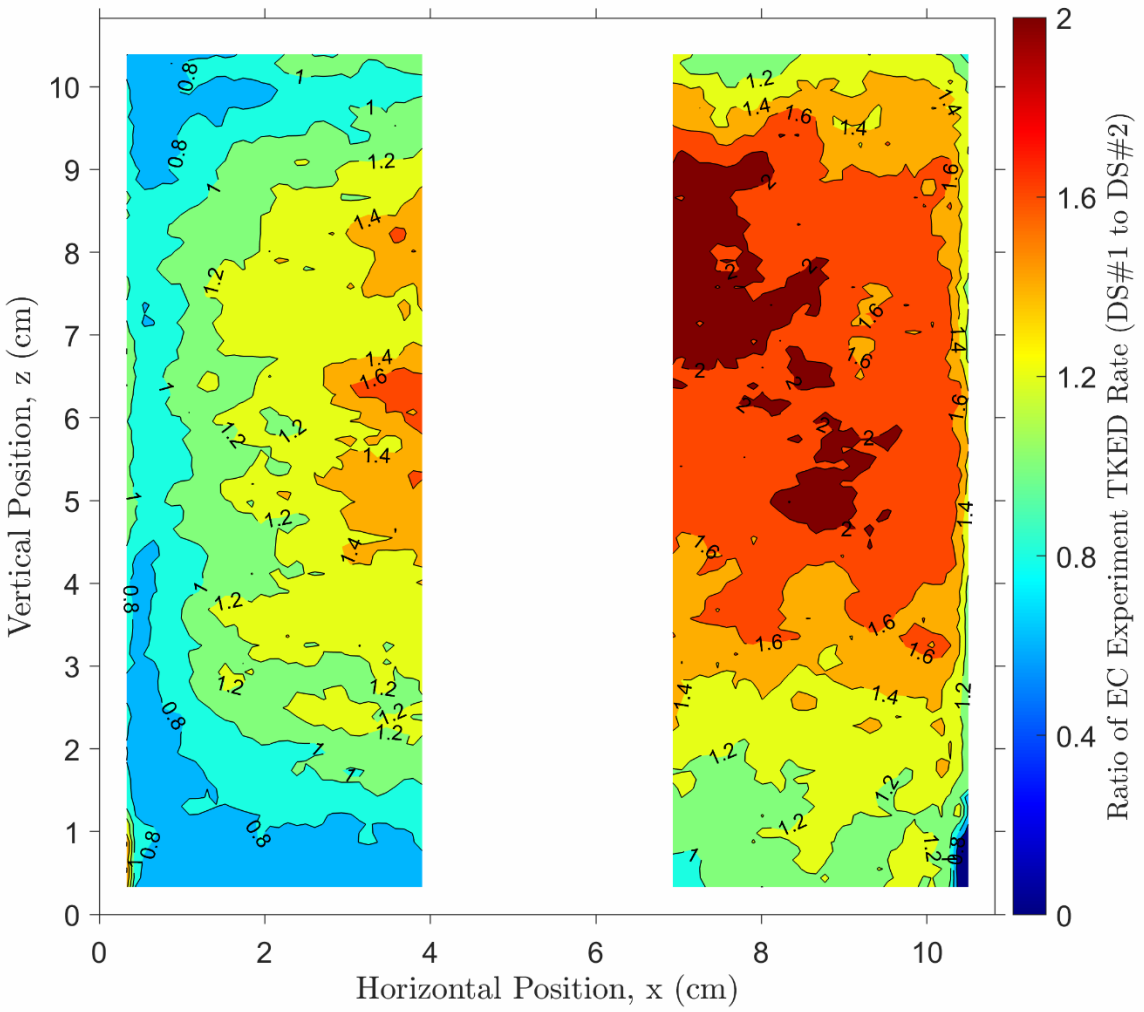

Figure D-57: Ratio of EC experimental results of TKED rate between DS#1.b to DS#2